Journal of Advanced Ceramics
先进陶瓷
ISSN 2226-4108
CN 10-1154/TQ
清华大学出版社 Tsinghua University Press
SciOpen

J Adv Ceram 2026, **15**: 9221406

https://doi.org/10.26599/JAC.2026.9221406

Review

Doping Engineering in piezocatalysis: Mechanisms, strategies, and perspectives

Xiaoli Xu[a,‡], Huan Zhai[a,‡], Jinqian Ma[a], Wanwan Cheng[a], Fanglin Shi[a],

Lingbo Xiao[b,*], Laishun Qin[a], Yanmin Jia[c,*], Da Chen[a,*]

[a]*College of Materials and Chemistry, China Jiliang University, Hangzhou 310018, China.*

[b]*Department of Applied Physics, Zhejiang University of Science and Technology, Hangzhou 310008, China.*

[c]*School of Physics and Information Technology, Shaanxi Normal University, Xi'an 710121, China.*

‡ These authors contributed equally to this work.

* Corresponding author.

E-mail address: L. Xiao, lbxiao@zust.edu.cn;

Y. Jia, ymjia@snnu.edu.cn;

D. Chen, chenda@cjlu.edu.cn

Received: September 24, 2026; Revised: November 4, 2026; Accepted: November 9, 2026

©The Author(s) 2026

Just Accepted

Abstract:

Piezocatalysis has emerged as a promising strategy for harvesting mechanical energy and driving chemical reactions toward sustainable energy conversion, environmental remediation, and biomedical applications. However, the practical implementation of piezocatalytic systems remains constrained by insufficient piezoelectric polarization, inefficient charge separation, and limited interfacial reaction kinetics. Doping engineering provides an effective atomic-scale approach to overcome these limitations by simultaneously regulating crystal structures, defect chemistry, electronic configurations, and piezoelectric properties. In this review, we establish a comprehensive framework encompassing crystal-structure regulation (lattice distortion, bond-length variation, and symmetry breaking), defect chemistry and carrier behavior (band-structure modulation, defect evolution, carrier concentration, and density-of-states regulation), and piezoelectric properties (polarization regulation and piezoelectric response enhancement) to elucidate the fundamental roles of dopants in piezocatalysis. The applications of doped piezocatalysts in environmental remediation, energy conversion, and biomedical fields are further reviewed. Finally, current challenges and future perspectives are proposed, focusing on rational dopant design, dynamic structure evolution, long-term stability, and scalable applications. This review provides mechanistic insights into doping-enabled piezocatalysis and offers guidance for the development of high-performance piezocatalytic materials for sustainable technologies.

Keywords: Doping engineering; Piezocatalysis; Crystal structure; Carrier behavior; Piezoelectric Properties

Just Accepted

1 Introduction

The escalating energy crisis and increasing environmental concerns have stimulated the development of sustainable technologies capable of converting renewable energy sources into valuable chemical products. Piezocatalysis, an emerging catalytic strategy that directly converts ubiquitous mechanical energy, such as water flow, vibration, and acoustic waves, into chemical energy[1, 2], has attracted increasing attention in recent years[2-6]. Unlike conventional photocatalytic and electrocatalytic processes that require external light irradiation or electrical input, piezocatalysis relies on the intrinsic piezoelectric polarization generated within non-

centrosymmetric materials under mechanical deformation, enabling spontaneous charge separation and surface redox reactions[7-9]. Owing to this unique mechanism, piezocatalysis has demonstrated great potential in clean energy conversion [7, 8], environmental remediation[10-12], and biomedicine[13-15].

The fundamental prerequisite for piezocatalysis is the presence of a non-centrosymmetric crystal structure capable of generating piezoelectric polarization under mechanical stimulation. Representative piezoelectric materials, including ZnO[16-18], CdS[19], $BaTiO_3$[20-22], $Pb(Zr,Ti)O_3$[23], $KNbO_3$[24], and $BiFeO_3$[25], have been widely investigated owing to their intrinsic polar structures and electromechanical coupling characteristics. Under external mechanical stress, the displacement of positive and negative charge centers within the lattice generates polarization charges on opposite surfaces of the material[26]. The resulting internal electric field drives directional carrier migration, promotes electron–hole separation, and activates interfacial redox reactions. However, despite significant progress, the practical efficiency of piezocatalytic systems remains limited by insufficient polarization intensity, rapid carrier recombination, restricted carrier transport, and sluggish surface reaction kinetics[27, 28]. Therefore, rational regulation of intrinsic material properties is essential for simultaneously enhancing polarization generation, charge utilization, and catalytic activity[29, 30]. In addition, nanoscale characteristics, including particle size and domain configuration, together with polarization stability, play important roles in piezocatalysis. Accordingly, various strategies, including morphology engineering[9, 31] and defect engineering, have been developed to enhance piezocatalytic performance. From a material-design perspective, these strategies can be broadly classified into two complementary categories. The first focuses on improving piezoelectric properties through phase-boundary engineering, strain engineering, Curie-temperature regulation, electrical modulation, and crystallographic orientation control. In particular, crystallographic texturing can enhance the macroscopic piezoelectric response of perovskite ferroelectric ceramics by promoting preferential grain orientation, providing a complementary approach to composition-based regulation of electromechanical properties [32]. These approaches can strengthen electromechanical coupling and mechanically induced polarization. The second focuses on optimizing carrier dynamics and interfacial reaction kinetics through defect engineering, heterostructure construction, cocatalyst loading, and carbon modification. These strategies can

Just Accepted

regulate carrier concentration, facilitate charge separation and transport, and improve surface redox kinetics [33].

Among these approaches, doping engineering represents a particularly versatile atomic-scale strategy because it can simultaneously influence both design pathways through coupled regulation of crystal structure, defect chemistry, and electronic properties. Specifically, dopant incorporation can modify lattice distortion, phase stability, crystal symmetry, and polarization, thereby influencing piezoelectric properties[34]. Meanwhile, doping can alter defect chemistry, electronic structure, carrier concentration, and surface active sites, facilitating charge separation, transport, and interfacial redox reactions [35]. However, the effects of doping extend beyond simple compositional substitution and involve complex interactions among lattice reconstruction, defect compensation, electronic redistribution, and polarization evolution[36, 37]. Depending on dopant valence, ionic radius, electronic configuration, and occupation sites, introduced dopants can induce local lattice distortion, chemical bond variation, and symmetry breaking, thereby modifying piezoelectric responses and polarization behavior[38-41]. Meanwhile, dopant-induced electronic reconstruction can regulate band structures, defects, carrier concentration, density of states, and charge-transfer pathways, improving carrier migration and accelerating interfacial redox reactions[42-48]. Nevertheless, the influence of doping on piezocatalysis is highly dependent on dopant species, concentration, incorporation sites, and defect configurations. Excessive or inappropriate doping may introduce secondary phases[49], excessive lattice disorder[50], deep-level recombination centers[51], charge-screening effects[52], and structural instability[53], resulting in weakened polarization and reduced catalytic efficiency[54]. Therefore, understanding the balance between beneficial and detrimental effects of doping is critical for the rational design of high-performance piezocatalysts.

With the rapid development of piezocatalysis, previous reviews have mainly focused on fundamental mechanisms, material systems, and representative applications[6, 55, 56], while recent studies have also highlighted various enhancement strategies, including defect engineering[27], morphology regulation[57], heterojunction construction[58], and polarization optimization[51, 59]. In particular, Shi et al. systematically reviewed defect-engineering strategies, including intrinsic defect activation, vacancy engineering, heteroatom doping, and complex defect construction, for improving piezocatalytic performance in environmental remediation and energy conversion [60]. These studies have significantly advanced the understanding of performance

Just Accepted

enhancement mechanisms. However, the intrinsic relationships among dopant characteristics, defect compensation, lattice symmetry regulation, carrier behavior, polarization evolution, and catalytic reactions remain insufficiently established. Moreover, the beneficial and detrimental effects of doping across different piezocatalytic systems have not been systematically integrated[61-63]. Improper dopant species or excessive doping concentrations may induce secondary phases[63], excessive lattice distortion[64], defect-induced charge recombination[61, 65], weakened polarization, and structural instability[66], ultimately deteriorating piezocatalytic performance. Consequently, a comprehensive understanding of how doping regulates crystal structure, defect chemistry, electronic structure, piezoelectric properties, and catalytic processes remains lacking.

In this review, we establish a unified structure, defect, carrier, and polarization framework to systematically elucidate the role of doping engineering in piezocatalysis. Different doping strategies, including heterovalent doping, isovalent doping, co-doping, defect-mediated doping, and spatially selective doping, are critically analyzed from the perspective of atomic-scale regulation mechanisms. The effects of dopant incorporation on lattice structure modulation, defect chemistry regulation, electronic structure reconstruction, carrier transport, and piezoelectric property enhancement are comprehensively discussed to reveal their underlying structure property relationships. Furthermore, the applications of doped piezocatalysts in environmental remediation, energy conversion, and biomedical fields are summarized (**Figure 1**). Finally, current challenges and future perspectives are discussed, focusing on rational dopant design, dynamic structural evolution, long-term stability, and practical scalability. This review aims to provide mechanistic insights into doping-enabled piezocatalysis and offer guidelines for the development of next-generation high-performance piezocatalytic materials.

Just Accepted

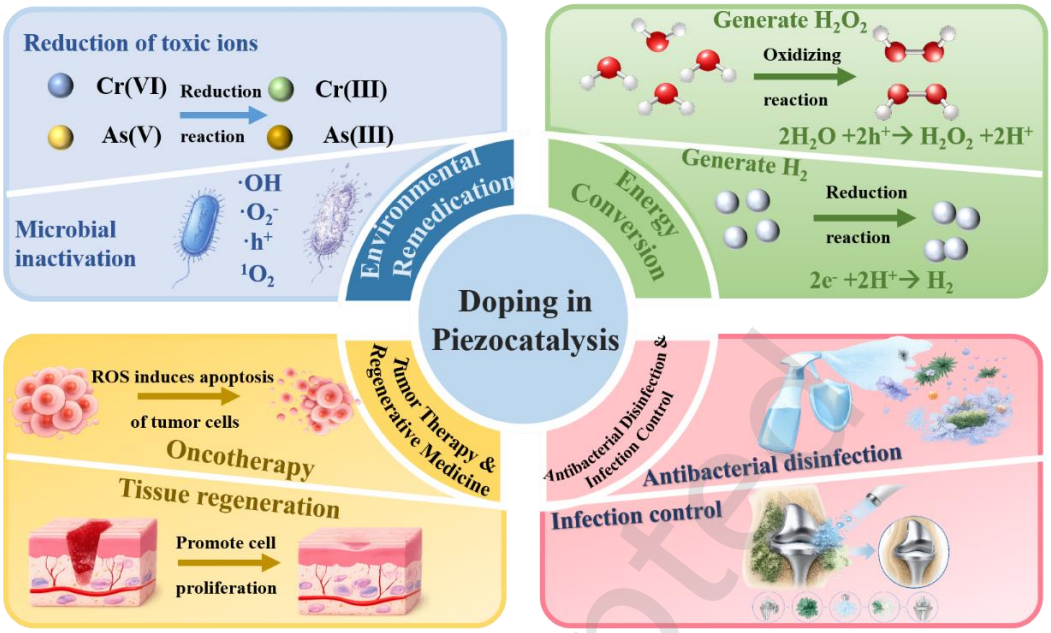


Figure 1 Overview of doping-engineered piezocatalysis for multifunctional applications.

2 Doping engineering

Doping engineering improves piezocatalytic performance through the coupled evolution of crystal structure, defect chemistry, electronic states, and piezoelectric polarization. As illustrated in **Figure 2**, this process begins with dopant incorporation, which modifies the local coordination environment according to the dopant's ionic radius, valence state, and preferred lattice site, thereby inducing lattice distortion, bond-length variation, and symmetry changes [67, 68]. In parallel, particularly in aliovalently doped systems, charge imbalance drives defect compensation through the formation or redistribution of vacancies, interstitials, and defect complexes[69]. The resulting structural and defect modifications jointly reconstruct the electronic structure, regulate carrier concentration and transport, and alter local charge distribution. These changes can further modify polarization behavior and piezoelectric response by affecting asymmetric atomic displacement and local symmetry [51, 69]. Under mechanical stimulation, the resulting piezoelectric polarization field promotes directional charge separation and migration, thereby influencing interfacial charge transfer and catalytic reactions. Importantly, these processes are not strictly sequential or independent: structural distortion affects defect formation, defects modify electronic states and polarization, and the resulting electronic and electromechanical responses can interact with one

Just Accepted

another. Their net effect on catalytic activity therefore depends on the balance among these coupled factors.

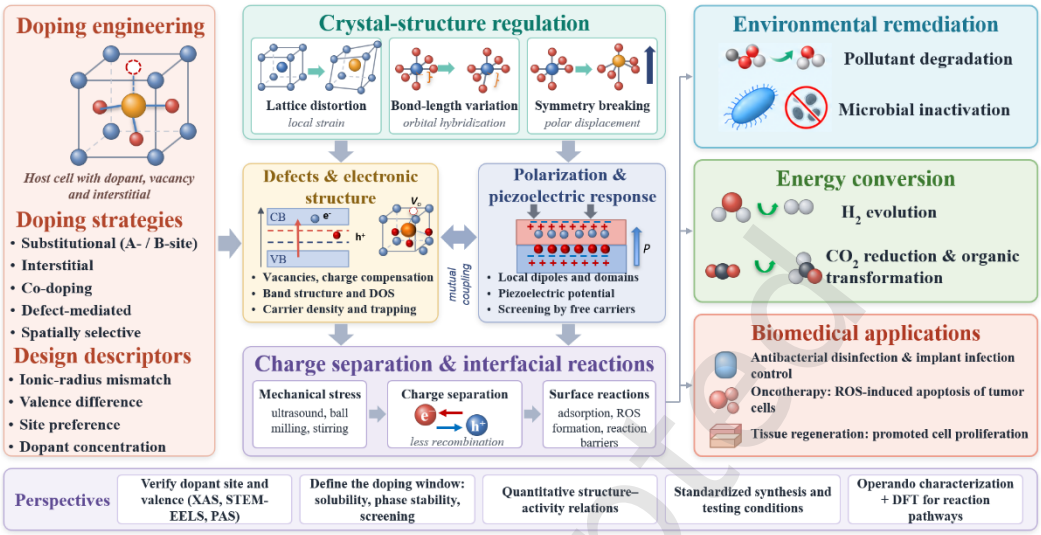


Figure 2 Schematic illustration of the mechanisms and applications of doping engineering in piezocatalysis.

2.1 Doping method

The choice of doping method plays a crucial role in determining dopant incorporation, defect formation, elemental distribution, and ultimately the piezocatalytic performance of the resulting materials[51, 69]. As illustrated in **Figure 3**, the fundamental difference among various doping methods lies in the stage at which dopant species participate in material formation and the pathways through which they are incorporated into the host lattice. From an atomic perspective, dopant incorporation involves migration to energetically favorable lattice sites, followed by local lattice relaxation and charge compensation to minimize the free energy of the system[67, 69]. Precursor-mediated methods, including hydrothermal synthesis, sol-gel processing, electrospinning, and thermal decomposition, introduce dopant species before or during crystallization[5, 70-72]. In these approaches, dopant atoms participate directly in nucleation and crystal growth, enabling lattice incorporation as the host structure forms. Because long-range solid-state diffusion is largely avoided, precursor-mediated routes generally provide relatively homogeneous dopant distributions and good compositional uniformity. Homogeneous co-precipitation also provides a solution-based approach for controlling the composition and particle size of doped oxide powders, as demonstrated in the preparation of scandia-stabilized zirconia

Just Accepted

submicron powders[73]. Moreover, electrospinning offers the additional advantage of constructing one-dimensional architectures that facilitate polarization alignment and directional charge transport[74, 75].

In contrast, solid-state reactions rely on thermally activated diffusion after the host lattice has already formed[51]. Dopant incorporation is therefore governed by diffusion kinetics, lattice solubility, and defect chemistry, resulting in a stronger dependence on sintering temperature and processing time[53, 76]. Owing to their simplicity and scalability, solid-state methods remain widely employed for ceramic piezoelectric materials despite their relatively limited control over dopant homogeneity[50, 51, 53]. Moreover, the crystal structure of precursor materials can influence solid-state diffusion, phase evolution, and the resulting piezoelectric properties. For example, the crystal form of Nb_2O_5 was demonstrated to affect the sintering behavior and electrical properties of (K,Na)NbO_3 (KNN)-based ceramics[77].

Thin-film deposition techniques, such as chemical vapor deposition (CVD), magnetron sputtering, and pulsed laser deposition (PLD), represent another important category of doping methods[5, 78]. Unlike diffusion-controlled approaches, these techniques incorporate dopant species simultaneously with film growth under non-equilibrium conditions, allowing precise regulation of dopant concentration, crystallographic orientation, interface structure, and defect distribution[5]. Such characteristics make them particularly suitable for piezoelectric thin films and integrated devices[78].

Other specialized approaches, including ion implantation, in-situ polymerization, co-precipitation[79], impregnation-calcination[80], microwave-assisted synthesis[81], and plasma-induced doping[82], further expand the available doping strategies for specific material systems[83, 84]. Ion implantation enables localized dopant incorporation, potentially beyond equilibrium solubility limits, while in situ polymerization facilitates the regulation of molecular interactions, dipole orientation, and phase composition in polymer-based piezoelectric materials [83-85]. Co-precipitation promotes the simultaneous precipitation of host and dopant species, whereas impregnation-calcination involves the introduction of dopant precursors followed by thermal treatment. Microwave-assisted synthesis enables rapid and relatively uniform heating, while plasma-induced doping facilitates dopant incorporation through interactions with energetic plasma species. A comparison of representative doping methods, together with their characteristics, advantages, limitations, and typical applications, is summarized in **Table 1**.

Just Accepted

Regardless of the synthesis route, the essential objective of doping is to achieve stable incorporation of foreign atoms into the host material while simultaneously regulating the local crystal environment and defect chemistry[27, 38, 67]. The resulting differences in dopant distribution, lattice evolution, and defect formation provide the structural basis for the modulation of electronic structure and piezoelectric polarization, which will be discussed in the following sections[27, 51].

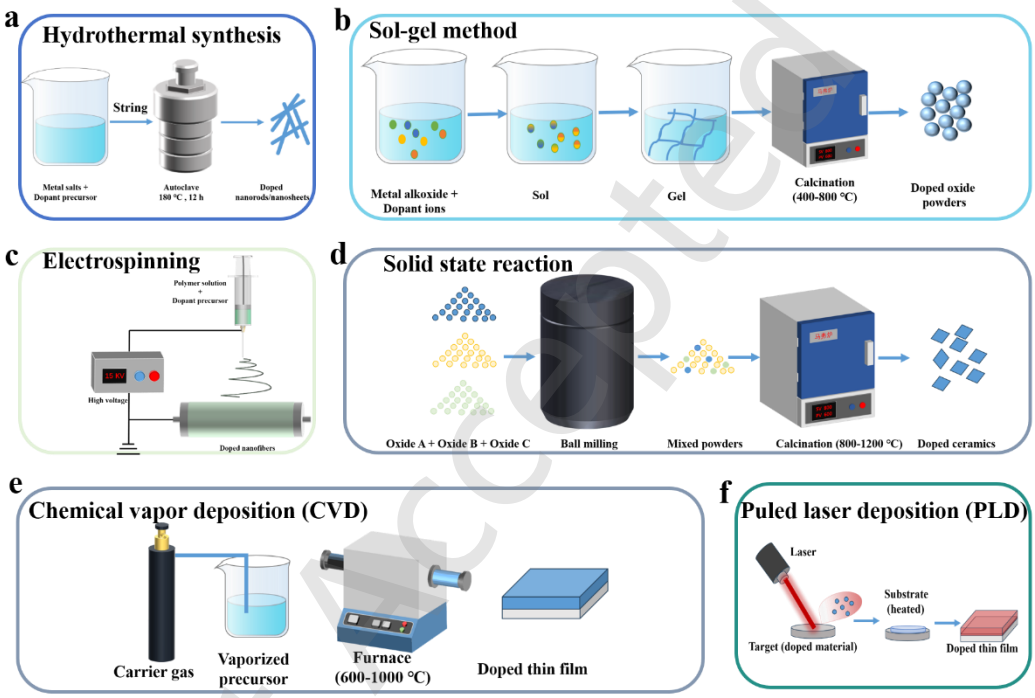


Figure 3 Representative doping methods for piezoelectric materials. (a) Hydrothermal synthesis, (b) sol-gel method, (c) electrospinning, (d) solid-state reaction, (e) chemical vapor deposition (CVD), and (f) pulsed laser deposition (PLD).

Just Accepted

Table 1 Comparison of representative preparation methods for doped piezoelectric materials, including their processing characteristics, dopant-introduction mechanisms, advantages, limitations, critical parameters, and reported piezoelectric responses.

Synthesis method	Method characteristics	Dopant introduction	Advantages	Limitations	Key synthesis points	d_{33} change after doping/modification	Ref.
Hydrothermal synthesis	Solution-based crystal growth; nanoparticles, nanorods, and nanosheets	Dopant-containing precursors introduced during nucleation and crystal growth	Mild conditions; low cost; morphology control	Unclear dopant sites; surface adsorption	Control pH, mineralizer, precursor ratio, temperature, and time	ZnO bulk: ~12.4 pm/V; La-ZnO: 100.3 pm/V; Y-ZnO nanosheets: up to ~420 pm/V	[70]
Sol-gel method	Molecular-level mixing; powders/films	Dopant precursors incorporated into the sol before gel formation	High compositional homogeneity; stoichiometry control; films and powders	High homogeneity; tunable stoichiometry	Control pH, chelating agent, viscosity, drying, and calcination	Sm-PZT thin films: 61.5-279.9 pm/V	[71]
Electrospinning	Oriented nanofibers; polymer composites	Dopant precursors or functional fillers mixed into spinning solution	One-dimensional structures; large surface area; fiber morphology control	Filler aggregation; composite-type doping	Control viscosity, voltage, distance, humidity, and filler dispersion	ZnO(10 wt%)/PVDF fibers: output voltage ~2.5x that of PVDF, beta-phase 52.8% (d_{33} not reported); PVDF/GO (1.5 wt%) nanofibers:	[86]

Just Accepted

						d_{33} ~55.6 pC/N	
Pulsed-laser deposition, PLD	Physical vapor deposition through pulsed laser ablation	Doped targets or controlled multi-target deposition	Orientation control; compositional transfer; dense films	Expensive; small area; droplets	Control laser fluence, oxygen pressure, substrate temperature, and annealing	PLD-grown PZT films: d_{33}, f (max.) 126 pm/V (undoped) to 164 pm/V (Nb-doped)	[5]
Solid-state reaction	High-temperature diffusion; bulk ceramics	Dopant-containing powders incorporated through thermally activated solid-state reactions and diffusion	Mature process; scalable; suitable for bulk ceramics	High temperature; volatilization; compositional inhomogeneity; secondary phases	Control milling, calcination, sintering, holding time, and poling	Sm^{3+}-modified KNLN-BZ-BNT: d_{33} increased to 325 pC/N; d_{33} reached 384 pm/V	[87]
Magnetron sputtering	In-situ film doping; thin films	Doped targets or co-sputtering from separate targets	Film-thickness and orientation control; compatible with microfabricat	Equipment-intensive; composition deviations; phase and defect sensitivity	Control RF power, Ar/O_2 ratio, substrate temperature, and thickness	V-$LiNbO_3$ films: 4.76 (undoped) to 13.5 pC/N (V/Nb = 0.07)	[88]

Just Accepted

			ion				
Chemical vapor deposition, CVD	Film or nanostructure growth from vapor-phase precursors	Dopant-containing vapor precursors supplied during growth	High crystallinity; conformal deposition; controllable growth	Precursor compatibility; narrow processing window; difficult dopant control	Control precursor flow, temperature, carrier gas, oxygen pressure, and substrate	Direct d_{33} values are rarely reported; enhancement is usually shown by device output or sensitivity	[89]
Ion implantation	Energetic ion injection; near-surface doping	Dopant ions implanted into the host followed by possible annealing	Localized modification; depth and dose control	Lattice damage; residual stress; limited implantation depth	Ion species, energy, fluence, implantation temperature, annealing	Ti-implanted AlN: d_{33} increased by about 30%	[90]
In-situ polymerization doping	In-situ filler dispersion; PVDF composites	Dopant-like additives or fillers incorporated during polymer formation	Good filler dispersion; interfacial interactions; phase regulation	Usually composite modification rather than substitutional lattice doping	Filler loading, polymerization temperature, monomer ratio, dispersion	AgF/Ag_2O-PVDF: d_{33} increased by about 50%, approximately d_0-1.5 d_0; β-PVDF reached 91.4%	[91]
Thermal	Precursor	Mixed host	Simple	Agglomeration;	Control heating rate,	Direct d_{33} values	[92]

Just Accepted

decomposition	decomposition; oxide nanoparticles	and dopant precursors decomposed and crystallized	processing; potential compositional mixing; nanoparticle production	secondary phases; incomplete decomposition	decomposition temperature, holding time, and atmosphere	are rarely reported; improvement is usually reflected by β-phase content, output voltage/current, or dielectric response	
Plasma-induced doping	Plasma-assisted modification of MoS_2 to achieve p-type conductivity	Plasma-induced electronic modification of MoS_2	Direct carrier-type modulation; formation of p–n heterojunctions; compatibility with thin-film devices	Plasma conditions require optimization; potential plasma-induced surface damage	Plasma treatment conditions, MoS_2 thickness, interfacial contact and carrier concentration	Not reported	[93]
Co-precipitation	Simultaneous precipitation of metal precursors followed by washing and drying	Co incorporation into $BaTiO_3$ lattice	Good compositional homogeneity; controllable doping concentration; simple processing	Sensitive to precipitation conditions; possible agglomeration	Control precursor ratio, reaction temperature, and precipitation conditions	Not reported	[79]
Impregnation-calcination	Impregnation of the host material with dopant	Fe-N coordination formation within the g-	Simple operation; flexible loading;	Dopant loading and calcination temperature require	Control precursor concentration, impregnation time, drying, and calcination	Not reported	[80]

Just Accepted

	precursors followed by drying and thermal treatment	C_3N_4 framework	effective interfacial modification	optimization	temperature		
Microwave-assisted synthesis	Rapid volumetric heating during precursor reaction and ceramic processing	Li/Ta/Sb incorporation into KNN-based perovskite through precursor stoichiometric control	Rapid processing; reduced reaction time; potentially improved energy efficiency	Possible secondary phases, porosity, and nonuniform heating	Optimize microwave power, temperature, holding time, and precursor composition	15 pC/N (microwave-sintered); 146 pC/N (conventionally sintered comparison)	[81]

Note: The piezoelectric coefficients are reported using the units and measurement methods provided in the original studies. Values obtained from Berlincourt-type measurements ($pC \cdot N^{-1}$) and local piezoresponse force microscopy measurements ($pm \cdot V^{-1}$) are not directly interchangeable and should be interpreted in the context of their respective measurement conditions.

Just Accepted

2.2 Doping type

Beyond synthesis routes, the regulatory effect of doping is largely determined by intrinsic dopant descriptors, including valence state, ionic radius, electronegativity, preferred lattice occupation[27], and concentration. Among these factors, doping type is a primary descriptor because it defines the initial defect-compensation pathway, carrier polarity[51], electronic transport behavior, and piezocatalytic response. According to the valence relationship between dopants and host ions, doping can generally be divided into heterovalent and isovalent substitution[50]. Heterovalent doping directly introduces charge imbalance and compensating defects, thereby regulating free-carrier concentration and enabling n-type or p-type conduction. Isovalent doping does not nominally change the charge state, but it can still modulate carrier polarity and defect formation through differences in ionic radius[94, 95], electronegativity, bonding configuration, or defect formation energy[96]. For mechanistic clarity, these strategies are discussed separately according to their valence relationships, dopant combinations, defect interactions, and spatial distributions.

2.2.1 Heterovalent doping

Heterovalent doping involves substituting host ions with dopants of different valence states, thereby modifying charge balance, defect chemistry, and electronic structure. Charge compensation may occur through ionic vacancies, changes in carrier concentrations, or adjustments in neighboring ionic oxidation states. These changes can influence defect energy levels, carrier transport, and local electric fields. Meanwhile, differences in ionic radius and site occupation may induce lattice distortion and modify polarization behavior. For example, Wang et al. demonstrated that Al^{3+} doping in (Ba,Ca)(Zr,Ti)O_3 (BCZT) ceramics induced concentration-dependent site occupation and lattice distortion, resulting in an enhanced piezoelectric coefficient of 638 pC N^{-1}[34]. Similarly, investigations of Dy-doped $BaTiO_3$ ceramics have revealed that concentration-dependent dopant-site occupation can modify charge-compensation pathways, grain-boundary defects, and potential barriers, emphasizing the importance of dopant-site selection in regulating the electrical properties of functional oxides[97]. Nevertheless, excessive free carriers or charged defects may increase leakage conductivity and screen polarization-induced electric fields, highlighting the importance of optimizing dopant concentrations.

Just Accepted

2.2.2 Isovalent doping

Isovalent doping introduces dopants with the same nominal valence as the substituted host ions, primarily modifying local coordination, chemical bonding, and structural symmetry without necessarily requiring charge-compensating defects. Changes in ionic radius and electronegativity can regulate orbital hybridization, band-edge characteristics, and polarization configurations. For instance, Cui et al. demonstrated that Ca^{2+} substitution in $Sr_2Nb_2O_7$ induced rotational distortion of Nb-O octahedra, enhancing the piezoelectric response and carrier dynamics. The optimized catalyst achieved an H_2O_2 production rate of 168 μmol g^{-1} h^{-1}, more than four times that of pristine $Sr_2Nb_2O_7$ [98]. Isovalent substitution can improve piezocatalytic performance through coordinated structural and electromechanical regulation rather than direct carrier introduction through formal valence imbalance.

2.2.3 Co-doping

Co-doping introduces two or more dopant species to achieve coordinated regulation of defect chemistry, electronic structure, and polarization. Appropriate dopant combinations may alter charge-compensation pathways, stabilize favorable structural configurations, and improve carrier transport. Gao et al. demonstrated that multi-element doping in KNN-based ceramics promoted tetragonal-phase formation and high-density nanoscale heterostructures with low-angle polar vectors, yielding an enhanced piezoelectric coefficient of 520 pC N^{-1} [99]. Furthermore, co-doping combined with phase-boundary and defect engineering in $BaTiO_3$-based ceramics was reported to improve carrier separation and piezocatalytic degradation kinetics[100]. These findings illustrate the potential of co-doping to simultaneously optimize polarization behavior and charge-transfer processes. However, competing dopant interactions, defect clustering, and secondary-phase formation may limit the synergistic benefits.

2.2.4 Defect-mediated doping

Defect-mediated doping emphasizes the interactions between dopants and intrinsic defects, particularly oxygen vacancies, cation vacancies, and dopant–defect complexes. These interactions can modify defect energy levels, carrier trapping, charge separation, and interfacial reaction pathways. In addition, charged defect complexes may form local dipoles and influence polarization stability. Wei et al. reported that Ce-regulated defect

Just Accepted

engineering in hollow $BaTiO_3$ nanoparticles promoted oxygen-vacancy formation, enhanced polarization, and improved electron–hole separation, thereby strengthening piezocatalytic tumor therapy [101]. Nevertheless, excessive defects may introduce deep-level trapping and recombination centers or cause electric-field screening. Therefore, controlling defect concentration and configuration is essential for balancing carrier transport and effective polarization.

2.2.5 Spatially selective doping

Spatially selective doping focuses on controlling dopant distributions within specific regions, including surfaces, interfaces, grain boundaries, and compositionally graded structures. Unlike homogeneous doping, spatially nonuniform dopant incorporation may create local variations in electronic potential, band bending, carrier concentration, and strain distribution. Such variations can potentially facilitate directional carrier transport, interfacial charge extraction, and local polarization redistribution. Spatially graded oxygen-vacancy engineering in $NiTiO_3/TiO_2$ heterostructures has recently demonstrated the significance of defect spatial distribution in regulating piezoelectric polarization and catalytic reaction dynamics [102]. Although this study concerns spatial defect engineering rather than direct substitutional dopant-gradient engineering, it provides relevant mechanistic support for spatially resolved regulation. Direct experimental verification of dopant location, local electronic structure, and polarization remains necessary to establish the effectiveness of spatially selective doping in piezocatalysis.

Overall, these strategies are complementary rather than mutually exclusive. Heterovalent and isovalent doping describe the valence relationship between dopants and host ions, whereas co-doping, defect-mediated doping, and spatially selective doping emphasize dopant combinations, defect interactions, and spatial distributions, respectively. Their effects on piezocatalytic performance are governed by the coupled regulation of electronic structure, carrier transport, polarization, and interfacial reaction kinetics.

3 Doping influence factors

Doping-regulated piezocatalysis is governed by multiple interconnected factors rather than a single material parameter. To clarify the underlying mechanisms, this section is organized into five aspects: crystal-structure regulation, defect chemistry and charge-carrier behavior,

Just Accepted

piezoelectric properties, potential adverse effects of excessive doping, and doping-regulated catalytic pathways. Sections 3.1-3.3 discuss the effects of dopant incorporation on lattice distortion, bond-length variations, symmetry breaking, defect evolution, electronic structure, and polarization behavior. Section 3.4 examines the detrimental effects of excessive doping, whereas Section 3.5 connects these material-level modifications with reactant adsorption, interfacial charge transfer, reaction energetics, and rate-determining steps. Together, these discussions establish the relationships among dopant characteristics, structural and electronic regulation, and piezocatalytic performance.

3.1 Crystal structure

3.1.1 Lattice distortion

Lattice distortion describes the overall structural response of a host lattice to dopant incorporation, including changes in lattice parameters, local strain, and coordination-polyhedron geometry[51, 103]. At this scale, the focus is on the spatial extent and magnitude of structural deformation rather than individual bond-length changes or the resulting symmetry state. Dopant-induced distortion originates from factors such as ionic-radius mismatch, charge compensation, and local structural relaxation, and its effects on piezoelectric response depend on the host lattice and doping concentration. It converts ionic-size mismatch, charge imbalance, and defect compensation into crystallographic asymmetry and local strain, thereby modifying polarization behavior and enhancing the piezoelectric response. Therefore, lattice distortion can be regarded as an intermediate link between dopant-induced defect chemistry and macroscopic piezoelectric or piezocatalytic performance[51]. Cheng et al. reported that Al^{3+} doping in BCZT ceramics induces a non-monotonic evolution of lattice distortion, with the most pronounced structural distortion observed at an optimal doping concentration of 0.25 mol% (**Figure 4a**) [34]. Synchrotron X-ray diffraction (XRD) patterns exhibited significant peak broadening, indicating enhanced lattice distortion and structural heterogeneity **(Figure 4b**). Furthermore, quantitative phase analysis reveals the coexistence of rhombohedral (R3m), orthorhombic (Amm2), and tetragonal (P4mm) phases, with the tetragonal-phase fraction increasing from 38.1% to 46.0% at x = 0.25 before decreasing at higher compositions **(Figure 4c)**, indicating composition-dependent phase redistribution and structural evolution. However, further increasing the Al content resulted in excessive lattice distortion and structural

Just Accepted

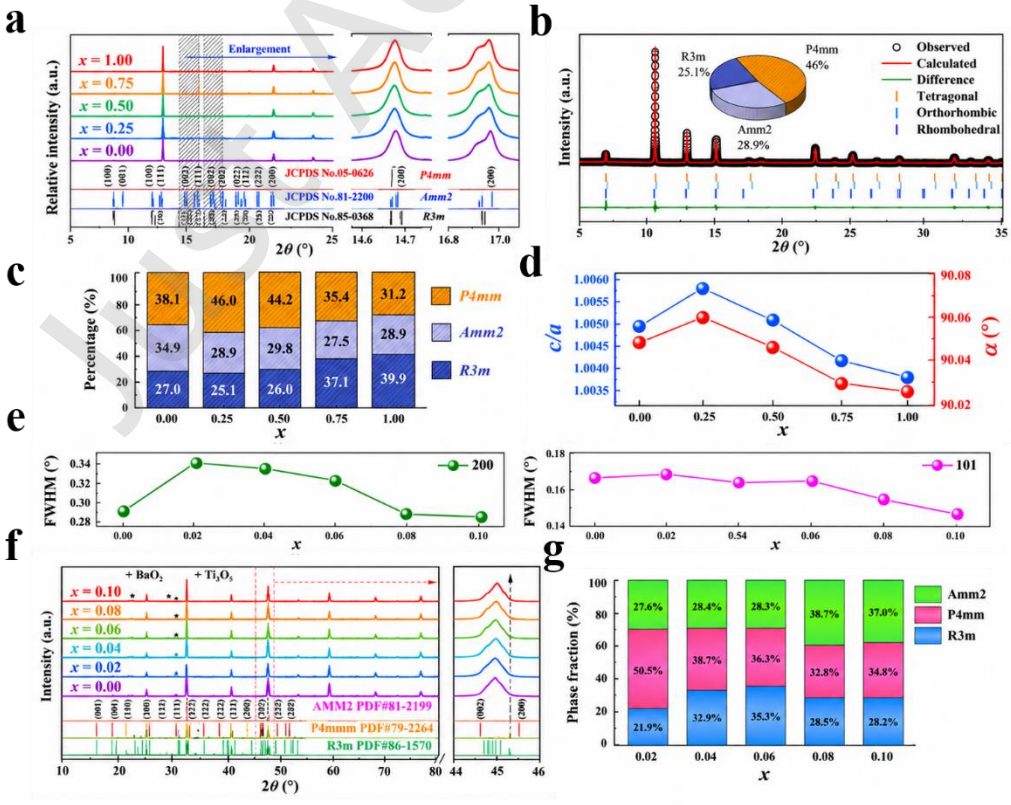
disorder, suggesting that dopant-induced lattice distortion should be maintained within an appropriate range to achieve favorable structural regulation. The non-monotonic evolution of lattice distortion can be understood as a competition between beneficial local structural modulation and excessive lattice destabilization. At low dopant concentrations, ionic-radius mismatch and charge-compensation effects generate local strain and asymmetric atomic displacement, which can enhance polarization-related responses. As the dopant concentration increases, overlapping local distortions may lead to accumulated internal stress, structural heterogeneity, and eventually a loss of lattice stability. Therefore, the optimal concentration corresponds to a balance between sufficient local distortion and preservation of the host crystal structure, rather than the maximum achievable lattice distortion. In ZnO-based piezocatalysts, dopant-induced local distortion mainly originates from ionic-radius mismatch and modified coordination environments. Due to the size and valence mismatch between Zn^{2+} and Sb^{3+}/Sb^{5+}, Sb dopants tend to induce off-center local coordination and modify Zn-O bond polarity[104]. This local distortion generates permanent dipoles and ferroelectric-like behavior **(Figure 4d)**, leading to enhanced piezoelectric output voltage **(Figure 4e)**. Similar lattice-distortion effects have also been observed in layered SnS_2-based systems. Fe doping induces pronounced lattice distortion in SnS_2 by introducing local structural strain and lattice deformation, with the most significant distortion observed for $Sn_{0.97}Fe_{0.03}S_2$[105]. These results further demonstrate that appropriate dopant incorporation can effectively tailor the local crystal structure through lattice distortion. In Cu- or Ag-doped SnS_2, ionic-size mismatch and charge imbalance induce lattice distortion, sulfur-vacancy formation, and increased carrier concentration [59]. These examples collectively suggest that dopant-induced local strain can strengthen structural asymmetry, enhance dipole polarization, and promote piezoelectric charge generation, especially in non-centrosymmetric or low-dimensional piezocatalysts.

Notably, doping does not always enhance piezoelectricity by simply increasing lattice distortion[106]. In some systems, performance improvement may instead arise from the redistribution or relaxation of local structural distortion and the optimization of phase coexistence. For example, multi-element doping in KNN-based ceramics induces composition-dependent structural evolution, as evidenced by changes in the XRD

Just Accepted

diffraction patterns **(Figure 4f)**[99]. Quantitative phase analysis further reveals variations in the relative fractions of rhombohedral (R3m), orthorhombic (Amm2), and tetragonal (P4mm) phases with increasing dopant concentration **(Figure 4g)**, indicating doping-induced phase redistribution and structural regulation. Such phase evolution may facilitate polarization reorientation by modifying the relative stability of competing ferroelectric phases, thereby contributing to improved piezoelectric performance. These findings suggest that the role of doping extends beyond increasing local lattice distortion to optimizing phase stability, structural symmetry, and polarization responsiveness. Therefore, an appropriately regulated structural state may be more beneficial than excessive static lattice distortion.

Overall, lattice distortion should be regarded as a tunable structural descriptor rather than a quantity to be maximized. Appropriate distortion can modify local coordination environments while preserving structural integrity, whereas excessive distortion may introduce disorder or destabilize the host lattice. The associated atomic-scale changes are further examined through bond-length redistribution in Section 3.1.2, while their potential effects on crystallographic symmetry are discussed in Section 3.1.3.



Just Accepted

Figure 4 Doping-induced lattice distortion and phase evolution in piezoelectric materials. (a) Synchrotron XRD patterns of Al-doped BCZT ceramics. (b) Rietveld refinement and phase composition. (c) Evolution of rhombohedral, orthorhombic, and tetragonal phase fractions. (d) Changes in lattice parameters (c/a and α) with Al doping concentration. Copyright 2022 Elsevier[34]. (e) Doping-dependent XRD peak broadening of Sm-doped BCZT ceramics. (f) XRD patterns showing structural evolution and secondary-phase formation. (g) Evolution of phase fractions with Sm doping concentration. Copyright 2026 American Chemical Society[107].

3.1.2 Chemical bond length change

At the atomic scale, bond-length redistribution provides a more localized descriptor of the lattice distortion discussed in Section 3.1.1. Dopant ions with different ionic radii, valence states, and bonding preferences can elongate or shorten neighboring metal-oxygen or metal-sulfur bonds, producing changes in bond-length distributions, coordination geometry, and orbital overlap[27, 51, 69]. Unlike the overall lattice distortion described in Section 3.1.1, bond-length analysis focuses on the magnitude and anisotropy of individual interatomic distances and their consequences for local bonding and electronic structure. These changes can influence orbital hybridization, charge localization, and defect energetics, thereby providing an atomic-scale link between dopant incorporation and material properties[27, 51, 69].

In oxide-based catalytic systems, bond-length modulation strongly influences local bonding interactions and charge-transfer properties. For example, Ru incorporation in $Bi_4O_5Br_2$ shortens the Bi-O bond from 2.219 to 2.192 Å and the Ru-O bond from 2.404 to 1.956 Å, indicating enhanced orbital overlap and strengthened local bonding interactions [108]. Such bond contraction can facilitate charge transfer and improve polarization response. In perovskite-related Nb-O frameworks, oxygen-vacancy regulation induces gradual structural reconstruction of the BO_6 octahedra, accompanied by variations in local bond lengths and coordination environments (**Figure 5b-f**)[42]. These structural changes reduce local symmetry and increase polarization flexibility. Similarly, Y doping in CeO_2 causes local bond contraction because of the smaller ionic radius of Y compared with Ce^{4+}, which contributes to particle-size reduction, nanorod formation, increased surface area, and

Just Accepted

enhanced oxygen-vacancy concentration[43]. These examples indicate that bond-length modulation is not merely a local structural change, but a key factor governing coordination distortion, polarization response, and catalytic activity.

Bond-length variation is closely coupled with defect formation and local coordination reconstruction. As illustrated in **Figure 5a**, Mn substitution in ZnO modifies the local metal–oxygen coordination environment and induces distortion of the ZnO_4 tetrahedra, while the introduction of oxygen vacancies further promotes neighboring atomic relaxation and bond-length redistribution [38]. Similarly, oxygen-vacancy engineering in BNT modifies the local coordination of TiO_6 octahedra **(Figure 5g)**[109]. These examples demonstrate that dopant–defect interactions can induce local bond reconstruction. The resulting defect chemistry and its implications for electronic structure and carrier behavior are discussed in Section 3.2.2.

Beyond modifying local bonding, bond-length redistribution can alter orbital hybridization, the density of states, charge localization, and band-edge positions, thereby influencing carrier migration and interfacial reaction kinetics. At catalytic interfaces, these changes may also affect the adsorption of reactants and intermediates and the associated reaction energy barriers. Importantly, bond-length variation does not necessarily imply symmetry breaking: uniform or symmetry-equivalent bond changes may preserve the original crystallographic symmetry. As discussed in Section 3.1.3, symmetry breaking requires a symmetry-inequivalent arrangement of atomic displacements or local structural units. This distinction separates bond-level structural modification from the emergence of a non-centrosymmetric configuration capable of supporting piezoelectric polarization.

Just Accepted

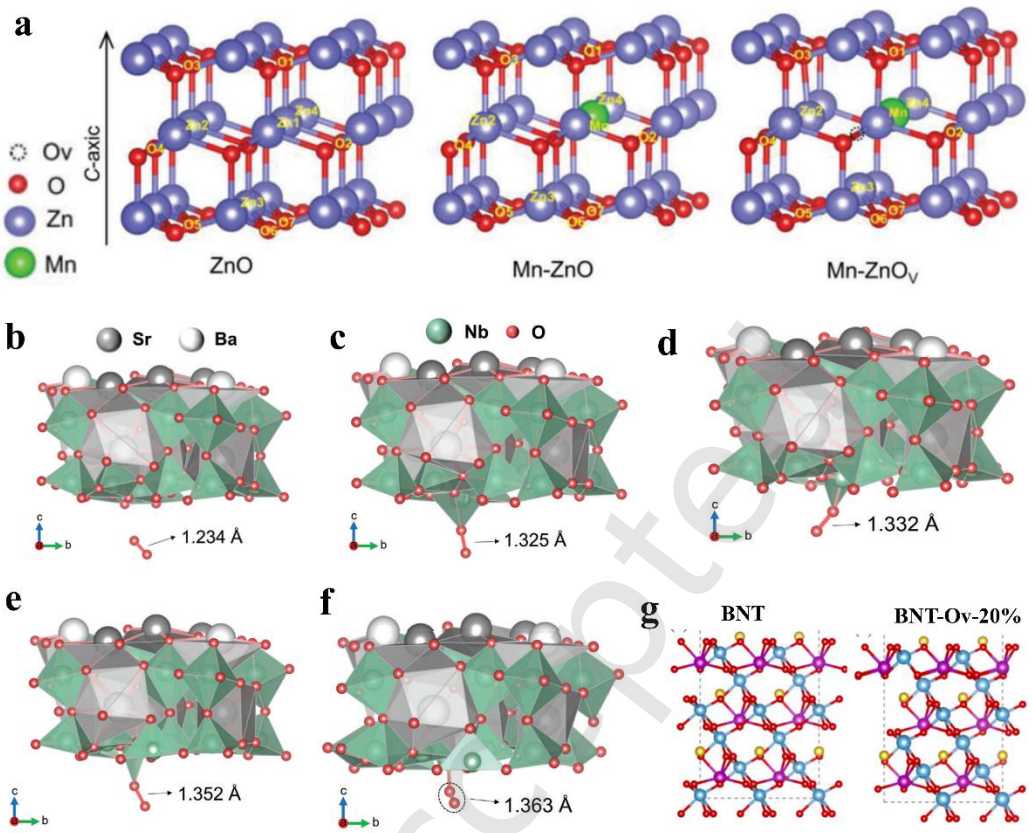


Figure 5 Representative examples of dopant-vacancy coupling and oxygen-vacancy engineering in piezoelectric materials. (a) Atomic structure models of pristine ZnO, Mn-doped ZnO, and Mn-ZnO_V. Copyright 2023 Wiley[38]. (b) Pristine SBN. (c) SBN-1 OV. (d) SBN-2 OV. (e) SBN-3 OV. (f) SBN-4 OV. O_2 adsorption models calculated by DFT. Copyright 2024 Wiley[42]. (g) Crystal structures of pristine BNT and oxygen-deficient BNT (BNT-OV-20%). Copyright 2022 Elsevier[109].

3.1.3 Symmetry breaking

Symmetry breaking refers to a reduction or loss of crystallographic symmetry caused by a symmetry-inequivalent arrangement of atomic displacements, bond distortions, or defect configurations. As discussed in Sections 3.1.1 and 3.1.2, dopant incorporation can induce overall lattice distortion and local bond-length redistribution; however, these structural changes do not necessarily break the original symmetry. Symmetry breaking occurs only when the resulting atomic arrangement no longer preserves the relevant symmetry operations. As illustrated in Figure 7a, the absence of inversion symmetry is a necessary

Just Accepted

condition for piezoelectricity. When doping induces or modifies a non-centrosymmetric configuration, the resulting asymmetric charge distribution and atomic displacements can alter local dipole moments and polarization behavior[110]. Accordingly, symmetry breaking provides a structural basis for modifying piezoelectric coupling and mechanically induced charge separation, rather than an inevitable final stage of lattice evolution.

At the atomic scale, anisotropic bond-length changes and spatially heterogeneous strain can contribute to symmetry breaking when they produce symmetry-inequivalent atomic displacements[111]. As schematically illustrated in **Figure 6a**, non-centrosymmetric structures can generate a net polarization under mechanical stress, whereas centrosymmetric structures exhibit no conventional piezoelectric polarization under the same conditions ($P = 0$). The schematic further illustrates that an applied electric field can couple with mechanical deformation through electrostriction, enabling a polarization response in centrosymmetric lattices. Atomic-scale polar-vector mapping further reveals pronounced spatial variations in local polarization in Sb-doped KNN (**Figure 6b, c**), with distinct compositional regions exhibiting different polar-vector orientations and distributions. These results demonstrate that multi-element doping can generate local polarization heterogeneity and modify the distribution of polar domains. Meanwhile, strain mapping reveals spatially non-uniform lattice deformation **(Figure 6d)**, providing further evidence of local structural heterogeneity. The XRD patterns and corresponding crystal structure illustrate the structural characteristics of different Ba-based perovskite compositions **(Figure 6e)**, while the amplitude and phase hysteresis loops demonstrate their electromechanical switching behavior **(Figure 6f)**. Collectively, these results highlight the important role of crystallographic symmetry, local structural distortion, and dopant-induced heterogeneity in regulating polarization and piezoelectric responses [112].

When symmetry breaking produces or modifies a non-centrosymmetric structure, it can change polarization behavior, piezoelectric coupling, and the internal electric field under mechanical stimulation. These changes may facilitate charge separation and influence piezocatalytic activity, although the magnitude and direction of the effect depend on the host structure, domain configuration, and defect distribution. Together, Sections 3.1.1–3.1.3 establish a causal but non-universal relationship: dopant incorporation can

Just Accepted

induce lattice distortion; bond-length redistribution describes the associated changes at the atomic scale; and symmetry breaking may emerge when these changes produce a symmetry-inequivalent structural arrangement. This framework distinguishes the three structural descriptors while clarifying how they can collectively influence piezoelectric polarization.

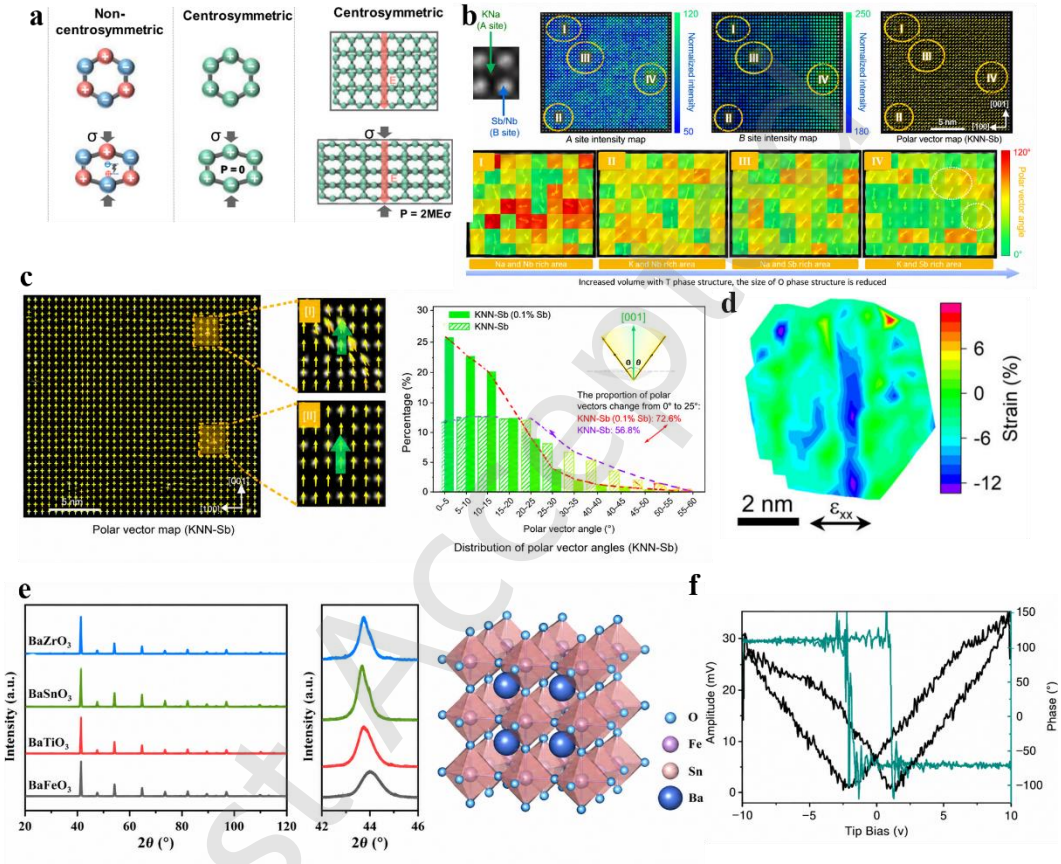


Figure 6 Doping-induced symmetry evolution and its effects on local polarization, lattice strain, and piezoelectric response. (a) Schematic illustration of stress-induced electromechanical responses in non-centrosymmetric and centrosymmetric semiconductors. Copyright 2025 Elsevier[110]. (b, c) Atomic-scale compositional heterogeneity and local polar vector evolution in doped KNN-based ceramics. Copyright 2021 the Author(s)[99]. (d) Nanoscale lattice strain distribution associated with local structural symmetry breaking in multicomponent alloys. Copyright 2026 Wiley[112]. (e) XRD patterns and crystal structure of Fe-doped Ba-based double perovskite oxides, illustrating doping-induced structural evolution. Copyright 2024 Elsevier[113]. (f) PFM

Just Accepted

amplitude and phase responses demonstrating the piezoelectric behavior of Fe-doped double perovskite oxides. Copyright 2024 Elsevier[113].

Beyond atomic-scale crystal-structure regulation, changes in crystal structure and growth behavior can also manifest at larger scales as variations in particle morphology and size. Dopant incorporation may alter local coordination environments, surface energies, and crystal growth kinetics, thereby influencing nucleation, particle aggregation, and morphological evolution. These morphological changes can further affect mechanical stress distribution, polarization behavior, specific surface area, and the availability of catalytic active sites, ultimately influencing piezocatalytic performance. For example, cetyltrimethylammonium bromide (CTAB)-assisted thickness regulation of Bi_2WO_6 nanosheets simultaneously increased the specific surface area and interfacial polarization, demonstrating that morphology optimization can enhance piezocatalytic activity through coupled structural, polarization, and surface effects [30].

For example, Meng et al. reported that La doping slightly increased the average particle size of $BaTiO_3$ from 79.51 to 81.31 nm, accompanied by enhanced piezocatalytic degradation performance **(Figure 7a, b)**. This improvement was associated with the combined effects of structural distortion, surface properties, and defect regulation rather than particle-size variation alone [114]. Similarly, Ce doping induced morphological evolution in ZnO from plate-like aggregates to flower-like structures, accompanied by enhanced H_2O_2 production **(Figure 7c, d)**. The morphological changes may provide more accessible surface-active sites and modify the electromechanical response, contributing to improved catalytic activity [115]. Furthermore, La doping in $BiFeO_3$ induces composition-dependent morphological and structural evolution, as illustrated by the TEM images and corresponding structural features of $Bi_{1-x}La_xFeO_3$ nanoparticles (**Figure 7e-h**). The piezocatalytic degradation rate constant exhibits a non-monotonic dependence on La concentration, reaching its maximum at $x = 0.01$ before decreasing at higher doping levels **(Figure 7i)** [97]. These results suggest that the improvement in piezocatalytic performance cannot be attributed solely to morphological changes, but rather reflects the combined influence of crystal structure, defect chemistry, and polarization behavior.

Just Accepted

The influence of particle size on piezocatalysis is further supported by size-dependent studies of $BaTiO_3$. Kalhori et al. demonstrated that decreasing particle size from 2 μm to 50 nm reduces tetragonal distortion and modifies the temperature-dependent piezoelectric response, consequently affecting methyl orange degradation[116]. Furthermore, nanoscale $BaTiO_3$ exhibits size-dependent ferroelectric domain configurations and polarization behavior, indicating that particle-size reduction may alter the effective piezoelectric respons. Therefore, particle size and morphology should be considered alongside lattice distortion, defect chemistry, and polarization when evaluating doping-induced changes in piezocatalytic performance.

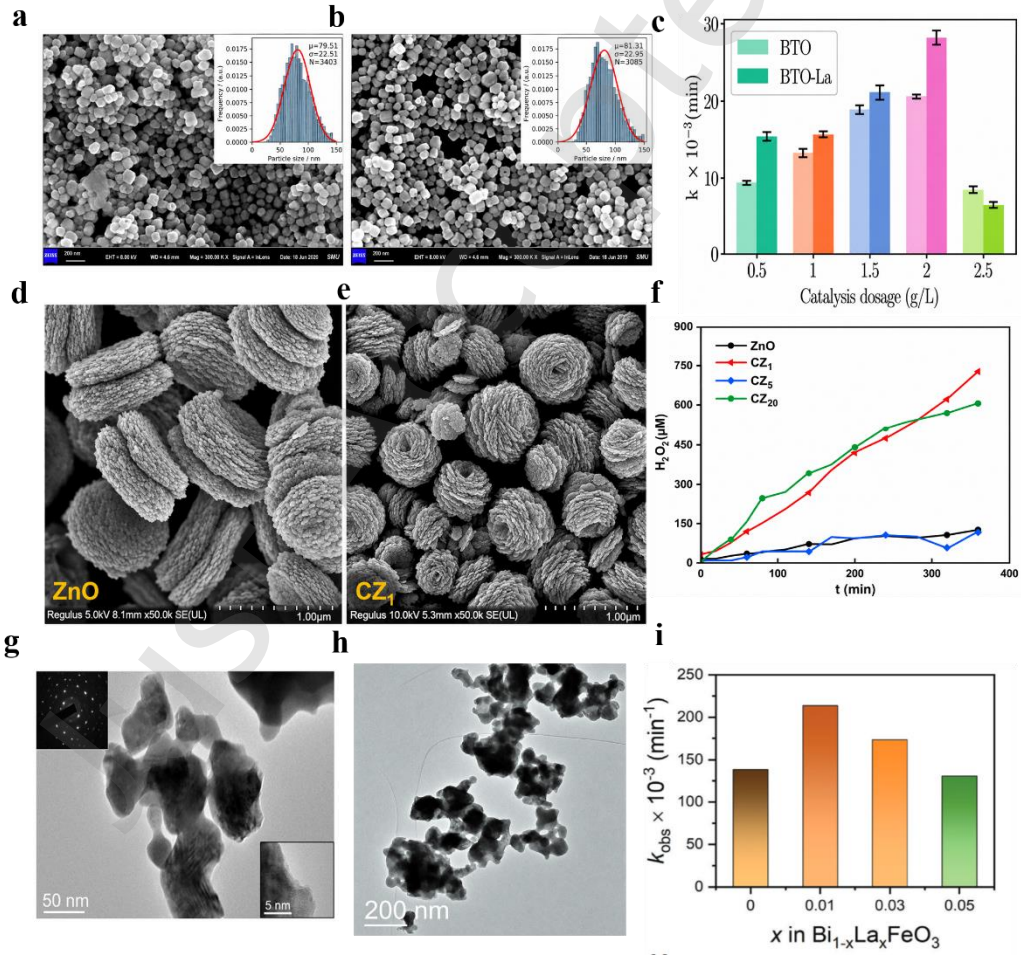


Figure 7 Effects of particle size and doping on piezocatalytic performance. (a) SEM images and corresponding particle-size distributions of pristine and La-doped $BaTiO_3$, respectively. (b) Effect of catalyst dosage on the apparent reaction rate constants

Copyright 2024 the Author(s)[114]. (c) SEM images of pristine ZnO and Ce-doped ZnO

(CZ$_1$). (d) Time-dependent H_2O_2 production over ZnO and Ce-doped ZnO catalysts. Copyright 2025 Elsevier[115]. (e) XRD patterns of $Ba_{1-x}La_xFeO_3$ nanoparticles. (f) TEM image of $Bi_{0.99}La_{0.01}FeO_3$ nanoparticles. (g) Composition-dependent piezocatalytic degradation rate constants. Copyright 2024 the Author(s)[35].

3.2 Defect chemistry and charge-carrier behavior

3.2.1 Band-structure modulation

Following defect formation and lattice-structure evolution, doping-induced electronic band-structure modulation becomes a critical factor in determining piezocatalytic activity. Dopant incorporation can introduce impurity levels, shift the valence-band maximum (VBM) and conduction-band minimum (CBM), tune the band-gap width, and regulate the thermodynamic driving force for surface redox reactions. In general, donor-type dopants tend to generate electronic states close to the conduction band, whereas acceptor-type dopants may introduce states near the valence band. These electronic perturbations directly influence charge redistribution, carrier separation, and the oxidation/reduction capability of piezo-induced electrons and holes. Under mechanical stimulation, piezoelectric polarization generates an internal electric field and induces band bending, which facilitates charge-carrier separation and directional migration toward reactive surface sites. Doping-induced changes in band-edge positions, defect states, and carrier concentration can further regulate charge transport, interfacial charge-transfer kinetics, and the thermodynamic feasibility of surface redox reactions. Importantly, unlike photocatalysis, pure piezocatalysis does not require photon-induced electron excitation across the band gap. Instead, its catalytic performance is governed by the coupled effects of mechanically induced piezoelectric polarization, electronic structure, carrier behavior, and interfacial reaction kinetics. Therefore, band-structure engineering provides an essential connection between atomic-scale doping regulation and macroscopic piezocatalytic performance.

Band-gap modulation is one of the most direct manifestations of doping-induced electronic reconstruction. Pb-doped SnS films provide a representative example of composition-dependent band-gap regulation. As shown in **Figure 8a**, the optical absorption edge of $Sn_{1-x}Pb_xS$ films changes progressively with increasing Pb content,

Just Accepted

indicating that Pb substitution effectively modifies the electronic transition behavior of SnS. The corresponding experimental and calculated band gaps also exhibit a clear Pb-content-dependent variation, as summarized in **Figure 8b**[117]. This band-gap modulation can be attributed to dopant-induced changes in orbital hybridization, lattice distortion, and electronic-state distribution. Such electronic reconstruction not only affects charge excitation but also determines whether mechanically generated carriers possess sufficient redox potential to participate in surface catalytic reactions.

Beyond band-gap regulation, doping can alter interfacial energy alignment and charge-transfer barriers. For example, Co incorporation into $BiFeO_3$ modifies the electronic structure relevant to its contact with Pt. As illustrated **in Figure 8c**, the band alignment of pristine $BiFeO_3$ (BFO) and Co-doped $BiFeO_3$ (BCFO) changes upon Fermi-level equilibration with Pt, leading to distinct Schottky barrier configurations [118, 119]. Under mechanical excitation, the piezoelectric polarization field may further influence local band bending and interfacial carrier migration. This illustration concerns interfacial band alignment under piezoelectric modulation and should not be conflated with light-driven generation and separation of photocarriers.

Dopant identity and occupation environment can also influence band-edge positions and reaction energetics. Ce-doped $BaTiO_3$ provides an example of dopant-associated band-structure modulation, as illustrated in **Figure 8d**. In this context, band-edge shifts and defect-related states should be considered alongside polarization-induced band bending when discussing charge transport and accessible interfacial redox pathways. Additional band-structure examples are presented in **Figure 8e-h**, including sulfur-vacancy-engineered $ZnIn_2S_4$, Sm_2O_3-modified BCZT, oxygen-doped CdS, and a MoS_2-based Schottky junction [107, 120-122]. These systems involve different modification mechanisms, and vacancy engineering or heterojunction formation should not be described as substitutional doping without direct evidence. Their interpretation also requires distinguishing pure piezocatalytic processes from light-assisted processes where applicable.

These findings demonstrate that doping-induced band-structure modulation governs piezocatalysis through multiple interconnected mechanisms, including band-edge alignment, carrier migration, interfacial charge transfer, and reaction-pathway regulation. Under mechanical stimulation, the electronic structure of doped piezocatalysts is further

Just Accepted

modulated by the piezoelectric polarization field, resulting in band bending or band tilting that promotes directional charge separation. Consequently, an optimized band structure should simultaneously possess appropriate band-edge positions and electronic states for target redox reactions, effective coupling with the mechanically induced piezoelectric polarization field, and favorable interfacial reaction pathways, thereby maximizing both catalytic activity and reaction selectivity.

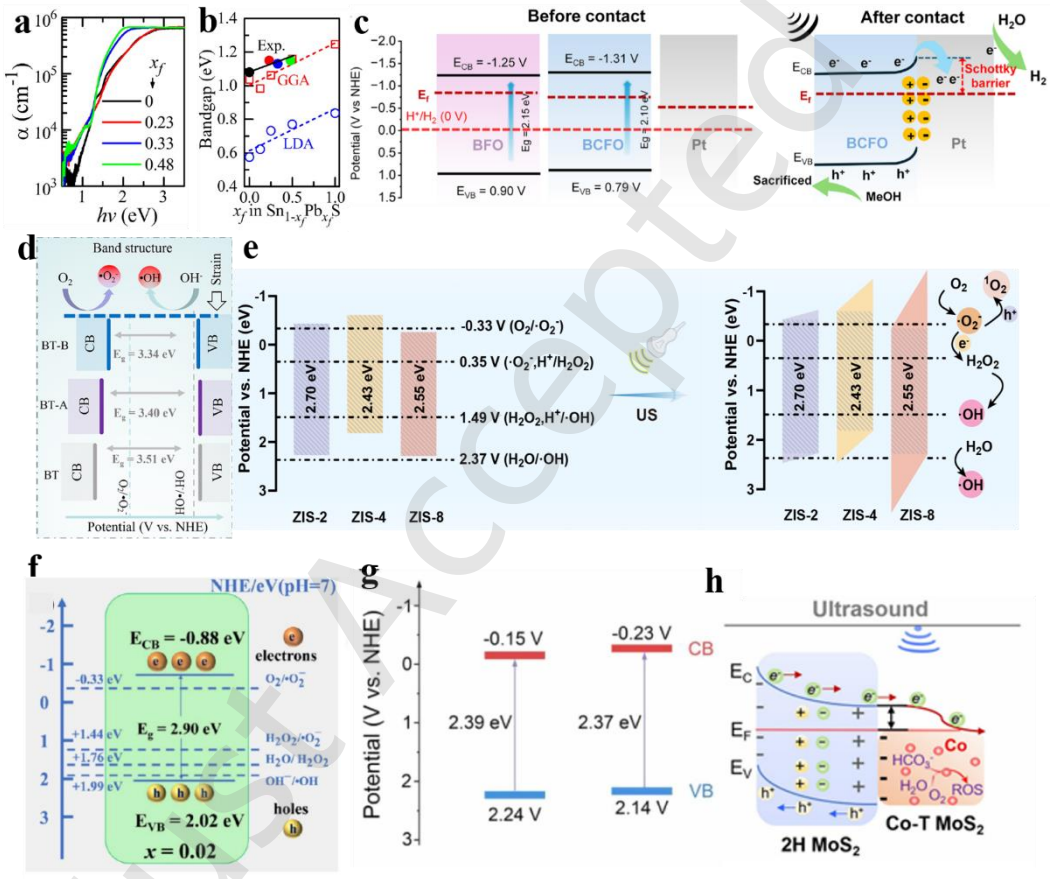


Figure 8 Doping-induced band-structure modulation and charge-transfer mechanisms in piezocatalytic materials. (a, b) Optical absorption spectra and band-gap evolution of Pb-doped SnS films. Copyright 2015 the Author(s)[117]. (c) Band alignment of pristine $BiFeO_3$ and Co-doped $BiFeO_3$ before and after Pt contact, illustrating Fermi-level equilibration and Schottky barrier formation. Copyright 2026 the Author(s)[118]. (d) Band-structure modulation of Ce-doped $BaTiO_3$. Copyright 2024 Elsevier[113]. (e) Band-edge alignment of sulfur-vacancy-engineered $ZnIn_2S_4$ nanosheets under piezoelectric-field modulation. Copyright 2025 Wiley[120]. (f) Energy-band structure of Sm_2O_3-doped BCZT. Copyright 2026 American Chemical Society[107]. (g) Conduction-

Just Accepted

and valence-band edge positions of pristine and oxygen-doped CdS. Copyright 2025 American Chemical Society[121]. (h) Ultrasound-induced charge separation and interfacial electron transfer across the 2H-MoS_2/Co-T/H-MoS_2 Schottky junction. Copyright 2025 American Chemical Society[122].

3.2.2 Dopant-induced defect chemistry

Defects in piezoelectric and piezocatalytic materials can originate from multiple sources and should not be exclusively attributed to doping. Intrinsic defects, including oxygen vacancies, cation vacancies, and interstitial defects, can spontaneously form in undoped materials due to nonstoichiometry and thermodynamic defect equilibria. In bulk ceramics, defect formation is influenced by sintering temperature, oxygen partial pressure, and subsequent thermal treatments, whereas in thin films, deposition conditions, substrate-induced strain, and interfacial interactions can further affect defect formation and redistribution. For example, oxygen-deficient processing conditions may favor oxygen-vacancy formation, while annealing in oxygen-rich atmospheres can reduce their concentration. Therefore, defect formation in piezocatalytic materials is governed by both chemical composition and synthesis conditions. In this context, doping engineering can further regulate defect equilibria and charge-compensation mechanisms by modifying local coordination environments and electronic structures rather than simply introducing additional defects.

Dopant incorporation can disturb the local charge balance and lattice stability of the host material, thereby promoting defect formation or redistribution. Depending on the dopant valence, ionic radius, and host crystal structure, charge compensation may involve cation vacancies, anion vacancies, interstitial defects, or defect complexes[50, 67, 69]. The type and concentration of these defects collectively influence the crystal structure, electronic properties, and ultimately the piezocatalytic performance of the material. Therefore, defects should be regarded not merely as charge-compensation defects but as multifunctional regulators connecting atomic structure with catalytic performance. Recent studies on two-dimensional piezocatalysts have further highlighted the multifunctional roles of defects in modulating piezoelectric polarization, regulating charge-carrier dynamics, and optimizing surface active sites and reaction energetics[123]. Defect

Just Accepted

chemistry is one of the earliest responses of a host lattice to dopant incorporation. In oxide piezocatalysts, aliovalent dopants with mismatched valence states, as well as isovalent dopants with different ionic radii or electronegativities, can induce local charge imbalance and lattice perturbation. These perturbations are frequently compensated by oxygen vacancies, which may function as shallow donor states, defect dipoles, charge-trapping centers, and active sites for molecular adsorption and activation[4, 124, 125]. In Kröger–Vink notation, the main symbol identifies the defect species, the subscript indicates the crystallographic site, and the superscript denotes the effective charge relative to the perfect lattice, where ×, •, and ′ represent neutral, positive, and negative effective charges, respectively. According to Kröger–Vink notation (**Equation 1**), the formation of an oxygen vacancy Vö is accompanied by the release of two electrons[126],

$$O_O^x \rightarrow V\ddot{o} + \frac{1}{2}O_2 + 2e^- \quad (1)$$

where O_O^x represents an oxygen ion occupying its regular lattice site, $V_O^{\cdot\cdot}$ denotes an oxygen vacancy with two positive effective charges, and e^- represents an electron. The equation describes oxygen-vacancy formation accompanied by the release of electrons and molecular oxygen[126]. These excess electrons can participate in charge compensation, modify carrier density, and influence the electronic structure and polarization behavior of piezocatalysts.

Among the intrinsic defects in oxide piezocatalysts, oxygen vacancies are particularly important because their formation can be driven by both synthesis conditions and doping-related charge compensation. In undoped materials, oxygen vacancies may arise from oxygen-deficient environments, nonstoichiometry, or thermal treatments. Meanwhile, aliovalent substitution can further promote or suppress oxygen-vacancy formation depending on the charge-compensation mechanism and defect formation energy. Consequently, oxygen-vacancy concentrations should be understood as the result of coupled compositional and processing effects rather than being attributed exclusively to dopant incorporation. High-resolution O 1s X-ray photoelectron spectroscopy (XPS) spectra can provide evidence of oxygen-vacancy-related chemical environments and their evolution following doping or processing treatments. XPS is widely used to investigate dopant-induced changes in oxygen chemical environments and oxygen stoichiometry. As schematically illustrated in **Figure 9a**, XPS provides complementary information on cation

Just Accepted

valence states, oxygen stoichiometry, and electronic chemical potential. For example, O 1s spectra reveal dopant-dependent variations in oxygen-related components in Nd-Ba ($Ti_{0.2}Zr_{0.2}Sn_{0.2}Nb_{0.2}Nd_{0.2}$) O_3 (BTZSN) and Yb-BTZSN ceramics (**Figure 9b**)[35, 127, 128]. Similar changes in oxygen chemical environments are observed in BNT-based ceramics, as evidenced by the O 1s spectra of $(Bi_{0.5}Na_{0.5})TiO_3$ (BNT) and BNT-Er (**Figure 9c**) [129]. In La-doped $BiFeO_3$, electron paramagnetic resonance (EPR) spectra exhibit concentration-dependent signals, including characteristic features at $g \approx 2.0021$ and $g \approx 2.0159$, indicating changes in paramagnetic defect environments (**Figure 10d**) [35]. A characteristic EPR signal at $g \approx 2.003$ is also observed in Ba (Zr_xTi_{1-x}) O_3 (BZT) ceramics (**Figure 9e**) and BNT-based ceramics (**Figure 9f**) [130, 131], providing complementary evidence of defect-related paramagnetic centers. Raman spectroscopy further reveals dopant-dependent changes in lattice vibrational modes and structural disorder in La-doped $BiFeO_3$ (**Figure 9g**) and BZT ceramics (**Figure 9h**) [35, 130]. Collectively, these spectroscopic results indicate that doping can alter oxygen-related chemical environments, local lattice structures, and paramagnetic defect states, potentially influencing polarization behavior, carrier dynamics, and piezocatalytic performance.

Beyond oxygen and sulfur vacancies, other defects, including cation vacancies, halogen vacancies, interstitial defects, and defect complexes, can also influence the structural and electronic properties of piezocatalytic materials[132, 133]. For example, Zn vacancies in ZnO, Ti vacancies in $BaTiO_3$, and iodine vacancies in halide piezoelectric materials have been reported to modify local coordination environments, electronic states, and polarization behavior[132-134] Although these defects have received comparatively less attention than oxygen and sulfur vacancies in piezocatalysis, they offer additional possibilities for regulating defect chemistry and charge-carrier behavior.

Overall, defect chemistry provides an important link between dopant incorporation, crystal structure, electronic properties, and piezocatalytic performance. Both intrinsic and doping-modulated defects can influence carrier trapping, charge transport, polarization screening, and interfacial reaction kinetics. Therefore, future studies should move beyond oxygen-vacancy-centered interpretations toward defect-specific design strategies that consider defect type, concentration, spatial distribution, and interactions with piezoelectric polarization.

Just Accepted

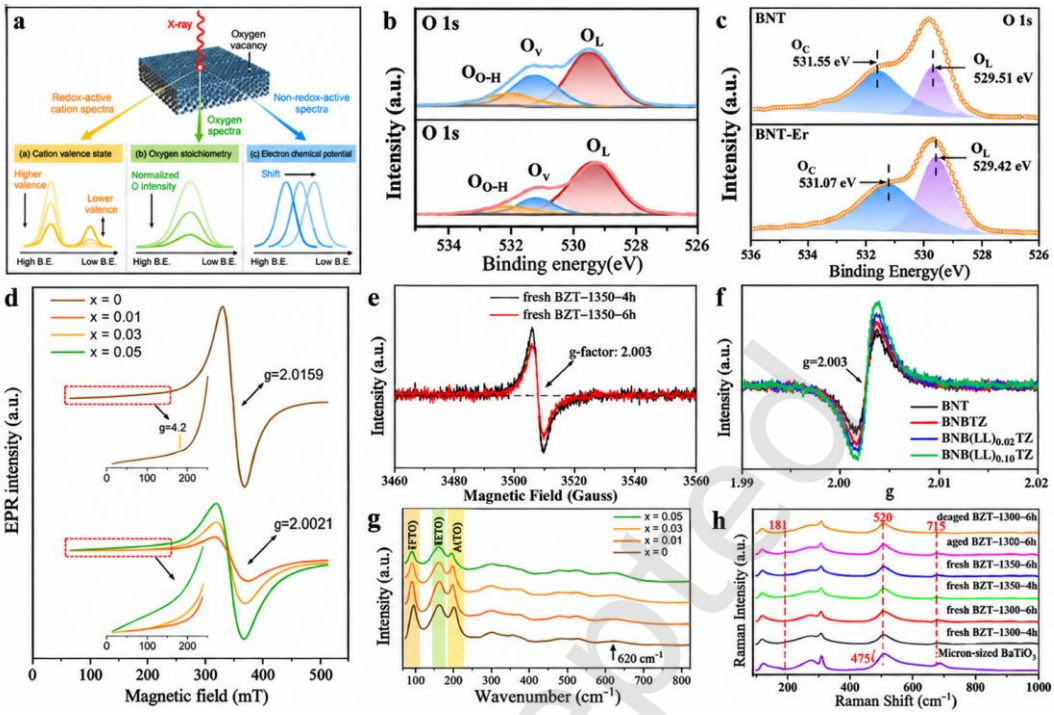


Figure 9 Spectroscopic identification of oxygen-vacancy defects in representative doped piezoelectric and piezocatalytic materials. (a) Schematic illustration of XPS-based oxygen-vacancy analysis. Copyright 2024 the author[135]. (b) Nd-BTZSN and Yb-BTZSN. Copyright 2025, Elsevier[128]. (c) BNT-based systems. Copyright 2024, Elsevier[129]. (d) EPR and (g) Raman spectra of $Bi_{1-x}La_xFeO_3$ nanoparticles. Copyright 2024 the Author(s)[35]. (h) Raman and (e) EPR spectra of BZT particles. Copyright 2023, Elsevier [130]. (f) EPR spectra of BNT-based ceramics. Copyright 2025, Elsevier [131].

3.2.3 Carrier concentration

As a direct consequence of electronic-structure reconstruction, dopant incorporation can significantly regulate carrier concentration by introducing donor or acceptor states, altering defect chemistry, and modifying the position of the Fermi level[51, 67, 69]. In aliovalently doped systems, charge compensation often generates free carriers or defect-related electronic states, whereas isovalent doping can indirectly influence carrier concentration through lattice distortion and defect formation[69]. Consequently, the carrier concentration can be effectively tuned by controlling the dopant species, valence state, and concentration.

Just Accepted

Appropriate carrier regulation provides the basis for optimizing charge transport and piezocatalytic performance[4, 28].

Cui et al. systematically investigated Ca^{2+}-doped $Sr_2Nb_2O_7$ and demonstrated that doping not only introduces lattice distortion but also significantly increases carrier density [136]. As evidenced by Mott-Schottky plots, the carrier concentration of $Ca_{0.8}Sr_{1.2}Nb_2O_7$ reaches 1.59×10^{18} cm^{-3}, approximately 56% higher than that of the undoped sample **(Figure 10a)**. Raman spectra further confirm that Ca doping induces local lattice distortion and structural modulation, which are closely associated with defect formation and carrier generation **(Figure 10b)**. As a result, the electrochemical impedance spectroscopy (EIS) response exhibits a reduced Nyquist arc radius, indicating lower charge-transfer resistance and more efficient interfacial electron migration [98]. This carrier-regulation effect is also observed in layered materials. In palladium metallene (Pd-ene)/MoS_2 composites, the in-situ introduction of conductive Pd metallene markedly enhances interlayer charge transfer. As shown in **Figure 10c**, the EIS Nyquist plots display a pronounced reduction in arc radius after Pd-ene incorporation, while the transient current response shows a substantial increase in current density **(Figure 10d)** [136]. These results indicate that (Pd-ene) improves conductivity, carrier separation, and interfacial charge transport. Similarly, Er^{3+} doping in $BaTiO_3$ significantly modulates carrier concentration through oxygen-vacancy and defect-dipole formation. The piezo-current response reaches its maximum at an optimal Er^{3+} concentration of 1 mol%, indicating efficient charge generation and transport under mechanical excitation **(Figure 10e)**[137]. Carrier concentration can be quantitatively evaluated using methods such as the Hall effect[34],

$$c=1/(e\times\frac{V_H d}{IB}) \quad (2)$$

where B, I, e, and d represent magnetic field, applied current, electronic charge, and sample thickness, respectively. Mott-Schottky analysis is also widely used to estimate carrier density. Overall, rational tuning of carrier concentration provides a crucial pathway for synchronizing bulk electronic transport with surface catalytic processes, ultimately improving piezocatalytic performance[138].

Just Accepted

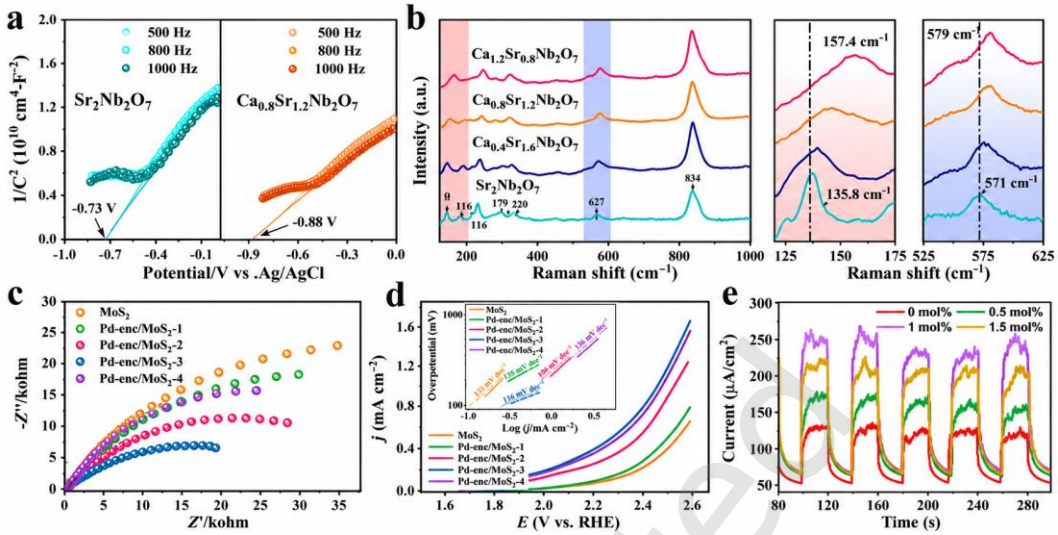


Figure 10 Representative characterization of charge transport and piezoelectric response in doped and interface-modified piezocatalysts. (a) Mott-Schottky plots and (b) Raman spectra of Ca-modified $Sr_2Nb_2O_7$-based materials. Copyright 2025, Elsevier[98]. (c) Electrochemical impedance spectra and (d) transient current responses of MoS_2 and Pd-ene/MoS_2-X piezocatalysts. Copyright 2024, Elsevier[136]. (e) Piezo-current curves of undoped and Er-doped BTO samples. Copyright 2025, Elsevier[137].

3.2.4 Density of states modulation

The electronic density of states (DOS) describes the number of available electronic states at a given energy and provides an important descriptor for understanding doping-induced electronic-structure reconstruction[139]. When dopant atoms are incorporated into a host lattice, the local crystal potential is perturbed, giving rise to orbital rehybridization, impurity-state formation, and redistribution of electronic states, particularly near the Fermi level (E_F). These changes modify the electronic configuration of the host material and determine the availability of electronic states for carrier excitation. The DOS can be expressed as,

$$D(E) = \frac{dN(E)}{dE} \tag{3}$$

where $D(E)$ is the density of electronic states at energy E, and $N(E)$ is the cumulative number of electronic states below E. Consequently, dopant-induced DOS reconstruction provides a direct electronic-structure descriptor for evaluating the influence of doping on piezocatalytic materials.

Just Accepted

Ca-doped $Sr_2Nb_2O_7$ provides a representative example of dopant-induced DOS modulation. As shown in **Figure 11a**, Ca incorporation reconstructs the total DOS and redistributes the orbital contributions near the band edges[98]. This electronic reconstruction originates from the distortion of NbO_6 octahedra induced by Ca substitution, which alters the hybridization between Nb 4d and O 2p orbitals. Similar DOS evolution is observed in oxygen-modified MoS_2. As illustrated in **Figure 11b,c**, oxygen incorporation introduces O 2p states and strengthens their hybridization with Mo d and S p orbitals, resulting in a more continuous DOS distribution near E_F[140]. These results indicate that dopant incorporation can regulate the electronic structure not only through impurity-state formation but also by modifying the interactions among host-lattice orbitals. A comparable DOS reconstruction has also been reported in doped ZnO systems. As shown in **Figure 11d,e**, N doping redistributes both the total and projected DOS around E_F, reflecting enhanced electronic coupling among dopant states, ZnO host orbitals, and adsorbed species[141]. In Mn-doped ZnO, additional electronic states associated with Mn 3d orbitals and oxygen vacancies emerge near the Fermi level (**Figure 11f**), further modifying the DOS distribution[38]. These observations demonstrate that impurity states, orbital hybridization, and defect-related electronic states collectively contribute to DOS reconstruction in doped piezocatalysts.

The influence of DOS modulation on carrier excitation can be understood from semiconductor statistics. The carrier concentration is determined by the product of the density of available electronic states and their occupation probability,

$$n = \int_{E_c}^{\infty} D_c(E) f(E) dE \quad (4)$$

where $Dc(E)$ represents the conduction-band density of states, $f(E)$ is the Fermi-Dirac distribution function, and E_c is the conduction-band minimum. Consequently, changes in the DOS near the Fermi level directly affect the number of carriers that can be thermally excited. These studies demonstrate that dopant incorporation reconstructs the density of states through orbital hybridization, impurity-state formation, and defect-induced electronic redistribution, providing the electronic basis for subsequent carrier regulation and piezocatalytic enhancement.

Just Accepted

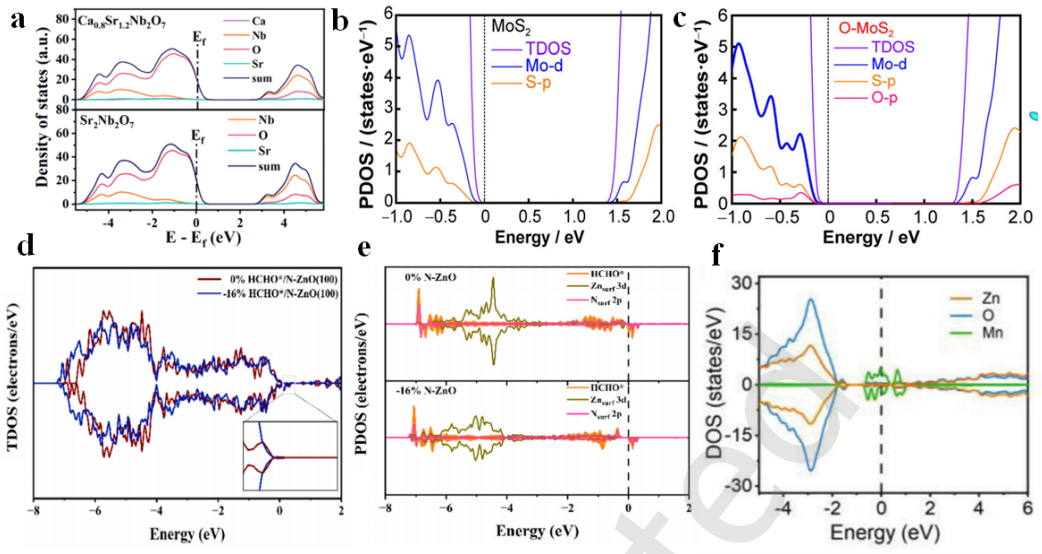


Figure 11 Density of states (DOS) modulation in representative doped piezocatalytic materials. (a) Pristine and Ca-doped $Sr_2Nb_2O_7$. Copyright 2025 Elsevier [98]. (b) MoS_2 and (c) O-MoS_2. Copyright 2023 Springer Nature [140]. (d) Total density of states (TDOS) and (e) Partial density of states (PDOS) of HCHO adsorbed on N-doped ZnO. Copyright 2025 Elsevier [141]. (f) Mn-doped ZnO with oxygen vacancies. Copyright 2023 Wiley [38].

3.2.5. Experimental verification of dopant incorporation and defect distribution

Reliable verification of dopant incorporation, crystallographic site occupancy, oxidation state, and spatial distribution remains a critical challenge in doping-engineered piezocatalysts. Although doping-induced changes in lattice parameters, electronic structures, defect concentrations, and piezoelectric responses are frequently reported, these macroscopic or ensemble-averaged observations do not necessarily establish the actual atomic configuration of the dopants. For example, a shift in XRD peaks may arise from lattice strain, crystallite-size effects, residual stress, or compositional changes, whereas variations in XPS spectra may reflect changes in surface chemistry rather than bulk substitution. Therefore, establishing reliable doping, structure, property relationships require complementary characterization techniques that probe different length scales and chemical environments.

XRD combined with Rietveld refinement is a useful starting point for evaluating phase purity, lattice parameters, average crystallographic structure, and candidate dopant-site

Just Accepted

occupancies. By refining the experimental diffraction patterns against structural models, this approach can identify systematic structural changes and detect sufficiently abundant crystalline secondary phases. **Figure 12g** illustrates Rietveld refinement of XRD patterns for $Bi_{1-x}La_xFeO_3$ nanoparticles with different La contents, including the observed patterns, calculated profiles, difference curves, and Bragg reflection positions [35]. However, the absence of detectable secondary phases does not by itself prove that all dopants occupy the intended lattice sites. In particular, the reliability of occupancy refinement may be limited by low dopant concentrations, weak scattering contrast between host and dopant atoms, parameter correlations, and instrumental resolution. Accordingly, refined occupancies should be interpreted together with compositional analysis and element-specific local-structure measurements.

X-ray absorption spectroscopy (XAS), including X-ray absorption near-edge structure (XANES) and extended X-ray absorption fine structure (EXAFS), provides complementary information on the oxidation state and local coordination environment of selected elements. As illustrated in **Figure 12c, d**, XANES spectra and EXAFS analyses can reveal changes in the absorption-edge region, local chemical environment, and neighboring-atom distances, respectively [142]. Comparison with appropriate reference compounds and structural models can help evaluate whether a dopant adopts the expected valence state and local coordination. Nevertheless, XAS generally provides an ensemble-averaged signal and requires careful spectral interpretation and model-dependent fitting; it may not independently distinguish multiple spatially separated dopant populations with similar local environments.

Atomic-resolution scanning transmission electron microscopy combined with energy-dispersive X-ray spectroscopy or electron energy-loss spectroscopy (STEM-EDS/EELS) can further investigate dopant distributions at the nanoscale and, when spatial resolution and signal quality are sufficient, at the atomic-column level. **Figure 12a, b** illustrates atomic-resolution imaging, elemental mapping, and an EELS line scan used to examine spatially resolved compositional and spectroscopic variations in complex oxides [143]. These methods can help identify dopant segregation, compositional inhomogeneity, and local changes in electronic structure or coordination. However, interpretation must account for specimen thickness, projection effects, signal-to-noise ratio, spectral overlap,

Just Accepted

quantification uncertainty, and possible electron-beam-induced damage. Consequently, apparent atomic-scale contrast or elemental enrichment should not be regarded as definitive evidence of substitutional occupancy without corroborating structural or spectroscopic information.

XPS is valuable for examining the chemical states of dopants and host elements, particularly near the material surface. When combined with depth profiling, it can provide information on the variation of chemical composition and chemical states with depth, thereby helping distinguish surface enrichment from more uniform dopant distributions. Nevertheless, conventional XPS is surface-sensitive, and ion sputtering during depth profiling may preferentially remove elements, modify oxidation states, or generate defects. XPS depth profiles should therefore be interpreted cautiously and, where possible, cross-validated using bulk-sensitive elemental analysis and complementary structural characterization. In addition, inductively coupled plasma mass spectrometry (ICP-MS) or related bulk elemental techniques can quantify the actual dopant content, but they cannot independently establish the dopant's crystallographic site or atomic-scale distribution.

Positron annihilation spectroscopy (PAS) offers another complementary approach for investigating vacancy-type defects and open-volume defects. As illustrated in **Figure 12e, f**, Doppler-broadening spectra and the S parameter as a function of positron implantation energy can provide information about electron-momentum distributions, positron trapping, and depth-dependent defect variations [144]. Because positrons can be preferentially trapped at certain open-volume defects, PAS is particularly useful for assessing vacancy-related changes that may not be readily resolved by conventional diffraction methods. However, the S parameter is not a unique fingerprint of a particular vacancy species, and its value can depend on defect concentration, defect configuration, chemical environment, and positron-trapping behavior. PAS should therefore be combined with techniques such as XPS, EPR, XAS, or first-principles calculations when assigning specific defect structures or charge states.

Overall, no single characterization technique is sufficient to establish all aspects of dopant incorporation and defect chemistry. A robust verification strategy should integrate bulk compositional analysis, average crystallographic refinement, element-specific spectroscopy, atomic-scale spatial characterization, and defect-sensitive measurements.

Just Accepted

Whenever feasible, experimental characterization should be conducted using undoped controls, suitable reference materials, and samples synthesized under consistent conditions. Regardless of the synthesis routes is essential for distinguishing genuine lattice incorporation from surface enrichment, grain-boundary segregation, secondary-phase formation, and dopant-induced defect compensation. Establishing this evidence chain provides a more reliable foundation for correlating dopant configuration with lattice distortion, charge-carrier behavior, piezoelectric polarization, and the resulting piezocatalytic performance. Nevertheless, theoretical reaction-energy profiles alone do not establish the experimentally rate-determining step under dynamic mechanical excitation; corroborating kinetic measurements and operando characterization are required to distinguish thermodynamic preferences from kinetic limitations.

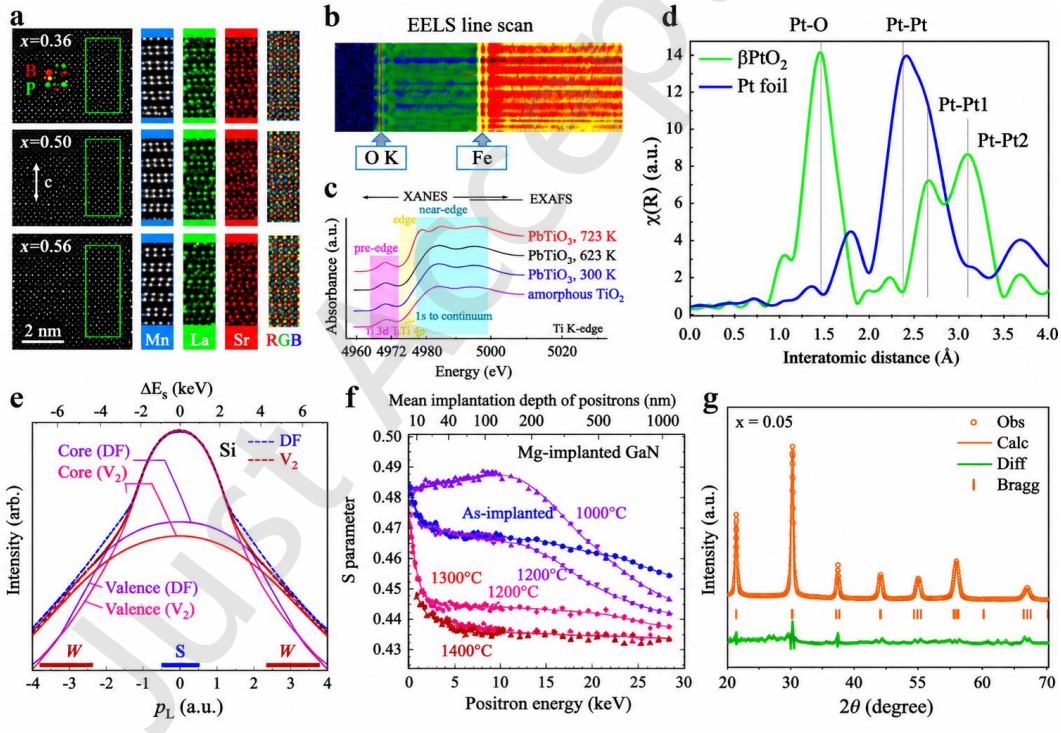


Figure 12 Complementary characterization techniques for verifying dopant incorporation, local chemical environments, and vacancy-type defects in functional oxides. (a) Atomic-resolution HAADF-STEM images and elemental maps illustrating spatially resolved compositional analysis. (b) An EELS line scan illustrating spatially resolved spectroscopic analysis of complex oxides. Copyright 2017 Elsevier[143]. (c) Ti K-edge XANES spectra of $PbTiO_3$ under different conditions, illustrating changes in the

Just Accepted

element-specific X-ray absorption near-edge structure. (d) Pt L_3-edge XAS/EXAFS analysis, including Fourier-transformed radial distribution profiles. Copyright 2021 the Author(s)[142]. (e) Simulated positron-annihilation Doppler-broadening spectra for defect-free Si and Si containing a divacancy, with the corresponding S and W integration regions. (f) S parameter as a function of positron implantation energy for as-implanted and annealed Mg-implanted GaN, illustrating the use of PAS to investigate depth-dependent vacancy-type defects. Copyright 2025 the Author(s) [144]. (g) Rietveld refinement of XRD patterns of $Bi_{1-x}La_xFeO_3$ nanoparticles with $x = 0.05$. Copyright 2024 the Author(s)[35].

3.3 Piezoelectric properties

3.3.1 Polarization regulation

Building upon the structural and electronic mechanisms discussed in Sections 3.1 and 3.2, this section focuses on how doping regulates intrinsic, interfacial, and spin-dependent polarization in piezoelectric materials[51, 69]. These polarization mechanisms determine the magnitude, distribution, and dynamic response of the internal electric field generated under mechanical stimulation. Their effects on piezocatalysis depend on the resulting electromechanical response and its coupling with carrier transport and interfacial reactions[145-148].

Intrinsic polarization enhancement represents one of the most direct approaches for strengthening piezoelectric polarization through doping. As shown in **Figure 13a**, Fe^{3+} substitution at the B site of hexagonal $YMnO_3$ significantly enlarges the polarization-electric field (*P*-*E*) hysteresis loop, increasing the spontaneous polarization from 0.41 to 8.84 μC cm^{-2}[111]. This enhancement originates from dopant-induced local structural distortion and chemical-bond reconstruction, which promote asymmetric atomic displacement, increase dipole density, and stabilize long-range ferroelectric ordering. Consequently, the enhanced intrinsic polarization generates a stronger piezoelectric potential under mechanical excitation, facilitating efficient charge separation.

Beyond modifying bulk polarization, doping combined with heterostructure construction can further enhance polarization through interfacial charge redistribution. As illustrated in **Figure 13b**, iodine doping in $Bi_4Ti_3O_{12}$ improves the bulk polarization, while

Just Accepted

the incorporation of two-dimensional transition-metal carbides, nitrides, and carbonitrides (MXene) establishes a strongly coupled heterointerface[149]. The difference in electronic structures between $Bi_4Ti_3O_{12}$ and MXene induces interfacial charge transfer and local electric-field redistribution, generating additional interfacial polarization. The coupling between bulk polarization and interface-induced polarization strengthens the internal electric field, accelerates carrier extraction, and improves piezocatalytic activity[150].

In addition to conventional polarization regulation, doping can introduce spin-polarized electronic states to provide an alternative pathway for improving charge separation. As shown in **Figure 13c, d**, Fe doping in Bi_3TiNbO_9 induces spin-polarized states that suppress electron-hole recombination through spin-selection effects [35]. In pristine Bi_3TiNbO_9, randomly oriented spin states facilitate carrier recombination during ultrasonic excitation[151]. In contrast, Fe incorporation generates spin-dependent electronic configurations that increase the energy barrier for spin flipping, prolong carrier lifetime, and enhance charge separation efficiency. Meanwhile, the spin-polarized carriers coupled with the strengthened polarization field exhibit improved directional migration behavior, simultaneously optimizing charge-transfer kinetics and reaction efficiency.

Doping-induced polarization enhancement arises from the synergistic regulation of crystal distortion, electronic redistribution, and defect-mediated structural evolution. These modifications collectively strengthen the internal electric field, promote directional carrier migration, and accelerate surface redox reactions. However, enhanced polarization alone does not necessarily translate into superior piezocatalytic performance, as excessive polarization may induce charge screening, while insufficient carrier mobility, unfavorable defect states, or sluggish surface kinetics can limit catalytic efficiency. Therefore, polarization regulation should be integrated with electronic-structure optimization, defect engineering, and interfacial reaction control to achieve a balanced enhancement of piezocatalytic performance.

Just Accepted

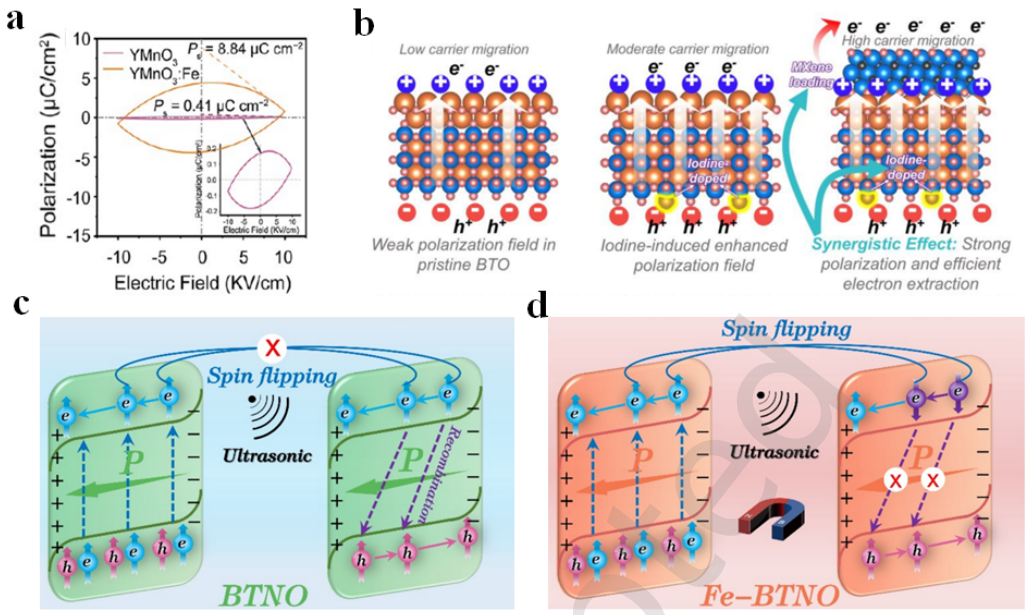


Figure 13 Polarization regulation and spin-polarization-assisted charge separation in representative doped piezocatalysts. (a) Polarization-electric field hysteresis loops of $YMnO_3$ and Fe-doped $YMnO_3$. Copyright 2025 American Chemical Society[111] (b) Material design strategy for MBTO-I. Copyright 2026 the Author(s)[149]. Spin-polarization-assisted charge separation in (c) BTNO and (d) Fe-BTNO. Copyright 2025 Elsevier [152].

3.3.2 Piezoelectric response enhancement

Besides regulating polarization behavior, doping can directly enhance the piezoelectric coefficient by modifying lattice distortion, local symmetry, domain-switching behavior, and electromechanical coupling. As summarized in **Figure 14**, representative doped piezoelectric materials consistently exhibit enhanced piezoelectric responses after appropriate dopant incorporation. An appropriate doping concentration is essential for maximizing the piezoelectric coefficient. As shown in **Figure 14a**, the d_{33} value of Sm-doped PZT films reaches a maximum of approximately 280 pm V^{-1} at 1.5 mol% Sm, after which it gradually decreases with further doping[[71]. This behavior indicates that moderate lattice distortion optimizes electromechanical coupling, whereas excessive dopant incorporation introduces structural disorder that deteriorates the piezoelectric response. Similar concentration-dependent behavior has also been reported for Al-doped

Just Accepted

BCZT ceramics, where an optimized doping level maximizes the piezoelectric coefficient by balancing lattice distortion and structural stability[34]. The enhancement of the piezoelectric coefficient is further verified by piezoresponse force microscopy (PFM). Compared with pristine materials, Mn-doped NiFe-LDH and $Cu_{1.0}$-BTO@Gua exhibit significantly enlarged amplitude-voltage (butterfly) hysteresis loops **(Figure 14b-e**), indicating enhanced local piezoresponse, improved domain-switching behavior, and stronger electromechanical coupling[153-155]. In addition, the PFM-measured d_{33} response of Cu@SnS_2-*x* remains consistently higher than that of pristine SnS_2 throughout the applied driving-voltage range (**Figure 14f**), further confirming that Cu doping effectively strengthens the intrinsic piezoelectric response[154].

The improvement of the piezoelectric coefficient is closely associated with dopant-induced structural evolution and the balance between lattice distortion and structural stability. Appropriate dopant incorporation optimizes local strain distribution and electromechanical coupling, enabling stronger piezoelectric polarization under mechanical excitation. However, excessive doping may introduce structural disorder, secondary phases, and charge-screening effects, which disrupt long-range polarization ordering and reduce the piezoelectric response. Therefore, enhancing piezoelectric coefficients requires precise regulation of dopant concentration, defect chemistry, and lattice stability rather than simply increasing dopant content. Such mechanism-guided optimization is essential for maintaining efficient polarization generation and promoting piezoelectric-driven charge separation in piezocatalytic systems. In addition, the critical role of piezoelectric properties of a material in determining its piezocatalytic performance is well established. Previous experimental studies have demonstrated a strong positive correlation between piezoelectric response and piezocatalytic activity within compositionally controlled material systems [28, 156-158].

Just Accepted

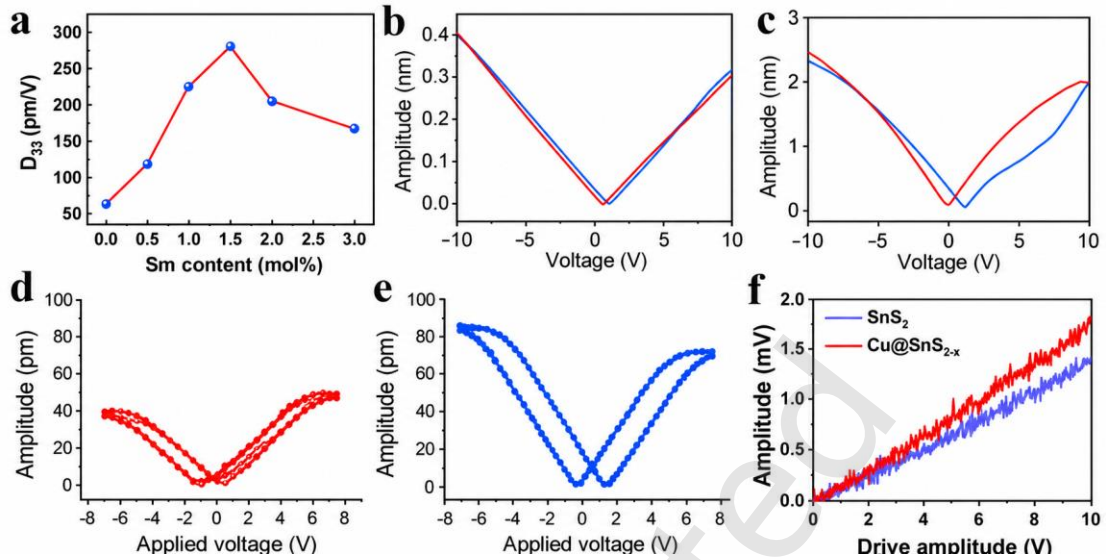


Figure 14 Doping-induced enhancement of piezoelectric properties in representative piezoelectric materials. (a) Dependence of the piezoelectric coefficient (d_{33}) of Sm-doped PZT films on Sm concentration. Copyright 2024 the Author(s)[71]. PFM amplitude-voltage (butterfly) hysteresis loops of (b) pristine NiFe-LDH and (c) Mn-doped NiFe-LDH. Copyright 2024 Wiley[155] and (d) pristine $BaTiO_3$ and (e) $Cu_{1.0}$-BTO@Gua. Copyright 2024 the Author(s)[153].(f) PFM-measured d_{33} responses of pristine SnS_2 and Cu@SnS_2-x as a function of the driving amplitude, demonstrating the enhanced piezoelectric response induced by Cu doping. Copyright 2024 American Chemical Society[154].

3.4 Potential negative effects

Although doping is an effective strategy for enhancing piezocatalytic performance, its beneficial effects and optimal concentration depend on the interplay among dopant solubility, lattice-site occupancy, lattice distortion, defect chemistry, carrier density, phase stability, and polarization response. At relatively low concentrations, dopant incorporation can introduce beneficial lattice distortion and appropriately regulate defect populations, thereby facilitating polarization-assisted charge separation and interfacial charge transfer. When the dopant concentration exceeds the optimal level or the lattice solubility limit, excessive doping may induce structural instability, unfavorable defect evolution, phase transformation, and deterioration of piezoelectric properties, ultimately reducing the piezocatalytic performance[27, 159, 160].

Just Accepted

One of the most common adverse effects of excessive doping is the deterioration of the crystal structure. Excessive dopant incorporation can induce severe lattice distortion, internal stress accumulation, dopant segregation, and secondary-phase formation, thereby disrupting the long-range crystallographic order of the host material. In ferroelectric and piezoelectric oxides, excessive dopant incorporation may also alter phase stability. For example, increasing Fe^{3+} doping in $BaTiO_3$ promotes the formation of the hexagonal phase at the expense of the ferroelectric tetragonal phase, accompanied by a significant reduction in remanent polarization[161]. Excessive doping can also induce unfavorable defect evolution. In piezoelectric oxides, aliovalent doping is frequently accompanied by the formation of charge-compensating oxygen vacancies. While a moderate concentration of oxygen vacancies can facilitate charge transport and surface activation, excessive vacancies may introduce deep-level defect states, increase leakage conductivity, screen the piezoelectric field, and act as recombination centers for piezo-induced charge carriers. In addition, oxygen vacancies may migrate toward ferroelectric domain walls and pin their motion, leading to polarization aging, fatigue, and reduced electromechanical response in $BaTiO_3$ and $PbTiO_3$-based materials [162]. Meanwhile, excessive defect concentrations can increase leakage conductivity and carrier recombination, while the associated charge accumulation may screen the piezoelectric polarization field. These effects can collectively weaken the effective polarization response and offset the benefits of increased carrier concentration. With further doping, however, the solubility limit may be approached or exceeded, promoting dopant segregation and secondary-phase formation. Li-added $BaTiO_3$ exhibits variations in piezocatalytic activity with the amount of LiCl introduced[163]. In Co-doped $BiFeO_3$, the degradation efficiency reaches a maximum at 5 mol% Co, whereas further doping promotes secondary-phase formation and reduces catalytic performance [164]. Similarly, Sb-doped ZnO thin films exhibit the highest piezocatalytic efficiency at 1 at.% Sb under ultrasonic excitation, while higher Sb concentrations do not provide further improvement[165]. The long-term stability of doped piezocatalysts under repeated mechanical stimulation also deserves attention. Continuous ultrasonic vibration or cyclic loading may induce dopant migration, defect redistribution, surface reconstruction, or dopant leaching, particularly in nanomaterials with abundant surface defects and high

Just Accepted

surface energy. These structural changes can alter the distribution of active sites, weaken the internal piezoelectric field, and gradually reduce catalytic durability[160, 166].

Overall, the adverse effects of excessive doping arise from the coupled deterioration of crystal structure, defect chemistry, polarization behavior, and electromechanical stability. Future doping strategies should therefore focus on optimizing dopant concentration and lattice occupation, controlling defect populations, and maintaining phase stability to achieve effective polarization-assisted charge separation while preserving long-term piezoelectric and piezocatalytic performance.

3.5 Doping-regulated catalytic pathways and rate-determining steps

Doping engineering influences piezocatalysis not only by modifying crystal structures, defect chemistry, carrier behavior, and piezoelectric polarization, but also by regulating the elementary steps of surface catalytic reactions. Under mechanical stimulation, the piezoelectric polarization field promotes directional carrier separation and migration, while dopant-induced electronic states and defects can modify reactant adsorption, interfacial charge transfer, and the activation of chemical bonds. Consequently, the overall catalytic process involves several coupled stages: reactant adsorption, polarization-driven charge separation, interfacial electron or hole transfer, intermediate formation, and product desorption. The relative importance of these stages depends on the catalyst composition, surface structure, reaction environment, and applied mechanical stimulus.

For environmental remediation, doping can regulate oxygen adsorption and activation, thereby influencing the formation and conversion of reactive oxygen species (ROS). Under mechanical stimulation, electrons can reduce dissolved oxygen to superoxide radicals ($\bullet O_2^-$), which may subsequently participate in H_2O_2 formation and further ROS conversion, whereas holes can oxidize adsorbed water or hydroxyl species to generate •OH radicals. These species contribute to pollutant degradation through radical and non-radical pathways [141, 167]. Dopant-induced changes in defect states, surface adsorption properties, and interfacial charge-transfer kinetics can therefore influence not only the overall degradation rate but also the relative contributions of different oxidation pathways. A representative theoretical study further illustrates how piezoelectric polarization regulates the adsorption and oxidation pathways of reactants. Zhao et al. investigated the catalytic oxidation of

Just Accepted

formaldehyde (HCHO) on ZnO(100) surfaces under different strain conditions. DFT calculations revealed that compressive strain of 12% substantially enhanced the adsorption of HCHO and O_2, with their adsorption free energies changing from -0.37 to -1.49 eV and from 0.37 to -0.57 eV, respectively (**Figure 16 c, d**) [168]. The reaction proceeds through a Langmuir–Hinshelwood mechanism involving the formation of *CHO, *OOH, *O, and *OH intermediates, ultimately yielding CO_2 and H_2O. Notably, the energy barrier for O-O bond cleavage in the OOH intermediate decreases from 1.29 to 0.14 eV under compressive strain. Meanwhile, the rate-determining step shifts to the subsequent dehydrogenation of HCO_2, with a barrier of 0.79 eV, indicating that piezoelectric polarization can substantially alter both reaction kinetics and the rate-determining step [168]. For energy-conversion reactions, such as hydrogen evolution and H_2O_2 production, doping may modify the adsorption and activation of reaction intermediates and facilitate multistep electron-transfer processes[169, 170]. The influence of chemical modification on intermediate adsorption has also been demonstrated in piezocatalytic hydrogen evolution. Fluorinated-ligand functionalization of UiO-66 reduced the Gibbs free energy of hydrogen adsorption (ΔG_H^*) from 0.21 to 0.13 eV (**Figure 15 a, b**) [171], indicating a more favorable adsorption–desorption balance for hydrogen intermediates. The optimized H* adsorption configuration further provides atomic-scale evidence for the modified surface reaction behavior. This modification, together with the enhanced piezoelectric response and regulated electronic structure, facilitates hydrogen desorption and promotes interfacial H_2 evolution [171]. Thus, the catalytic consequences of doping extend beyond enhanced charge separation to the regulation of reaction pathways and intermediate formation.

Importantly, the rate-determining step cannot be universally assigned to a single elementary process across different piezocatalytic systems. Depending on the catalyst and target reaction, the rate-limiting process may involve reactant adsorption, interfacial charge transfer, chemical-bond activation, intermediate conversion, or product desorption. Density functional theory (DFT) calculations can provide insights into adsorption configurations, reaction energetics, and competing pathways, whereas reactive-species trapping, electron paramagnetic resonance, kinetic measurements, and in situ or operando spectroscopy offer complementary experimental evidence. Their combined application is

Just Accepted

essential for identifying how doping modifies specific reaction steps and for distinguishing improvements in charge utilization from changes in intrinsic surface reaction kinetics.

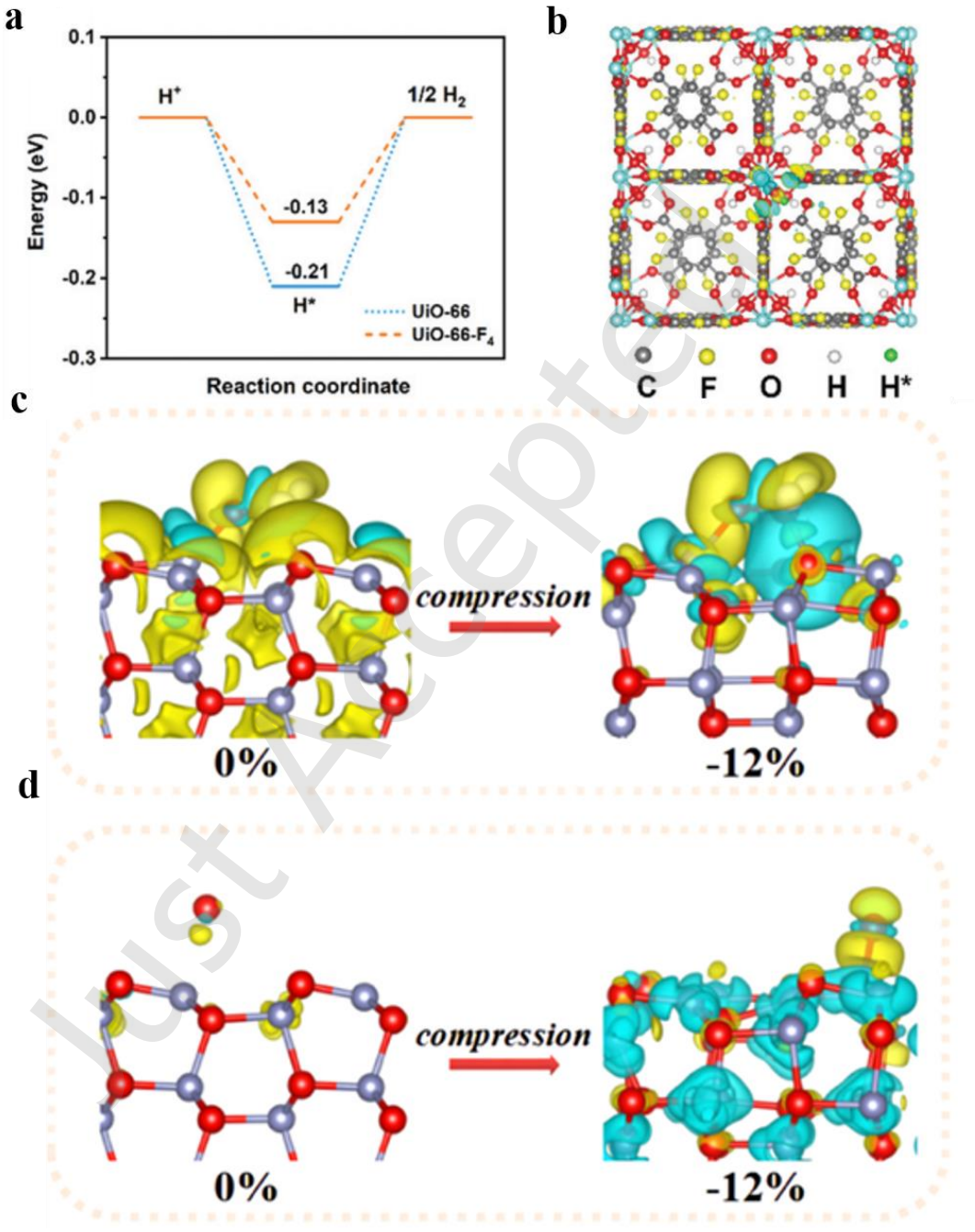


Figure 15 (a) Gibbs free-energy diagram and (b) optimized H adsorption configuration of UiO-66 and UiO-66-F_4. Copyright 2022 The Royal Society of Chemistry[171]. (c) Charge-density distributions of ZnO under unstrained and (d) compressive conditions, illustrating strain-induced charge redistribution. Copyright 2024 Elsevier [168].

Just Accepted

4. Doping in piezocatalytic applications

The preceding sections establish how doping regulates crystal structures, defect chemistry, electronic states, and piezoelectric polarization. These modifications collectively influence the generation and separation of charge carriers, reactant adsorption, interfacial charge transfer, and the energetics of surface reactions. Their catalytic consequences, however, depend on the specific reaction system and operating conditions. Accordingly, this section examines how doping-induced structural and electronic changes translate into enhanced catalytic performance in environmental remediation, energy conversion, and biomedical applications, with attention to reaction pathways, reactive intermediates, and catalytic kinetics.

4.1 Environmental remediation

Piezocatalysis has attracted extensive attention in environmental remediation because mechanically induced polarization charges can drive surface redox reactions for organic pollutant degradation[52, 172-174], toxic-ion reduction[145, 175-178], and microbial inactivation[179-183]. Compared with pristine piezocatalysts, doping engineering provides an effective strategy to simultaneously regulate defect chemistry, electronic structure, polarization intensity, interfacial charge transfer, and surface adsorption behavior, thereby enhancing both catalytic efficiency and reaction selectivity[184].

Organic pollutant degradation is currently the most extensively investigated application of doped piezocatalysts. Dopant-induced defect engineering introduces localized electronic states that facilitate charge separation while simultaneously promoting oxygen activation, leading to enhanced generation of ROS, including $\bullet O_2^-$, •OH, $^1O_2$, and H_2O_2. Under mechanical stimulation, piezoelectric polarization drives electron–hole separation. Electrons activate dissolved oxygen to generate superoxide radicals, which can further transform into hydrogen peroxide and hydroxyl radicals, while holes oxidize water or hydroxyl groups to produce hydroxyl radicals[185, 186],

$$e^- + O_2 \rightarrow \bullet O_2^- \quad (5)$$

$$2\bullet O_2^- + 2H^+ \rightarrow H_2O_2 + O_2 \quad (6)$$

$$H_2O_2 + e^- \rightarrow \bullet OH + OH^- \quad (7)$$

Just Accepted

The relative contributions of these pathways depend on the adsorption and activation of dissolved oxygen, the availability of surface reaction sites, and the kinetics of intermediate conversion. Dopant-induced changes in defect states and interfacial electronic structures may alter these processes. The resulting ROS subsequently participate in pollutant oxidation through both radical and non-radical pathways. As summarized in **Figure 16**, representative doped piezocatalysts exhibit enhanced organic pollutant degradation through synergistic regulation of charge transport, defect structures, and surface redox reactions. For example, Zn/N co-doped porous carbon and oxygen-doped MoS_2 demonstrate that optimized coordination environments and vacancy structures enhance ROS generation and accelerate pollutant degradation through improved carrier behavior and interfacial reaction kinetics (**Figure 16a, b**)[43, 140]. Transition-metal dopants further improve catalytic efficiency by introducing effective carrier-trapping centers and promoting interfacial electron transfer. Representative systems, including Cu-doped Bi_2WO_6 and other metal-doped piezocatalysts, couple piezoelectric polarization with oxidant activation processes, enabling efficient pollutant removal through both radical and non-radical oxidation pathways (**Figure 16c, d**)[167, 187, 188]. Moreover, rare-earth dopants such as Ce regulate local electronic configurations and oxygen-vacancy formation, thereby enhancing charge migration and surface redox activity under mechanical stimulation (**Figure 16e, f**)[189]. Beyond organic pollutant degradation, toxic-ion reduction represents another important pathway for environmental piezocatalysis. Under mechanical stimulation, piezoelectric polarization promotes charge separation, and the resulting electrons can directly participate in the reduction of high-valence metal ions. $BaTiO_3$-based piezocatalysts and $BaCO_3$@$BaTiO_3$ microspheres have demonstrated effective piezocatalytic reduction of Cr(VI), confirming the feasibility of utilizing mechanically generated electrons for toxic-ion conversion [145, 175]. Within the framework of doping engineering, regulation of defect states, carrier concentration, band-edge positions, and interfacial electron-transfer kinetics provides a potential route for improving electron utilization and reduction efficiency. Compared with organic pollutant degradation, however, systematic studies focusing specifically on doped piezocatalysts for toxic-ion reduction remain relatively limited. Further investigations are therefore required

Just Accepted

to establish quantitative relationships among dopant configuration, defect chemistry, interfacial electron transfer, reduction selectivity, and long-term stability.

Rational doping engineering enhances environmental piezocatalysis by regulating ROS generation, charge transport, and interfacial reaction kinetics, enabling efficient organic pollutant degradation, toxic-ion reduction, and microbial inactivation. However, practical applications remain limited by catalyst stability, dopant migration, defect evolution, and complex wastewater environments. Future studies should establish quantitative relationships among dopant chemistry, defect dynamics, polarization behavior, ROS selectivity, and long-term durability, thereby promoting mechanism-guided design of robust piezocatalysts for scalable environmental remediation.

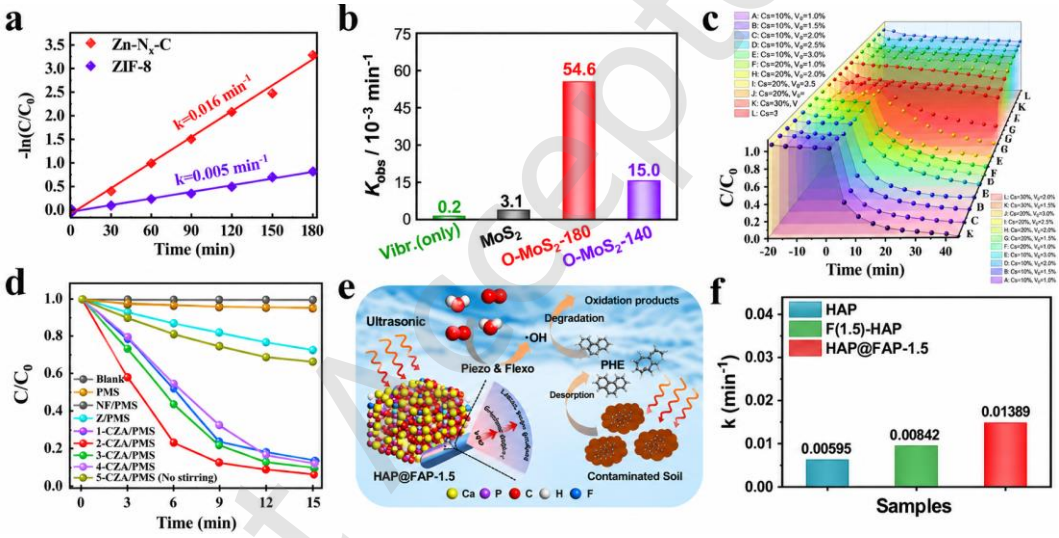


Figure 16 Piezocatalytic degradation performance and mechanisms of representative doped catalysts. (a) Zn-N_x-C and ZIF-8. Copyright 2023 Elsevier[190]. (b) O-MoS_2-based piezocatalytic degradation. Copyright 2023 Springer[140]. (c) Cu-Bi_2WO_6-assisted pollutant degradation. Copyright 2025. Elsevier[188]. (d) PMS-assisted NOR degradation over doped piezocatalysts. Copyright 2023 Elsevier[167]. (e) Degradation mechanism and (f) catalytic activity of HAP-based catalysts. Copyright 2024 the Author(s)[191].

4.2 Energy conversion

Beyond pollutant degradation, doped piezocatalysts have demonstrated remarkable potential in mechanical-energy-driven energy conversion and resource recovery, including U(VI) reduction, H_2O_2 production[170, 192, 193], H_2 evolution[140, 194, 195], and NO^{3-}

Just Accepted

to NH^{4+} conversion[51, 196-198]. Compared with environmental remediation, these reactions generally involve multi-electron transfer processes and therefore impose more stringent requirements on charge separation efficiency, redox potential matching, surface reaction selectivity, and adsorption energetics. Consequently, doping engineering has become an indispensable strategy for simultaneously regulating polarization intensity, electronic structure, carrier behavior, surface active sites, and reaction thermodynamics[199].

Among various resource-recovery reactions, U(VI) reduction has attracted considerable attention because it converts soluble U(VI) into insoluble U(IV), enabling simultaneous uranium recovery and environmental protection. As shown in **Figure 17a,** pristine BFO exhibited only 32.7% U(VI) removal, whereas Sm/Mn co-doped BSFMO-2 achieved a removal efficiency of 94.8% within 120 min [200]. Notably, the apparent U(VI) reduction rate constant of BSFMO-2 was 8.28 times that of pristine $BiFeO_3$ under the same reported conditions, demonstrating that co-doping substantially accelerates the reduction kinetics[201]. This enhancement is associated with improved piezoelectric polarization, more effective charge-carrier separation, and accelerated interfacial electron transfer. The reaction kinetics followed a pseudo-first-order model[35],

$$\ln(C_0/C) = kt \quad (8)$$

where C_0 and C represent the initial and remaining U(VI) concentrations, respectively, k is the apparent reaction rate constant, and t is the reaction time. These results indicate that appropriate Sm/Mn co-doping enhances electron utilization during U(VI) reduction. Nevertheless, excessive dopant concentrations may introduce structural disorder or additional charge-recombination centers, highlighting the importance of optimizing dopant species and concentration for efficient radioactive-metal recovery[201].

Water-related energy conversion provides further quantitative evidence of the benefits of doping engineering. For V-doped $NaNbO_3$ nanocubes containing 10 mol% V, the reported H_2 and H_2O_2 production rates reached 346.2 and 102.6 μmol g^{-1} h^{-1}, respectively, corresponding to 4.6-fold and 2.2-fold increases over pristine $NaNbO_3$ (**Figure 17b, c**)[140, 170]. These improvements were attributed to enhanced piezoelectric response, increased availability of catalytic active sites, and a reduced energy barriers for water dissociation. In another representative system, oxygen incorporation into MoS_2 significantly enhanced

Just Accepted

piezocatalytic H_2 production (**Figure 17d, e)**. The O-MoS_2-180 sample exhibited the highest H_2 generation rate of 45.1 μmol·g^{-1}·h^{-1}, substantially exceeding those of pristine MoS_2 (17.3 μmol·g^{-1}·h^{-1}) and vibration-only controls (0.4 μmol·g^{-1}·h^{-1}). These results demonstrate that oxygen incorporation effectively improves the catalytic activity of MoS_2 under mechanical stimulation[140]. Beyond water-related energy conversion, doping-engineered piezocatalysts have also demonstrated considerable potential for CO_2 reduction. For example, Nb-doped Pb (Zr,Ti)O_3 (PZTN), with an optimized Nb concentration of 2 mol%, achieves a CO production rate of 789 μmol g^{-1} h^{-1} under pulsed ultrasonic excitation, with a CO/H_2 product ratio exceeding 7.6, indicating favorable selectivity toward CO formation[23]. The bulk ceramic exhibits a piezoelectric coefficient (d_{33}) of approximately 69 pC N^{-1}, suggesting that Nb-induced regulation of piezoelectric polarization may contribute to enhanced charge separation and CO_2 reduction. Notably, the catalytic performance also depends on catalyst dosage (**Figure 17f**). As the PZTN loading increases from 0 to 0.1 g L^{-1}, the CO production rate rises from approximately 3.1 to 4.0 μmol h^{-1}, remains nearly constant at 0.1-0.7 g L^{-1}, and subsequently decreases to approximately 3.7 μmol h^{-1} at 1.0 g L^{-1}. In comparison, the Al_2O_3 reference exhibits a more gradual increase, reaching approximately 3.45 μmol h^{-1} at 1.0 g L^{-1}. These results highlight the importance of optimizing both dopant concentration and catalyst loading to improve mechanically driven CO_2 reduction, demonstrating the potential of doping engineering for CO_2 resource utilization and chemical fuel production [23].

In parallel, piezocatalysis has also been extended to nitrogen-resource recovery. For example, a ZnO nanorod/Shewanella oneidensis metal-reducing strain 1 (MR-1) biohybrid system achieved NO_3^--to-NH_4^+ conversion under hydrodynamic stimulation[196]. In this system, piezoelectrically generated electrons are transferred through bacterial extracellular electron-transfer pathways to drive dissimilatory nitrate reduction, providing an alternative approach for coupling mechanical energy harvesting with nitrogen recovery. A comparison of representative doping-engineered piezocatalysts across environmental remediation, energy conversion, and biomedical applications is summarized in **Table 2**.

Just Accepted

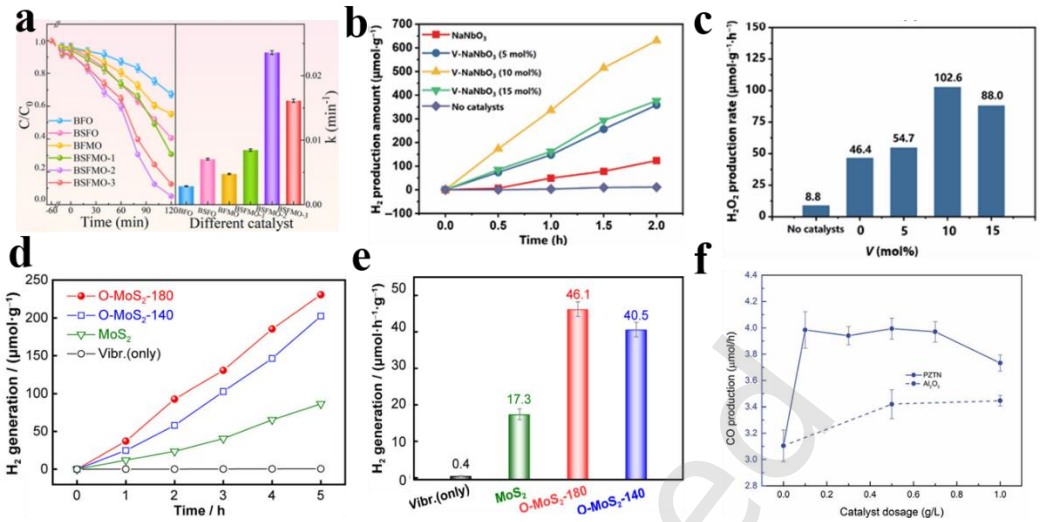


Figure 17 Representative piezocatalytic applications in energy conversion, resource recovery, and nitrogen conversion. (a) U(VI) reduction over $BiFeO_3$-based catalysts. Copyright 2022 Springer Nature [201].(b) H_2 evolution and (c) H_2O_2 production over V-doped $NaNbO_3$. Copyright 2022 Springer [170]. (d) Time-dependent H_2 generation and (e) Comparison of H_2 generation rates over pristine MoS_2 and oxygen-incorporated MoS_2. Copyright 2023 Springer[140]. (f) Piezocatalytic CO production rate. Copyright 2021 the Author(s)[23].

Just Accepted

1080 **Table 2** Doping-enhanced piezoelectric properties and piezocatalytic activity of representative materials.

Catalyst / dopant	Piezoelectric performance	Catalytic performance	Medium / co-reactant	Loading / activation	Ref.
$BaTiO_3$/Li	d_{33}: 145-191 pC N^{-1}; P_r: 7.5-11.3 μC cm^{-2}	30 mL RhB solution	200 mg; 180 W, 10 s work, 5 s rest)	RhB degradation: 90%; k: 0.021-0.149 min^{-1}	[163]
(Ba,Ca)(Zr,Ti)O_3/ Sm_2O_3	d_{33}: 540-612 pC N^{-1}	50 mL RhB, MB, or MO dye solution: 10 mg L^{-1}	40 kHz, 500 W	RhB degradation: 96.8%; k: 0.115 min^{-1}	[107]
(Ba,Ca)(Zr,Ti)O_3/	d_{33}: 520-645 pC N^{-1}	No sacrificial agent	-	Enhanced organic pollutant degradation	[34]
$BiFeO_3$/Co	d_{33}: 42-68 pm V^{-1}; P_r: 5.8-9.4μC cm^{-2}	20 mL RhB, MB, O7 dye solution: 10 mg L^{-1}	10 mg; 120 W, 40 kHz	Nearly complete dye degradation within 15 min; k: 0.067-0.198 min^{-1}	[164]
$BaTiO_3$/Nd	d_{33}: 191-247 pC N^{-1}; P_r: 11.3-14.8 μC cm^{-2}	50 mL RhB solution: 5 mg L^{-1}; 1.1 g/50 mL NaCl	50 mg; 40 kHz, 100 W	RhB degradation: 94%; k: 0.242 min^{-1}	[202]
$BiFeO_3$/Sm/Mn	d_{33}: 48-73 pm V^{-1}; P_r: 8.6-13.1 μC cm^{-2}	No sacrificial agents	30 mg; 40 kHz, 150 W	U(VI) reduction and H_2 evolution enhanced by 2.3- fold increase	[203]
$BaTiO_3$/Ca/Sr/Sn/ Hf	d_{33}: 450 pC N^{-1}	50 mL RhB solution	100 mg; 40 kHz, 100 W	Piezocatalytic activity greatly enhanced	[100]
ZnO/Ag	-	100 mL MO dye solution: 10 mg L^{-1}	100 mg; 40 kHz, 150 W	Dye degradation: 97%; k: 0.028-0.072 min^{-1}	[127]
0.97($Na_{0.5}Bi_{0.5}$)TiO_3-0.03Ba($Ni_{0.5}Nb_{0.5}$)O_3-xLa	d_{33}: 73–110 pC N^{-1}	30 mL RhB solution: 5 mg L^{-1}	60 mg; 33 ± 3 kHz, 180 W	RhB degradation: 100%; MB degradation: 96%; MO degradation: 88%	[204]
$BaTiO_3$/Ca	d_{33}: 145-330 pC N^{-1}; P_r:	50 mL RhB solution: 5 mg L^{-1}	50 mg; 40 kHz, 120 W	RhB degradation:	[205]

Just Accepted

	7.5-14.2 μC cm^{-2}	[1]		99%; TC degradation: 98%; *k*: 0.031-0.095 min^{-1}	
0.82Ba($Ti_{0.89}Sn_{0.11}$)O_3-0.18($Ba_{0.7}Ca_{0.3}$)TiO_3/Ca/Sn	d_{33}: 620-700 pC N^{-1}; P_r: 14.8-17.6 μC cm-2	50 mL RhB solution: 5 mg L^{-1}	100 mg; 40 kHz, 120 W	RhB degradation: >90%; *k*: 0.0706 min^{-1}	[206]
($Bi_{1/2}Na_{1/2}$)$_{1-x}Ba_xTiO_3$/ Ba	d_{33}: 110-181 pC N^{-1}; Pr: 8.2-27.6μC cm^{-2}	50 mL RhB solution: 10 mg L^{-1}	100 mg; 40 kHz, 320 W	RhB degradation: 98.95%; *k*: 0.026-0.082 min^{-1}	[206]
$NiTiO_3$/Cd	d_{33}: 7 pm V^{-1}	30 mL glucose solution: 0.1 mol L^{-1}	10 mg; 40 kHz, 200 W	H_2: 1520 μmol g^{-1} h^{-1} (13-fold)	[31]
$NaNbO_3$/V (10 mol%)	-	Intermediate water-splitting system; additional reagents NR	10 mg; 68 kHz, 192 W	H_2: 346.2 μmol g^{-1} h^{-1}; H_2O_2: 102.6 μmol g^{-1} h^{-1} (4.6- and 2.2-fold)	[170]
$Ba_2Nb_{2-x}Fe_xO_{6-\delta}$/Fe	d_{33}: 30 pm V^{-1}	50 mL pure water; air or O_2; no sacrificial agent	25 mg; 40 kHz, 180 W	H_2O_2: 512 μmol g^{-1} h^{-1} (air) and 690 μmol g^{-1} h^{-1} (O_2)	[113]
Bi_3TiNbO_9/Fe	d_{33}: 40 pm V^{-1}	40 mL deionized water and 10 mL ethanol	50 mg; 40 kHz, 300 W	H_2O_2: 1421.2 μmol g^{-1} h^{-1} (10.4-fold)	[152]
$Bi_4Ti_3O_{12}$/I	d_{33}: 179 pm V^{-1}	30 mL pure water; no sacrificial agent	5 mg; 40 kHz, 100 W	H_2O_2: 5890 μmol g-1 h-1	[149]
$Pb_{0.99}(Zr_{0.95}Ti_{0.05})_{0.03}$)/Nb (2%)	d_{33}: 69 pC N^{-1}	10 mL Na_2SO_3: 0.1 mol L^{-1}; 2% CO_2 in Ar	1 mg (0.1 g L^{-1}); 40 kHz	CO: 789 μmol g^{-1} h^{-1}; CO/H_2 > 7.6	[23]
MoS_2/O	-	20 ml pure water or 10% methanol	10 mg;40 kHz, 150 W	H_2: 46.1 μmol g^{-1} h^{-1} (water) and 921.0 μmol g^{-1} h^{-1} (methanol); MB degradation: 84.6%; *k*: 0.003→0.0546 min^{-1}	[140]
TiO_2@C/N	-	30 mL terephthalic acid	5 mg; 45 kHz, 200 W	H_2: 6.4 mmol g^{-1} h^{-1};	[195]

Just Accepted

		solution: 5 × 10^{-4} mol/L		k: 0.0546 min^{-1}	
$BiFeO_3$/La	-	RhB solution: 10^{-5} mol L^{-1}; no sacrificial agent	10 mg; 45 kHz, 100 W	RhB degradation: 100%; k: 0.2136 min^{-1}	[35]
PMN-xPT/Sm	d_{33}: 1150 pC N^{-1}	NR;	150 mg (1.5 g L^{-1}); 120 W	MO degradation; k:0.0453 min^{-1}	[156]
ZnAl-LDH/Co	-	20 mL of a mixture of peroxymonosulfate (0.5 mM) and norfloxacin (10 mg/L)	Mechanical conditions NR	Norfloxacin degradation: 91.5%; k: 0.1644 min^{-1}	[167]
HAP/F	d_{33}: 60 pm V^{-1}	Contaminated soil; 200 mg kg^{-1} phenanthrene	20 mg catalyst/2 g soil; 45 kHz, 50 W	Phenanthrene degradation: 78.99%; k: 0.01389 min^{-1}	[191]
ZnS/Mn	d_{33}: 23.3 pm V^{-1}	MB and RhB aqueous solution	20 mg; 40 kHz	MB degradation: 95%; RhB degradation: 95%； k: 0.1376 min^{-1} (MB); 0.1048 (RhB) min^{-1}	[187]
Zn-N_x-C/Zn,N	-	16 mL aqueous methanol solution: 9.4%; 30 mL RhB solution: 10 mg/L	5 mg for H_2 generation; 30 mg for RhB degradation; 40 kHz, 180 W	H_2: 6.29 mmol g^{-1} h^{-1}; RhB degradation: 94%	[190]

1081

Just Accepted

4.3 Tumor therapy and regenerative medicine

Beyond environmental remediation and energy conversion, doped piezocatalytic materials have recently emerged as a promising platform for biomedical applications, including tumor therapy[200, 207-210], antibacterial treatment[211, 212], biofilm eradication[101, 153, 213, 214], postoperative infection control [153, 213, 215] , and tissue regeneration[213]. Compared with conventional catalytic systems, piezocatalytic therapy utilizes ultrasound as a non-invasive mechanical stimulus owing to its deep tissue penetration, excellent spatial controllability, and ability to activate piezoelectric materials *in situ*. Under ultrasound irradiation, polarization charges generated by piezoelectric materials react with dissolved O_2, H_2O, and endogenous H_2O_2 to produce ROS, including $\bullet O_2^-$, •OH,[2, 216, 217], and $^1O_2$ [218], which disrupt intracellular redox homeostasis and induce tumor-cell death or bacterial inactivation. However, pristine piezocatalysts generally suffer from limited ROS generation, rapid carrier recombination, and insufficient catalytic activity under physiological conditions. Doping engineering therefore provides an effective strategy to simultaneously regulate lattice distortion, defect chemistry, polarization intensity, electronic structure, catalytic active sites, and biointerfacial interactions, thereby substantially improving therapeutic performance.

Tumor therapy represents one of the most extensively investigated biomedical applications of doped piezocatalysts. Mn-doped ZnO provides a representative example, where Mn incorporation induces lattice distortion and oxygen-vacancy formation, strengthening piezoelectric polarization and facilitating ultrasound-triggered charge separation (**Figure 18a-c**)[38]. The enhanced piezoelectric response promotes ROS-mediated oxidative stress, resulting in glutathione depletion, glutathione peroxidase 4 (GPX4) downregulation, lipid peroxidation, and ultimately ferroptotic tumor-cell death. This example demonstrates that doping engineering can regulate both piezoelectric charge dynamics and intracellular therapeutic pathways. Beyond regulating piezoelectric properties, dopant-induced active centers can further enhance catalytic reactions involved in tumor therapy. For example, Fe single-atom-doped MoS_2 nanosheets contain atomically dispersed Fe sites that accelerate interfacial charge transfer and exhibit enhanced nanozyme-like catalytic activity (**Figure 18d-f**)[219]. The isolated Fe centers improve peroxidase-like and Fenton-like activities, promoting the conversion of endogenous H_2O_2 into highly reactive species and amplifying

Just Accepted

oxidative stress within tumor cells. The synergistic integration of piezocatalytic activation and nanozyme-mediated catalytic reactions provides an effective strategy for enhancing tumor therapeutic efficacy. In addition to regulating cellular therapeutic mechanisms, doping engineering can also improve the in vivo performance of piezocatalytic materials by modulating their biological interactions and biodistribution. Fe-doped hexagonal $YMnO_3$ exhibits efficient tumor accumulation and favorable distribution in major organs, thereby enhancing ultrasound-triggered therapeutic efficacy while minimizing systemic toxicity (**Figure 18g**)[111].

In addition to tumor therapy, doped piezocatalysts have demonstrated remarkable potential in antibacterial treatment, infection control, and tissue regeneration. Guanidine-functionalized Cu-doped $BaTiO_3$ integrates piezocatalytic activation with bacterial targeting, enabling localized ROS generation for efficient bacterial eradication while simultaneously promoting osteogenic differentiation (**Figure 18h**)[153]. Likewise, Fe-doped ultrathin $Bi_4Ti_3O_{12}$ nanosheets combine piezocatalysis with chemodynamic therapy, where Fe-induced oxygen vacancies, enhanced charge separation, and Fe^{2+}/Fe^{3+} redox cycling synergistically promote antibacterial activity and accelerate wound healing (**Figure 18i**)[220].

From the perspective of regenerative medicine, doping engineering can further regulate biointerfacial interactions and cellular responses in addition to enhancing piezocatalytic activity. The guanidine-functionalized Cu-doped $BaTiO_3$ (Cu-BTO@Gua) system promotes osteogenic differentiation while achieving antibacterial effects, whereas Fe-doped $Bi_4Ti_3O_{12}$ simultaneously enhances antibacterial activity and wound healing. These results demonstrate that rational doping can integrate infection control with tissue regeneration, providing a promising strategy for multifunctional biomedical piezocatalytic platforms.

Just Accepted

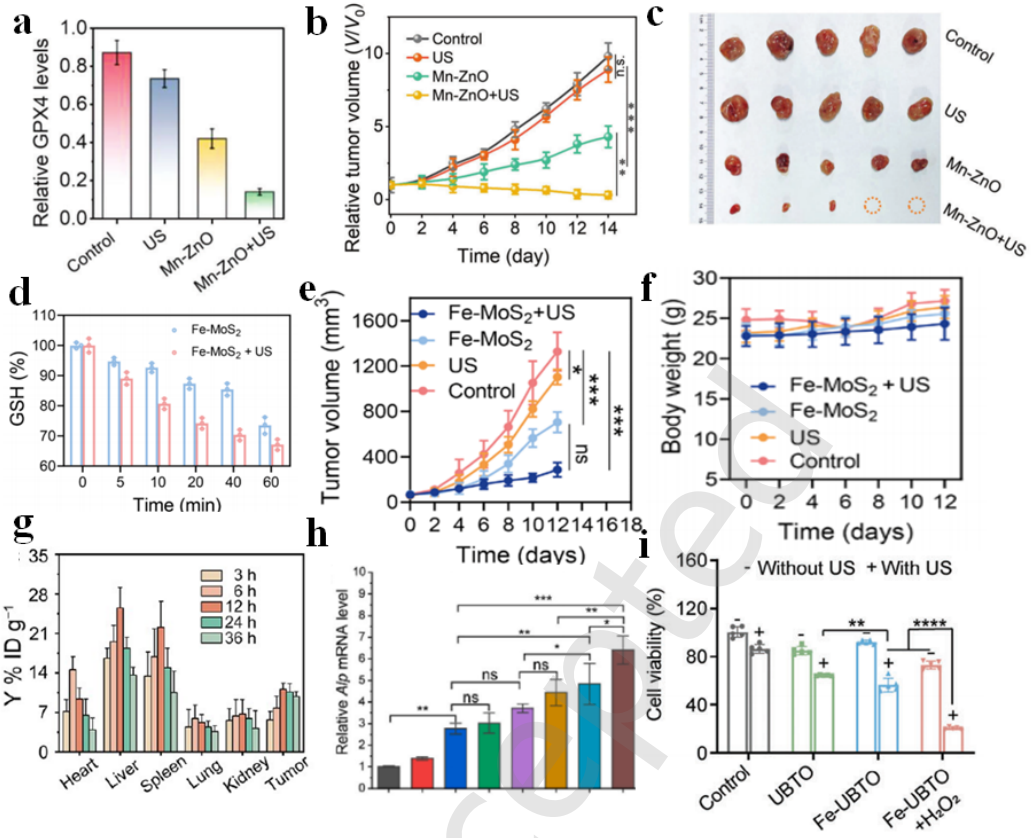


Figure 18 Representative biomedical applications of doped piezocatalytic materials. (a) Relative GPX4 levels of control, US, Mn-ZnO, and Mn-ZnO+US groups. (b) Relative tumor volume changes during Mn-ZnO-mediated ultrasound therapy. (c) Photographs of tumor tissues collected from different treatment groups. Copyright 2023 Wiley [38]. (d) GSH depletion performance of Fe-MoS_2 under different treatment conditions. (e) Tumor growth inhibition of Fe-MoS_2 under ultrasound irradiation. (f) Body-weight changes of mice during Fe-MoS_2-mediated therapy. Copyright 2025 American Chemical Society [219]. (g) Fe-doped hexagonal $YMnO_3$. Copyright 2025 American Chemical Society [111]. (h) Cu-BTO@Gua for MRSA-infected osteomyelitis. Copyright 2025 the Author(s)[153]. (i) Fe-doped $Bi_4Ti_3O_{12}$ for piezo-chemodynamic therapy. Copyright 2025 Wiley [220].

4.4 Antibacterial disinfection and infection control

Beyond environmental remediation and biomedical therapy, doped piezocatalytic materials have recently attracted increasing attention for antibacterial disinfection, biofilm eradication, implant-associated infection control, and self-powered water sterilization[101, 153, 213, 220, 221]. Compared with conventional sterilization

Just Accepted

technologies, piezocatalytic disinfection utilizes mechanical energy derived from ultrasound, vibration, fluid flow, or shear stress to continuously generate ROS without external light irradiation or electrical input. Under mechanical stimulation, piezoelectric polarization drives electron–hole separation, where electrons reduce dissolved oxygen to generate superoxide radicals, while holes oxidize surface hydroxyl groups or water molecules to produce hydroxyl radicals[222],

$$O_2 + e^- \rightarrow O_2^- \quad (9)$$

$$H_2O/OH^- + h^+ \rightarrow \bullet OH \quad (10)$$

The generated ROS induce oxidative damage to bacterial membranes, proteins, lipids, and DNA, while disrupting extracellular polymeric substances, thereby inhibiting bacterial proliferation and promoting biofilm destruction. However, pristine piezoelectric materials generally suffer from insufficient polarization intensity, rapid carrier recombination, limited ROS generation, and weak bacteria-material interactions. Consequently, doping engineering has emerged as an effective strategy for simultaneously regulating polarization response, defect chemistry, charge-transfer dynamics, catalytic active sites, and biointerfacial interactions to enhance antibacterial performance.

One of the major challenges in antibacterial therapy is the eradication of mature bacterial biofilms, which effectively protect microorganisms from antibiotics and host immune responses. Guanidine-functionalized Cu-doped $BaTiO_3$ (Cu-BTO@Gua) represents a representative strategy integrating doping engineering with biointerface regulation (**Figure 19a-c**)[153]. In this system, Cu doping enhances piezoelectric polarization, defect-mediated charge separation, and ROS generation, while guanidine functionalization further strengthens bacteria-material interactions by improving bacterial adhesion and biofilm affinity. As shown in **Figure 19a**, Cu-BTO@Gua exhibits concentration- and time-dependent adhesion to MRSA, facilitating its interaction with bacteria. Furthermore, Cu-BTO@Gua combined with ultrasound effectively reduces toxin-induced hemolysis (**Figure 19b**), demonstrating its toxin-inactivation capability. In vivo experiments further reveal a substantial reduction in bacterial burden in MRSA-infected osteomyelitis models, particularly under ultrasound stimulation (**Figure 19c**). These findings highlight the importance of synergistically regulating piezoelectric activity, bacterial targeting, and biointerfacial interactions for effective antibacterial therapy.

Just Accepted

Another representative strategy involves Fe-doped $Bi_4Ti_3O_{12}$ nanosheets (Fe-UBTO), in which Fe incorporation induces lattice distortion and oxygen vacancies, enhancing ultrasound-responsive piezocatalytic activity and promoting synergistic piezo-chemocatalytic tumor therapy[101]. As shown in **Figure 19d**, Fe-UBTO combined with ultrasound and H_2O_2 markedly reduces tumor-cell viability, demonstrating enhanced antitumor activity through coupled piezocatalytic and chemical catalytic processes. Furthermore, the representative tumor photographs (**Figure 19e**) and corresponding tumor growth inhibition curves (**Figure 19f**) demonstrate that Fe-UBTO incorporated into a hydrogel (Fe-UBTO@Gel) effectively suppresses tumor growth under ultrasound stimulation. These findings highlight the potential of doping engineering to improve piezocatalytic tumor therapy by modulating material properties and facilitating mechanically activated therapeutic reactions.

Collectively, these studies demonstrate that doping engineering can enhance biomedical piezocatalysis through coordinated regulation of piezoelectric polarization, defect chemistry, reactive oxygen species generation, and biointerfacial interactions. The Cu-BTO@Gua and Fe-UBTO systems illustrate complementary applications in antibacterial treatment and tumor therapy, respectively, highlighting the potential of doping-engineered materials for multifunctional biomedical applications.

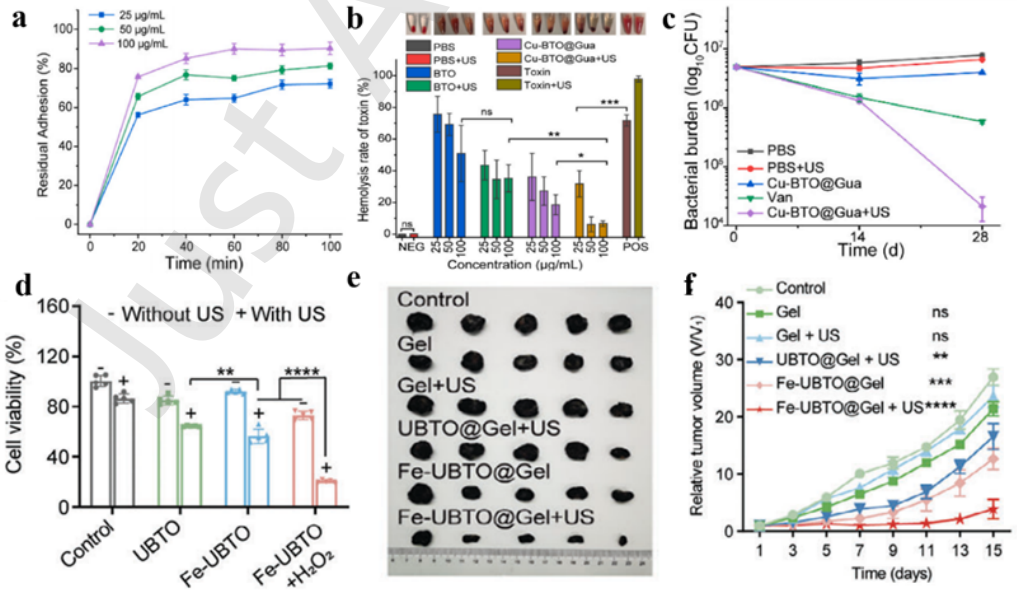


Figure 19 Representative biomedical applications of doping-engineered piezocatalysts. (a) Time- and concentration-dependent adhesion of Cu-BTO@Gua to MRSA. (b) Hemolysis induced by MRSA-secreted toxins following different Cu-BTO@Gua treatments, reflecting toxin-inactivation efficacy. (c) Changes in bacterial

Just Accepted

burden in the bone marrow of MRSA-infected osteomyelitis models under different treatments. Copyright 2025 the Author(s)[153]. (d) Viability of B16-F10 tumor cells treated with UBTO, Fe-UBTO, and Fe-UBTO/H_2O_2 under conditions with or without ultrasound irradiation. (e) Representative tumor photographs following different Fe-UBTO@Gel-based treatments. (f) Relative tumor volume changes under different Fe-UBTO@Gel-based treatments with or without ultrasound irradiation. Copyright 2024 Wiley[220].

5. Conclusions and outlook

Doping engineering has emerged as a powerful strategy for advancing piezocatalytic materials by enabling simultaneous regulation of crystal structure, defect chemistry, electronic configuration, and piezoelectric properties. In this review, we systematically summarized the fundamental roles of dopants in modifying lattice distortion, chemical bonding, symmetry breaking, defect formation, carrier behavior, and polarization response. These structural and electronic modifications collectively determine the generation and utilization of piezoelectric potentials, thereby governing charge separation, interfacial redox reactions, and catalytic efficiency. Rather than serving as a simple compositional adjustment, doping engineering provides a multidimensional platform for establishing structure, property and performance relationships in piezocatalytic systems. Importantly, this review integrates doping-induced structural reconstruction, defect regulation, electronic modulation, and piezoelectric polarization into a unified mechanistic framework, establishing connections between atomic-scale dopant configurations, macroscopic electromechanical responses, and interfacial catalytic processes. By systematically examining the beneficial and adverse effects of doping, as well as the influence of synthesis routes, mechanical excitation conditions, and material characteristics, this review provides a more comprehensive understanding of the factors governing piezocatalytic performance. These insights extend beyond conventional empirical optimization and offer a basis for mechanism-guided dopant selection and rational materials design. These insights extend beyond conventional empirical optimization and offer a basis for mechanism-guided dopant selection and rational materials design. Nevertheless, several critical challenges remain in achieving precise dopant regulation, understanding coupled electromechanical and catalytic mechanisms, and ensuring long-term performance. As summarized in **Figure 20,**

Just Accepted

addressing these challenges requires coordinated advances in dopant characterization, defect and phase control, polarization–carrier analysis, standardized performance evaluation, mechanistic investigation, and scalable synthesis.

Appropriate dopant incorporation can induce lattice distortion, optimize local coordination environments, and regulate defect chemistry, thereby enhancing piezoelectric polarization, charge transport, and interfacial reaction kinetics. However, excessive doping may introduce structural disorder, secondary phases, recombination centers, and charge-screening effects, ultimately deteriorating piezocatalytic performance [27, 109, 223]. These competing effects highlight the need to move beyond empirical concentration optimization toward precise control of dopant incorporation, lattice-site occupancy, defect compensation, and phase stability. Since nominal dopant concentrations do not necessarily reflect actual lattice incorporation, quantitative compositional analysis combined with complementary techniques, including inductively coupled plasma mass spectrometry (ICP-MS), scanning transmission electron microscopy with energy-dispersive X-ray spectroscopy (STEM-EDS), and X-ray absorption spectroscopy (XAS), is essential for verifying dopant configurations and identifying suitable doping windows. Moreover, synthesis routes and processing conditions influence dopant distribution, defect formation, and phase stability, meaning that identical nominal compositions may exhibit different piezoelectric and catalytic responses[50, 53]. Future studies should therefore establish quantitative correlations among synthesis parameters, actual dopant incorporation, defect chemistry, polarization behavior, and catalytic kinetics to enable mechanism-guided materials design.

A key challenge is to clarify the quantitative relationship among piezoelectric polarization, carrier dynamics, and catalytic performance, as enhanced piezoelectricity does not necessarily lead to improved catalytic activity. Future studies should combine PFM, piezocurrent measurements, and EIS to distinguish polarization enhancement from charge-screening and carrier-transport effects, thereby establishing reliable correlations between electromechanical properties and catalytic efficiency. Standardized performance evaluation is essential for establishing reliable structure–property–activity relationships. Variations in catalyst morphology, dopant concentration, mechanical excitation conditions, and reaction environments can significantly affect catalytic performance. Future studies should employ comparable experimental conditions and appropriate controls to distinguish piezoelectric

Just Accepted

contributions from other mechanically induced effects, including flexocatalysis, tribocatalysis, and sonocatalysis, which may coexist under mechanical stimulation[224],while integrating standardized datasets with data-driven modeling to support predictive dopant design. Understanding dynamic catalytic pathways and rate-determining steps remains another important challenge. Future investigations should integrate in situ and operando characterization with density functional theory (DFT) calculations and kinetic analyses to clarify the evolution of dopant-related defects, active sites, and reaction intermediates under mechanical stimulation. Such approaches will provide mechanistic insights into doping-dependent reaction pathways and catalytic selectivity. Long-term stability, catalytic durability, and scalable fabrication are essential for practical applications. Repeated mechanical stimulation may induce dopant migration, defect redistribution, structural degradation, and elemental leaching. Future studies should establish standardized durability protocols and develop reproducible synthesis strategies to ensure structural stability, consistent catalytic performance, and scalable production. Application-oriented research should address the specific challenges of environmental remediation, energy conversion, and biomedical technologies. Environmental applications require improved stability and performance under realistic wastewater conditions [172, 225, 226]. while energy conversion demands greater attention to product selectivity, energy efficiency, and operational durability [172]. For biomedical applications, long-term biosafety, biodegradation, and biological responses remain critical challenges[227]. Addressing these issues through application-specific evaluation and materials optimization will facilitate the practical implementation of doping-engineered piezocatalysts.

Overall, the future development of doping-engineered piezocatalysts requires a transition from empirical optimization toward mechanism-guided and predictive materials design. Integrating in situ and operando characterization, theoretical calculations, and data-driven approaches will help establish quantitative structure–property–activity relationships by linking dopant configurations, defect chemistry, piezoelectric polarization, and interfacial reaction kinetics. Such advances will facilitate the development of efficient, selective, stable, and scalable piezocatalytic systems for environmental remediation, sustainable energy conversion, and biomedical applications.

Just Accepted

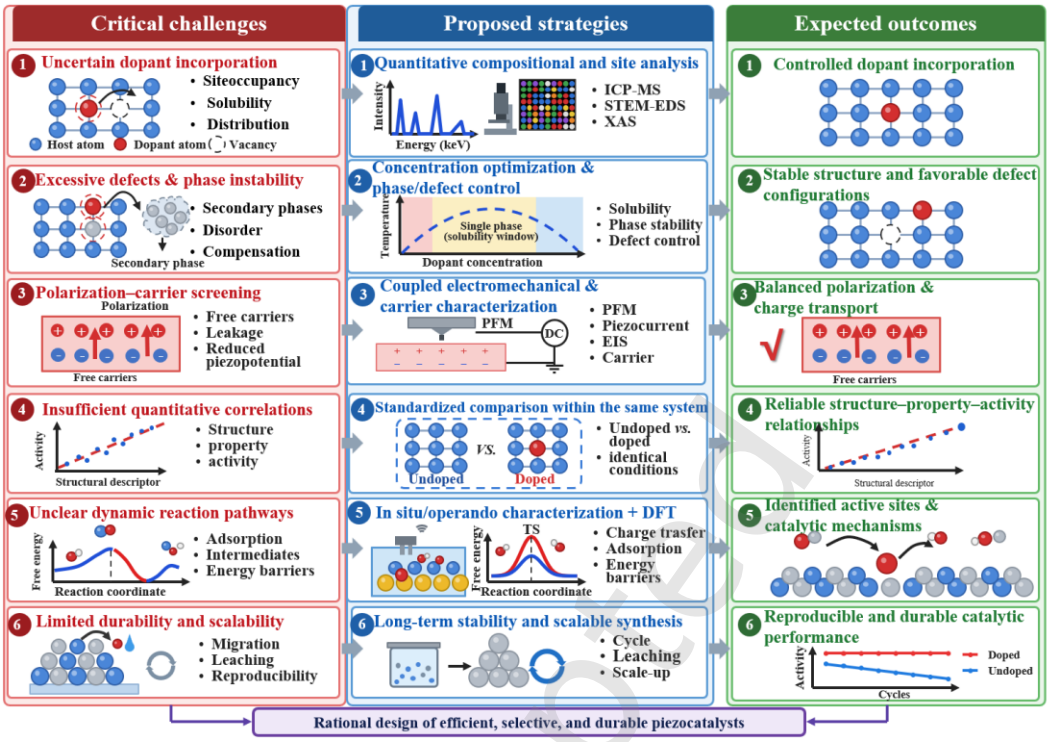


Figure 20 Schematic illustration of critical challenges and proposed strategies for doping-engineered piezocatalysts.

Declaration of competing interests

The authors declare that they have no known competing financial interests or personal relationships that could have appeared to influence the work reported in this paper.

Data availability

No data was used for the research described in the article.

Acknowledgements

This work is financially supported by the National Natural Science Foundation of China (22309170, 22179108), the Natural Science Foundation of Zhejiang Province (LQ24E020003, LQN25E020017, LD25B060001), and the Fundamental Research Funds for the Provincial Universities of Zhejiang (2024YW14, 2025QN065).

Just Accepted

References:

1. Liu, D., J. Zhang, L. Tan, et al., Enhanced piezocatalytic hydrogen evolution performance of bismuth vanadate by the synergistic effect of facet engineering and cocatalyst engineering. *J. Colloid Interface Sci*, 2023. **646**: 159-166.
2. Wang, Y., Y. Xu, S. Dong, et al., Ultrasonic activation of inert poly(tetrafluoroethylene) enables piezocatalytic generation of reactive oxygen species. *Nat. Commun*, 2021. **12(1)**: 3508.
3. Kubota, K., Y. Pang, A. Miura, et al., Redox reactions of small organic molecules using ball milling and piezoelectric materials. *Science*, 2019. **366**(6472): 1500-1504.
4. Kharlamova, T.S., M.V. Salina, V.A. Svetlichnyi, et al., CeO_2-supported Pt–Ag bimetallic catalysts for 4-nitrophenol reduction. *Catal. Today*, 2022. **384-386**: 12-24.
5. Song, Z., R. Hou, and F. Jiang, Recent progress in piezoelectric thin films as self-powered devices: material and application. *Front. Mater*, 2024. **11**: 1373040.
6. Dai, J., Z. Fan, H. Xie, et al., Versatile $BiFeO_3$ shining in piezocatalysis: From materials engineering to diverse applications. *J. Adv. Ceram*, 2025. **14**(3): 9221046.
7. Xu, M.L., M. Lu, G.Y. Qin, et al., Piezo-photocatalytic synergy in $BiFeO_3$@COF Z-Scheme heterostructures for high-efficiency overall water splitting. *Angew*, 2022. **61**(44): e202210700
8. You, H., Z. Wu, L. Zhang, et al., Harvesting the vibration energy of $BiFeO_3$ nanosheets for hydrogen evolution. *Angew*, 2019. **58**(34): 11779-11784.
9. Yu, C., M. Tan, Y. Li, et al., Ultrahigh piezocatalytic capability in eco-friendly $BaTiO_3$ nanosheets promoted by 2D morphology engineering. *J. Colloid Interface Sci*, 2021. **596**: 288-296.
10. Jin, C., D. Liu, J. Hu, et al., The role of microstructure in piezocatalytic degradation of organic dye pollutants in wastewater. *Nano Energy*, 2019. **59**: 372-379.
11. Liu, X., L. Shen, W. Xu, et al., Low frequency hydromechanics-driven generation of superoxide radicals via optimized piezotronic effect for water disinfection. *Nano Energy*, 2021. **88**: 106290.
12. Li, H., H. Li, M. Du, et al., A perspective on field-effect in energy and environmental catalysis. *Chem. Sci*, 2025. **16**(4): 1506-1527.
13. Wu, A., L. Jiang, C. Xia, et al., Ultrasound-driven piezoelectrocatalytic immunoactivation of deep tumor. *Adv Sci*, 2023. **10**(28): e2303016.
14. Wang, Y., X. Wen, Y. Jia, et al., Piezo-catalysis for nondestructive tooth whitening. *Nat. Commun*, 2020. **11**: 1328.
15. Zhang, H.Y., A small-molecule organic ferroelectric with piezoelectric voltage coefficient larger than that of lead zirconate titanate and polyvinylidene

Just Accepted

difluoride. *Chem. Sci*, 2022. **13**(17): 5006-5013.
16. Xu, X., Y. Jia, L. Xiao, et al., Strong vibration-catalysis of ZnO nanorods for dye wastewater decolorization via piezo-electro-chemical coupling. *Chemosphere*, 2017. **193**: 1143-1148.
17. Wang, B., Q. Zhang, J. He, et al., Co-catalyst-free large ZnO single crystal for high-efficiency piezocatalytic hydrogen evolution from pure water. *J. Energy Chem*, 2021. **65**: 304-311.
18. Peng, F., J. Lin, H. Li, et al., Design of piezoelectric ZnO based catalysts for ammonia production from N_2 and H_2O under ultrasound sonication. *Nano Energ*, 2022. **95**: 107020.
19. Wang, J., C. Hu, Y. Zhang, et al., Engineering piezoelectricity and strain sensitivity in CdS to promote piezocatalytic hydrogen evolution. *Chinese J. Catal*, 2022. **43**(5): 1277-1285.
20. Xue, K., Y. Jiang, S. S. Mofarah, et al., Composition-driven morphological evolution of $BaTiO_3$ nanowires on efficient piezocatalytic hydrogen production. *Chemosphere*, 2023. **338**: 139337.
21. Wang, X., X. Gao, M. Li, et al., Synthesis of flexible $BaTiO_3$ nanofibers for efficient vibration-driven piezocatalysis. *Ceram. Int*, 2021. **47**(18): 25416-25424.
22. Wu, J., N. Qin, and D. Bao, Effective enhancement of piezocatalytic activity of $BaTiO_3$ nanowires under ultrasonic vibration. *Nano Energy*, 2018. **45**: 44-51.
23. Zhang, Y., P.T. Thuy Phuong, N.P. Hoang Duy, et al., Polarisation tuneable piezo-catalytic activity of Nb-doped PZT with low curie temperature for efficient CO_2 reduction and H_2 generation. *Nanoscale Adv*, 2021. **3**(5): 1362-1374.
24. He, J., F. Gao, H. Wang, et al., C-doped $KNbO_3$ single crystals for enhanced piezocatalytic intermediate water splitting. *Environ. Sci-Nano*, 2022. **9**(6): 1952-1960.
25. Lan, S., C. Yu, F. Sun, et al., Tuning piezoelectric driven photocatalysis by La-doped magnetic $BiFeO_3$-based multiferroics for water purification. *Nano Energy*, 2022. **93**: 106792.
26. Beh, E.S., S.A. Basun, X. Feng, et al., Molecular catalysis at polarized interfaces created by ferroelectric $BaTiO_3$. *Chem. Sci*, 2017. **8**(4): 2790-2794.
27. Dong, H., Y. Zhou, L. Wang, et al., Oxygen vacancies in piezocatalysis: A critical review. *Chem. Eng. J*, 2024. **487**: 150480.
28. Wang, Y., X. Xu, L. Xiao, et al., Balancing the piezoelectric coefficient and carrier concentration of Bi_2WO_{6-x} for ultrahigh piezocatalysis. *J. Adv. Ceram*, 2024. **13**(11): 1737-1747.
29. Wen, Q., H.-H. Guo, Z.-Y. Shen, et al., MnO_2 doping induced structural tuning drives superior piezoelectric response in $CaBi_4Ti_4O_{15}$-based ceramics. *J. Adv. Ceram*, 2025. **14**(4): 9221051.
30. Xu, X., Y. Wang, W. Cheng, et al., Thickness-regulated interfacial polarization

Just Accepted

in CTAB-tailored Bi_2WO_6 for enhanced piezocatalysis. *J. Adv. Ceram*, 2026. **15**(3): 9221255.
31. Li, K., B. Li, X. Zhang, et al., Enhancement of $NiTiO_3$ piezocatalytic hydrogen evolution by doping with large radius elements. *Chem. Commun*, 2024. **60**(36): 4801-4804.
32. Zhou, P.N.F.L.H.K.Y., Advances in Piezoelectric Properties of Textured Ferroelectric Ceramics with Perovskite Structure.pdf. *Adv. Ceram*, 2024. **02-0171-24**: 1005-1198.
33. Wang, K. and Y. He, Recent advances in metal titanate-based piezocatalysts: Enhancing catalytic performance through improved piezoelectric properties and regulated carrier transport. *Chin. J. Catal.*, 2024. **61**: 111-134.
34. Wang, X., Y. Huan, S. Ji, et al., Ultra-high piezoelectric performance by rational tuning of heterovalent-ion doping in lead-free piezoelectric ceramics. *Nano Energy*, 2022. **101**: 107580.
35. Amdouni, W., M. Otonicar, D. Alamarguy, et al., Enhancement of the piezocatalytic response of La-doped $BiFeO_3$ nanoparticles by defects synergy. *Small*, 2024. **20**(50): e2406425.
36. Kirubasankar, B., Y.S. Won, L.A. Adofo, et al., Atomic and structural modifications of two-dimensional transition metal dichalcogenides for various advanced applications. *Chem. Sci*, 2022. **13**(26): 7707-7738.
37. Chen, X., B. Ou, G. Liu, et al., Simultaneous enhancement of piezoelectric performance and Curie temperature in high-temperature $Bi_4Ti_3O_{12}$ piezoceramics through A/B site co-doping. *J. Adv. Ceram*, 2025. **14**(5): 9221077.
38. Tian, B., R. Tian, S. Liu, et al., Doping engineering to modulate lattice and electronic structure for enhanced piezocatalytic therapy and ferroptosis. *Adv. Mater*, 2023. **35**(38): e2304262.
39. Lu, X., R. Zhang, Y. Liu, et al., Oxygen vacancies and lattice distortion synergistically enhanced piezocatalysis of $CaZn_2(BO_3)_2$ for nonantibiotic pharmaceutical degradation. *ACS Appl. Mater. Int*, 2024. **16**(46): 63692-63702.
40. Tian, W., J. Han, L. Wan, et al., Enhanced piezocatalytic activity in ion-doped SnS_2 via lattice distortion engineering for BPA degradation and hydrogen production. *Nano Energy*, 2023. **107**: 108165.
41. Chen, J.C., M.J. Pei, W.B. Yu, et al., New theoretical insights into doping-induced enhancement of ORR activity in molybdenum disulfide: d-p hybridization or the Jahn-Teller effect? *Chem. Sci*, 2026. **17**(7): 3758-3774.
42. Dai, J., Z. Fan, Y. Long, et al., Remarkably boosting piezocatalytic performance of $Sr_{0.5}Ba_{0.5}Nb_2O_6$ piezoceramics via size optimization and oxygen vacancy engineering. *Adv. Funct. Mater*, 2024. **34**(48): 2408754.
43. Sun, C., P. Beaunier, V. La Parola, et al., Ni/CeO_2 nanoparticles promoted by yttrium doping as catalysts for CO_2 methanation. *ACS Appl. Nano. Mater*, 2020. **3**(12): 12355-12368.
44. Zhao, D., X. Deng, and L. Yang, High-entropy doping and defect co-

Just Accepted

engineering to synergistically boost piezo-catalytic activity of $BaTiO_3$-based materials. *Ceram. Int.*, 2024. **50(9)**: 16412-16424.
45. Xu, X., L. Liu, and Y. Tong, Facile Cr^{3+}-doping strategy dramatically promoting Ru/CeO_2 for low-temperature CO_2 methanation: unraveling the roles of surface oxygen vacancies and hydroxyl groups. *ACS Catal.*, 2021. **11(9)**: 5762-5775.
46. Xu, X., Y. Wang, and W. Cheng, Recent advances in piezocatalytic hydrogen production and prospects. *Surf. Interf.*, 2024. **54**: 105245.
47. Hou, X., K. Wang, and J. Wang, Doping-induced piezoelectricity in Ba2Nb_(2-x)Fe_(x)O_(6-delta) double perovskite oxides for efficient hydrogen peroxide production via piezocatalysis in pure water. *J. Colloid Interface Sci.*, 2024. **674**: 256-265.
48. Kang, Z., M. Chen, and J. Wu, Insights on enhancing piezocatalytic performance of Bi_2WO_6@PDA homojunction from phase coexistence and electron transfer mediators. *J. Colloid Interface Sci.*, 2023.
49. Yan, Y., K.-H. Cho, and S. Priya, Role of Secondary Phase in High Power Piezoelectric PMN-PZT Ceramics. *J. Am. Ceram. Soc*, 2011. **94**(12): 4138-4141.
50. Feng, Y., J. Wu, Q. Chi, et al., Defects and aliovalent doping engineering in electroceramics. *Chem. Rev*, 2020. **120**(3): 1710-1787.
51. Meng, N., W. Liu, R. Jiang, et al., Fundamentals, advances and perspectives of piezocatalysis: A marriage of solid-state physics and catalytic chemistry. *Prog. Mater Sci*, 2023. **138**: 101161.
52. Zhou, L., L. Meng, H. Jia, et al., Recent advances in piezocatalysts for dye degradation. *Adv. Sustain. Syst*, 2024. **8**: 2300652.
53. A. Randall, C., H. Nishiyama, and H. Shimizu, Impact of volatility, non-stoichiometry, and atmospheres in perovskite piezoelectric and dielectric materials. *J. Am. Ceram. Soc*, 2024. **107**(12): 7921-7938.
54. Su, Y., Q. Wang, Y. Huan, et al., Concurrently enhanced piezoelectric performance and curie temperature in stressed lead-free $Ba_{0.85}Ca_{0.15}Ti_{0.9}Zr_{0.1}O$-ceramics. *Nat. Commun*, 2025. **16**(1): 4049.
55. Jiang, T., Y. Wang, and C. Cai, Piezocatalysis for water treatment: Mechanisms, recent advances, and future prospects. *Environ. Sci. Ecotechnol.*, 2025. **23**: 100495.
56. Meng, F., C. Guo, and T. Cui, Piezoelectric catalysis for antibacterial applications. *Mater. Chem. Front.*, 2025. **9(2)**: 171-188.
57. Tu, S., Y. Guo, Y. Zhang, et al., Piezocatalysis and Piezo-Photocatalysis: Catalysts Classification and Modification Strategy, Reaction Mechanism, and Practical Application. *Adv. Funct. Mater*, 2020. **30**(48): 2005108.
58. Zhou, X., B. Shen, A. Lyubartsev, et al., Semiconducting piezoelectric heterostructures for piezo- and piezophotocatalysis. *Nano Energy*, 2022. **96**: 107141.
59. Chen, F., H. Huang, L. Guo, et al., The Role of Polarization in Photocatalysis. *Angew*, 2019. **58**(30): 10061-10073.

Just Accepted

60. Shi, H., Y. Liu, Y. Bai, et al., Progress in defect engineering strategies to enhance piezoelectric catalysis for efficient water treatment and energy regeneration. *Sep. Purif. Technol.*, 2024. 330: 125247.
61. Lu, Y., H. Cao, S. Xu, et al., CO_2 photoelectroreduction with enhanced ethanol selectivity by high valence rhenium-doped copper oxide composite catalysts. *J. Colloid Interface Sci*, 2021. **599**: 497-506.
62. Shin, J., C. Andreas Hutomo, J. Kim, et al., Natural pollen exine-templated synthesis of photocatalytic metal oxides with high surface area and oxygen vacancies. *Appl. Surf. Sci*, 2022. **599**: 154064.
63. Wang, Y., X. Yuan, J. Ye, et al., Effects of zinc/gallium dual doping on the physicochemical properties and cell response of 3D printed β-tricalcium phosphate ceramic scaffolds. *Ceram. Int*, 2022. **48**(19): 28557-28564.
64. Wang, C., Y. Hu, C. Lan, et al., Densification, microstructure, tribological and electrochemical properties of pure Zn fabricated by laser powder bed fusion. *J. Alloys Compd*, 2023. **955**: 170227.
65. Zhuang, W., Y. Zhang, and Q. Luo, Piezoelectric catalytic process: A genuinely energy-saving approach for water Treatment? A critical review. *Chem. Eng. J.*, 2024. **499**: 155956.
66. Zhang, X., H.S. Chen, S.P. Jiang, et al., $W_{18}O_{49}$/crystalline g-C_3N_4 layered heterostructures with full solar energy harvesting towards efficient H_2O_2 generation and NO conversion. *Nano Energy*, 2024. **120**: 109160.
67. Klein, A., K. Albe, N. Bein, et al., The fermi energy as common parameter to describe charge compensation mechanisms: A path to Fermi level engineering of oxide electroceramics. *J. Electroceram*, 2023. **51**(3): 147-177.
68. Ha, S.-J., Y.K. Moon, and H.-A. Cha, A defect-chemical framework for transparent piezoelectric perovskites through donor-induced phase transitions. *J. Adv. Ceram.*, 2026.
69. Tian, B., R. Tian, S. Liu, et al., Doping engineering to modulate lattice and electronic structure for enhanced piezocatalytic therapy and ferroptosis. *Adv. Mater.*, 2023. **35**(38): 2304262.
70. Bhadwal, N., R. Ben Mrad, and K. Behdinan, Review of zinc oxide piezoelectric nanogenerators: piezoelectric properties, composite structures and power output. *Sensors*, 2023. **23**(8): 3859.
71. Ti, J., J. Li, Q. Fan, et al., Sm-doped PZT thin film with high piezoelectric properties by sol-gel method. *J. Appl. Phys*, 2024. **136**(5): 055302
72. Toroń, B., W. Matysiak, A. Starczewska, et al., Electrospun fabrication of 1–3-Type PVP/SbSI and PVP/SbSeI nanocomposites with excellent piezoelectric properties for nanogenerators and sensors. *Energies*, 2025. **18**(20): 5506.
73. Ke, F.L.H.L.M.Z.D.J.Y.Z.H., Preparation and Particle Size Control of Scandium-Doped Zirconia Submicron Powders via Homogeneous Co-precipitation Method. *Adv Mater*, 2026. **04-0354-12**: 1005-1198.
74. Zhang, M., C. Liu, B. Li, et al., Electrospun PVDF-based piezoelectric

Just Accepted

nanofibers: materials, structures, and applications. *Nanoscale Adv*, 2023. **5**(4): 1043-1059.
75. He, Z., F. Rault, M. Lewandowski, et al., Electrospun PVDF nanofibers for piezoelectric applications: A review of the influence of electrospinning parameters on the beta phase and crystallinity enhancement. *Polymers*, 2021. **13**(2): 174.
76. Yousefian, P., B. Akkopru-Akgun, C.A. Randall, et al., Electrical degradation in dielectric and piezoelectric oxides: Review of defect chemistry and characterization methods. *Prog. Mater Sci*, 2025. **153**: 101473.
77. Lin Wang, J.Z., Xingfeng Xu, Yongli Zhang, Influence of Nb_2O_5 crystal form on the structure and properties of potassium sodium niobate-based piezoelectric ceramics. *Adv Mater*, 2025. **04-0310-07**: 1007-4252.
78. Roy, K., J.E. Lee, and C. Lee, Thin-film PMUTs: a review of over 40 years of research. *Microsyst. Nanoeng*, 2023. **9**: 95.
79. Mo, Y., J. Wu, W. Liu, et al., Ultrafast piezocatalytic organic pollutant degradation enabled by dynamic spin state regulation of cobalt in nano-ferroelectrics. *Adv.Pow.Mater.*, 2025. **4**(4): 100307.
80. Liu, S., M. Wu, Y. Xu, et al., Piezo-enhanced Fenton catalysis via Fe-N active sites in graphitic carbon nitride: Toward efficient and stable tetracycline elimination. *J. Environ. Chem. Eng.*, 2026. **14**(5): 124026.
81. Lagunas-Chavarría, A., M.G. Navarro-Rojero, M.D. Salvador, et al., Effect of Microwave-Assisted Synthesis and Sintering of Lead-Free KNL-NTS Ceramics. *Materials*, 2022. **15**(11).
82. Le, O.K., V. Chihaia, V. Van On, et al., N-type and p-type molecular doping on monolayer MoS_2. *RSC Adv*, 2021. **11**(14): 8033-8041.
83. Mohammadpourfazeli, S., S. Arash, A. Ansari, et al., Future prospects and recent developments of polyvinylidene fluoride (PVDF) piezoelectric polymer; fabrication methods, structure, and electro-mechanical properties. *RSC Adv*, 2022. **13**(1): 370-387.
84. Li, M., D. Yu, S. Shen, et al., Review of n-type doping diamond: methods, elements, and properties. *Carbon Lett*, 2025. **35**(5): 1981-2009.
85. Zhang, L., S. Li, Z. Zhu, et al., Recent progress on structure manipulation of poly(vinylidene fluoride)-based ferroelectric polymers for enhanced piezoelectricity and applications. *Adv. Funct. Mater*, 2023. **33**(38): 2301302.
86. Ouyang, Z., J. Lin, R. Rao, et al., Enhancement of Piezoelectric Properties in Electrospun PVDF Nanofiber Membranes via In Situ Doping with ZnO or $BaTiO_3$. *Micromachines*, 2025. **17**(1): 12.
87. Quan, Y., L. Wang, W. Ren, et al., Enhanced electrical properties of lead-free piezoelectric KNLN-BZ-BNT ceramics with the modification of Sm^{3+} ions. *Front. Mater*, 2021. **8**: 695330.
88. Zeng, X., C. Xu, R. Rakhimov, et al., Enhanced piezoelectric response in V-doped $LiNbO_3$ films. *Ceram. Int.*, 2025. **51**(21): 33441-33450.

Just Accepted

89. Manisha Kumari, Rakesh K. Prasad, Manish K. Singh, et al., Piezoresistive_piezoelectric pressure sensor based on CVD-grown ZnO nanowires on polyethylene terephthalate substrate. *ACS Appl. Electron. Mater*, 2024. **6**: 6165−6173.
90. Fiedler, H., J. Leveneur, D.R.G. Mitchell, et al., Enhancing the piezoelectric modulus of wurtzite AlN by ion beam strain engineering. *Appl. Phys. Lett*, 2021. **118**(1): 012108.
91. Liu, R., K.H. Shin, Y. Zhu, et al., Modulating D_{33} coefficients through In situ AgF and Ag_2O growth in PVDF composites for high-performance piezoelectric nanogenerators. *Adv. Mater. Technol*, 2025. **10**(12): 2500012.
92. Damm, H., A. Kelchtermans, A. Bertha, et al., Thermal decomposition synthesis of Al-doped ZnO nanoparticles: an in-depth study. *RSC Advances*, 2013. **3**(45): 23745.
93. Xue, F., L. Chen, J. Chen, et al., p-Type MoS_2 and n-Type ZnO Diode and Its Performance Enhancement by the Piezophototronic Effect. *Adv Mater*, 2016. **28**(17): 3391-3398.
94. Muhammad, P., A. Zada, J. Rashid, et al., Defect engineering in nanocatalysts: from design and synthesis to applications. *Adv. Funct. Mater*, 2024. **34**(29): 2314686.
95. Das, D., J. Prakash, A. Bandyopadhyay, et al., Modulating the effective ionic radii of trivalent dopants in ceria using a combination of dopants to improve catalytic efficiency for the oxygen evolution reaction. *RSC Adv*, 2024. **14**(25): 17801-17813.
96. Futazuka, T., R. Ishikawa, N. Shibata, et al., Grain boundary structural transformation induced by co-segregation of aliovalent dopants. *Nat. Commun*, 2022. **13**(1): 5299.
97. Huizhan He, Y.L., Saiwei luan, Lei Zhang, Xiuhua Cao. Zhenxiao Fu ,Rong Sun, Enhancing the Reliability of Dy-doped $BaTiO_3$ Ceramics via Grain Boundary Defect Engineering. *Adv. Ceram*, 2026. **02-0150-14**: 1005-1198.
98. Cui, Y., W. Zhou, H. Yang, et al., Lattice distortion and morphology modulation enhanced piezocatalytic activity of Ca-doped $Sr_2Nb_2O_7$ towards H_2O_2 production and piezo-self-Fenton degradation. *Nano Energ*, 2025. **146**: 111540.
99. Gao, X., Z. Cheng, Z. Chen, et al., The mechanism for the enhanced piezoelectricity in multi-elements doped (K,Na)NbO_3 ceramics. *Nat. Commun*, 2021. **12**(1): 881.
100. Zhao, D., L. Yang, T. Du, et al., Boosting the piezocatalytic performance of $BaTiO_3$-based materials via phase boundary and defect co-engineering. *J. Alloy. Compd.*, 2024. **1005**: 176074.
101. Wei, J., J. Xia, X. Liu, et al., Hollow-structured $BaTiO_3$ nanoparticles with cerium-regulated defect engineering to promote piezocatalytic antibacterial treatment. *Appl. Catal. B-Environ*, 2023. **328**: 122520.
102. Zhou, F., Z. Dong, Y. Dong, et al., Regulation of piezoelectric polarization for

Just Accepted

uranium extraction dynamics by spatially gradient manipulation of oxygen vacancies. *Appl. Catal. B Environ*, 2026. **390**: 126603.
103. Xia, T., L. Lu, H. Zhang, et al., Inducing piezoelectricity in distorted rutile TiO_2 for enhanced tetracycline hydrochloride degradation through photopiezocatalysis. *J. Adv. Ceram*, 2024. **13**(3): 323-331.
104. Laurenti, M., G. Canavese, A. Sacco, et al., Nanobranched ZnO structure: p-type doping induces piezoelectric voltage generation and ferroelectric–photovoltaic effect. *Adv. Mater*, 2015. **27**(28): 4218-4223.
105. Jiang, R., G. Lu, M. Wang, et al., Lattice distortion SnS_2 piezoelectric self-Fenton system for efficient degradation and detoxification of pollutants. *NPJ Clean Water*, 2023. **6**(1): 79.
106. O'Malley, C.J., X. Tang, V. Koval, et al., Unveiling the mechanism of substitution-induced high piezoelectric performance in PLZT ceramics. *J. Adv. Ceram*, 2025. **14**(7): 9221097.
107. Zhang, Z., X. Zhang, R. Li, et al., Superior piezocatalytic activity of the $(Ba_{0.85}Ca_{0.15})(Zr_{0.1}Ti_{0.9})O_3$ crystal catalyst induced by Sm_2O_3 doping: morphotropic phase transition and defect engineering. *ACS Appl. Mater. Interfaces*, 2026. **18**(10): 14988-15002.
108. Peng, C., W. Wu, H. Huo, et al., Defect-boosted piezoelectric and nanozymatic synergetic catalysis for deep bacterial abscess therapy. *ACS Nano*, 2025. **19**(23): 21830-21843.
109. Liu, D.-M., J.-T. Zhang, C.-C. Jin, et al., Insight into oxygen-vacancy regulation on piezocatalytic activity of $(Bi_{1/2}Na_{1/2})TiO_3$ crystallites: Experiments and first-principles calculations. *Nano Energy*, 2022. **95**: 106975.
110. Huang, F., Y. Chao, M. Li, et al., Piezotronic effect driven by symmetry breaking in centrosymmetric semiconductors. *Nano Energy*, 2025. **144**: 111403.
111. Yang, M., L. Yang, S. Gai, et al., Polarization engineering and chemical bond reconstruction in rare-earth hexagonal manganite via Fe^{3+}-occupied B-site doping for piezocatalytic therapy and ferroptosis. *J. Am. Chem. Soc*, 2025. **147**(46): 42724–42742.
112. Shen, X., X. Zhang, W. Hu, et al., Symmetry-breaking modulation of platinum sites in multicomponent alloy for efficient oxygen reduction reaction. *Angew. Chem. Int. Ed*, 2026. **0**: e5938299.
113. Hou, X., K. Wang, J. Wang, et al., Doping-induced piezoelectricity in $Ba_2Nb_{2-x}Fe_xO_{6-delta}$ double perovskite oxides for efficient hydrogen peroxide production via piezocatalysis in pure water. *J. Colloid Interface Sci*, 2024. **674**: 256-265.
114. Meng, D., Y. Xiang, Z. Yang, et al., The Piezocatalytic Degradation of Sulfadiazine by Lanthanum-Doped Barium Titanate. *Molecules*, 2024. **29**(8): 1719.
115. Li, G., Q. Zhong, W. Wu, et al., Effect of rare earth cerium doping on the activity of ZnO nanomaterials for producing H_2O_2 by piezoelectric catalysis. *J Colloid Interf. Sci*, 2025. **700**: 138431.

Just Accepted

116. Kalhori, H., I.C. Amaechi, A.H. Youssef, et al., Catalytic Activity of $BaTiO_3$ Nanoparticles for Wastewater Treatment: Piezo- or Sono-Driven? *ACS Appl. Nano Mater.*, 2023. **6**(3): 1686-1695.
117. Ran, F.-Y., Z. Xiao, Y. Toda, et al., n-type conversion of SnS by isovalent ion substitution: Geometrical doping as a new doping route. *Sci. Rep*, 2015. **5**(1): 10428.
118. Zhang, D., X. Ruan, L. Wang, et al., Enhanced Lattice Polarization and Directed Charge Transport Toward Pt Surface Sites Accelerate the Volmer Step in Piezocatalytic H_2 Evolution on Co-Doped $BiFeO_3$. *Adv. Energy Mater*, 2026. **16**(23): e70895.
119. Yu, C., J. He, M. Tan, et al., Selective enhancement of photo-piezocatalytic performance in $BaTiO_3$ via heterovalent ion doping. *Adv. Funct. Mater*, 2022. **32**(52): 2209365.
120. Yang, M., B. Ding, X. Ma, et al., Multipath ROS Storm and Immune Activation via Sulfur Vacancy-Optimized $ZnIn_2S_4$ Nanosheets for Piezocatalytic Tumor Therapy. *Angew. Chem. Int. Ed.*, 2025. **64**(33): e202507502.
121. Hu, H., X. Gao, Y. Wei, et al., Engineering Compressive Strain via Oxygen Doping to Modulate the p-Band Center for Enhanced Photocatalysis and Piezocatalysis. *Inorg. Chem*, 2025. **64**(46): 23088-23096.
122. Shen, X., C. Pan, X. Wei, et al., Single-Atom Engineering and Phase-Transition Optimization in MoS_2 for Enhanced Schottky Junction Piezocatalysis. *ACS Nano*, 2025. **19**(31): 28257-28267.
123. Cai, Y.X., K.Q. Shi, C.C. Jin, et al., Defect Engineering in Two-Dimensional Piezocatalysts: A Trifunctional Perspective on Mechanisms and Design. *ChemSusChem*, 2025. **18**(23): e202501794.
124. Xiao, M., D. Han, and X. Yang, Ni-doping-induced oxygen vacancy in Pt-CeO_2 catalyst for toluene oxidation: Enhanced catalytic activity, water-resistance, and SO_2-tolerance. *Appl. Catal. B: Environ.*, 2023. **323**: 122173.
125. Wang, S., C. Meng, and Y. Bai, Synergy promotion of elemental doping and oxygen vacancies in Fe_2O_3 nanorods for photoelectrochemical water splitting. *ACS Appl. Nano Mater.*, 2022. **5(5)**: 6781-6791.
126. Kröger, F.A. and H.J. Vink, *Relations between the Concentrations of Imperfections in Crystalline Solids*, in *Solid State Physics*, F. Seitz and D. Turnbull, Editors. 1956, Academic Press: 307-435.
127. Ning, X., A. Hao, Y. Cao, et al., Boosting piezocatalytic performance of Ag decorated ZnO by piezo-electrochemical synergistic coupling strategy. *Appl. Surf. Sci*, 2021. **566**: 150730.
128. Li, S., T. Jiao, Z. Yu, et al., Boosting piezocatalytic performance in high-entropy perovskite oxides by amphoteric substitution induced oxygen vacancies. *J. Alloy. Compd*, 2025. **1045**: 184752.
129. Wang, P., S. Zhong, Y. Wang, et al., Oxygen vacancy engineering and rare earth ion modification in Er-doped $Bi_{0.5}Na_{0.5}TiO_3$–$BaTiO_3$ for piezo-photocatalysis.

Just Accepted

Ceram. Int, 2024. **50**(17): 30887-30893.
130. Tang, Q., Y. Meng, Y. Xu, et al., Tribocatalytic activity on $Ba(Ti_{0.95}Zr_{0.05})O_3$ surfaces: The role of oxygen vacancies and the aging effect. *Mat Sci Eng B-Adv*, 2023. **297**: 116814.
131. Du, T., L. Yang, Q. Zheng, et al., Achieving excellent piezo-catalytic performance of $(Bi_{0.5}Na_{0.5})TiO_3$-based piezoelectric ceramics through high-entropy induced energy band reconfiguration and oxygen vacancies engineering. *J. Alloys Compd*, 2025. **1039**: 183133.
132. Gurylev, V. and T.P. Perng, Defect engineering of ZnO: Review on oxygen and zinc vacancies. *J. Eur. Ceram. Soc*, 2021. **41**(10): 4977-4996.
133. Freeman, C.L., J.A. Dawson, H.-R. Chen, et al., Energetics of donor-doping, metal vacancies, and oxygen-loss in A-site rare-earth-doped $BaTiO_3$. *Adv. Funct. Mater*, 2013. **23**(31): 3925-3928.
134. Euvrard, J., Y. Yan, and D.B. Mitzi, Electrical doping in halide perovskites. *Nat. Rev. Mater*, 2021. **6**(6): 531-549.
135. Wang, J., D.N. Mueller, and E.J. Crumlin, Recommended strategies for quantifying oxygen vacancies with X-ray photoelectron spectroscopy. *J. Eur. Ceram. Soc.*, 2024. **44**(15): 116709.
136. Liu, C., J. Li, C. Guo, et al., Regulating interlayer charge transfer in MoS_2 via in-situ loading of Pd-metallene to enhance piezo-catalytic degradation efficiency: Contributions of low free energy. *Chem. Eng. J*, 2024. **502**: 157909.
137. Chen, Y., Y. Zhu, A. Nasir, et al., Trace $BaTiO_3$:Er^{3+} with ultrasensitive piezocatalysis. *Ceram. Int*, 2025. **51**(22): 36819-36827.
138. Lin, K., Z. Zhu, W. Ge, et al., Atomic-level unveiling secondary recrystallization enabled micro- and macroscopic polarization enhancement for piezo-photocatalytic oxygen activation. *Nano Res*, 2024. **17**(6): 5040-5049.
139. Guo, Z., X. Liu, J. Zhang, et al., Ultrasound-activated perovskite piezocatalyst for efficient inactivation of antibiotic-resistant bacteria in complex wastewater system. *Nano Res*, 2026. **19**(5): 94908301.
140. Ning, X.-E., D.-Z. Jia, S.-H. Li, et al., Oxygen-incorporated MoS_2 catalyst for remarkable enhancing piezocatalytic H_2 evolution and degradation of organic pollutant. *Rare Met*, 2023. **42**(9): 3034-3045.
141. Peng, W.-B., B.-D. Jiang, S.-H. Guan, et al., Wind-driven piezocatalytic HCHO degradation by N-doped ZnO: A combined experimental and theoretical study. *Nano Energy*, 2025. **145**: 111453.
142. Iglesias-Juez, A., G.L. Chiarello, G.S. Patience, et al., Experimental methods in chemical engineering:X-ray absorption spectroscopy—XAS,XANES,EXAFS. *Can. J. Chem. Eng.*, 2021. **100**(1): 3-22.
143. Gázquez, J., G. Sánchez-Santolino, N. Biškup, et al., Applications of STEM-EELS to complex oxides. *Mater. Sci. Semicond. Process*, 2017. **65**: 49-63.
144. Uedono, A., Material characterization using positron annihilation spectroscopy. *JSAP Review*, 2025. **94**(478): 250210.

Just Accepted

145. Xie, C., B. Niu, H. Guo, et al., Piezoelectric-catalytic degradation of organic dyes and catalytic reduction of Cr(VI) with $BaCO_3$@$BaTiO_3$ microspheres. *Appl. Catal. B Environ*, 2023. **154**: 110922.
146. Jia, P., J. Li, and H. Huang, Piezocatalysts and piezo-photocatalysts: from material design to diverse applications. *Adv. Funct. Mater.*, 2024. **34(44)**: 2407309.
147. Zheng, H., Y. Wang, and J. Liu, Recent advancements in the use of novel piezoelectric materials for piezocatalytic and piezo-photocatalytic applications. *Appl. Catal. B-Environ.*, 2024. **341**: 123335.
148. Qi, W., Y. Fu, and E. Liu, Advancements and opportunities in piezo-(photo)catalytic synthesis of value-added chemicals. *EES Catal.*, 2024. **2(4)**: 884-910.
149. Ruan, X., C. Ding, H. Cai, et al., Bulk polarization fields and interfacial electron sink in MXene-modified iodine-doped $Bi_4Ti_3O_{12}$ enhance piezocatalytic H_2O_2 generation. *Nat. Commun*, 2026.
150. Hu, C., J. Hu, Z. Zhu, et al., Orthogonal Charge Transfer by Precise Positioning of Silver Single Atoms and Clusters on Carbon Nitride for Efficient Piezocatalytic Pure Water Splitting. *Angew. Chem. Int. Ed.*, 2022. **61**(43): e202212397.
151. Liang Shu, G.P., Xiaoming Shi, Yang Zhang, Sixu Wang, Haijun Wu, Qian Li, Hangren Li, Xin Zhang, Zhen Wang, Huanhua Wang, Yongbo Fan, Chenguang Deng, Yunpeng Ma, Jiazhang Li, Limin Guo, Ke Bi, Yue- Yu- Shan Cheng, Ziqi Yang, Yue- Yao Dai, Liyu Wei, Lei Zhao, Lisha Liu, Yi- Xuan Liu, Kun Xu, Xiangdong Ding, Jun Sun, Shujun Zhang, Houbing Huang1, Jing- Feng Li,, Ultrahigh piezoelectricity by polaron- defect complexes. *Science* 2026. **394**(689): 118-125.
152. Xiong, R., F. Liu, J. Huang, et al., Spin polarization-coupled piezocatalysis in Fe-doped Bi_3TiNbO_9: Synchronous kinetic and thermodynamic optimization for superior H_2O_2 production. *Chem. Eng. J*, 2025. **525**: 170344.
153. Wu, Y., B. Chen, X. Chen, et al., Enhanced piezocatalytic therapy of MRSA-infected osteomyelitis using ultrasound-triggered copper nanocrystals-doped barium titanate. *Bioact. Mater*, 2025. **51**: 450-468.
154. Ma, X., B. Ding, Z. Yang, et al., Sulfur-Vacancy-Engineered two-dimensional Cu@SnS_{2-x} nanosheets constructed via heterovalent substitution for high-efficiency piezocatalytic tumor therapy. *J. Am. Chem. Soc*, 2024. **146**(31): 21496-21508.
155. Yang, L., S. Liu, M. Yang, et al., Manganese-Doped Piezoelectric Layered Double Hydroxides Induce Catalytic Therapy and Ferroptosis. *Adv. Funct. Mater*, 2026. **36**(45): e31699.
156. Yuan, B., J. Wu, N. Qin, et al., Sm-doped $Pb(Mg_{1/3}Nb_{2/3})O_{3-x}PbTiO_3$ piezocatalyst: Exploring the relationship between piezoelectric property and piezocatalytic activity. *Appl. Mater. Today*, 2019. **17**: 183-192.

Just Accepted

157. Cheng, W., X. Xu, H. Zhai, et al., Composition-Tuned piezoelectricity governs hydrogen evolution in $Ba_{1-x}Sr_xTiO_3$ ($0 \leq x \leq 0.3$). *Adv. Funct. Mater*, 2025. **36**(10): e16480.
158. Xu, X., Y. Wang, W. Cheng, et al., Defect dipole alignment mediated by poling for simultaneous optimization of piezoelectricity and carrier concentration in piezocatalysts. *Commun. Chem.*, 2025. **9**(1): 22.
159. Wan, L., W. Tian, and N. Li, Hydrophilic porous PVDF membrane embedded with $BaTiO_3$ featuring controlled oxygen vacancies for piezocatalytic water cleaning. *Nano Energy*, 2022. **94**: 106930.
160. Dai, J., N. Shao, and S. Zhang, Enhanced piezocatalytic activity of Sr_(0.5)Ba_(0.5)Nb_2O_6 nanostructures by engineering surface oxygen vacancies and self-generated heterojunctions. *ACS Appl. Mater. Interfaces*, 2021. **13(6)**: 7259-7267.
161. Cortés-Vega, F.D., C. Montero-Tavera, and J.M. Yañez-Limón, Influence of diluted Fe^{3+} doping on the physical properties of $BaTiO_3$. *J. Alloys Compd.*, 2020. **847**: 156513.
162. Petralanda, U., M. Kruse, H. Simons, et al., Oxygen vacancies nucleate charged domain walls in ferroelectrics. *Phys. Rev. Lett*, 2021. **127**(11): 117601.
163. Dong, Z., P. Guan, L. Zhou, et al., Enhanced piezocatalytic performance of Li-doped $BaTiO_3$ through a facile sonication-assisted precipitation approach. *ChemSusChem*, 2024. **17**(19): e202400796.
164. Zhu, J., S. Chen, S. Ding, et al., Efficient piezocatalysis of $BiFeO_3$ achieved via defect introduction through doping. *J. Alloy. Compd.*, 2026. **1058**: 187044.
165. Laurenti, M., N. Garino, G. Canavese, et al., Piezo- and photocatalytic activity of ferroelectric ZnO:Sb thin films for the efficient degradation of rhodamine-β dye pollutant. *ACS Appl. Mater. Interfaces*, 2020. **12**(23): 25798-25808.
166. Kang, Z., E. Lin, and N. Qin, Effect of oxygen vacancies and crystal symmetry on piezocatalytic properties of Bi_2WO_6 ferroelectric nanosheets for wastewater decontamination. *Environ. Sci. Nano*, 2021. **8(5)**: 1376-1388.
167. Lu, Y., C. Ding, J. Guo, et al., Cobalt-doped ZnAl-LDH nanosheet arrays as recyclable piezo-catalysts for effective activation of peroxymonosulfate to degrade norfloxacin: non-radical pathways and theoretical calculation studies. *Nano Energ*, 2023. **112**: 108515.
168. Zhao, W., G. Wang, S. Song, et al., Enhanced pizeopotential-mediated catalytic oxidation mechanism of formaldehyde and anti-deactivation performance onto ZnO surface. *Appl. Catal. B-Environ*, 2024. **353**: 124057.
169. Ning, X.-E., D.-Z. Jia, S.-H. Li, et al., Oxygen-incorporated MoS_2 catalyst for remarkable enhancing piezocatalytic H_2 evolution and degradation of organic pollutant. *Rare Met.*, 2023. **42**(9): 3034-3045.
170. Li, Y., L. Li, F. Liu, et al., Robust route to H_2O_2 and H_2 via intermediate water splitting enabled by capitalizing on minimum vanadium-doped piezocatalysts. *Nano Res*, 2022. **15**(9): 7986-7993.

Just Accepted

171. Zhao, S., M. Liu, Y. Zhang, et al., Harvesting mechanical energy for hydrogen generation by piezoelectric metal-organic frameworks. *Mater Horiz*, 2022. **9**(7): 1978-1983.
172. Liu, J., W. Qi, M. Xu, et al., Piezocatalytic techniques in environmental remediation. *Angew. Chem. Int. Ed.*, 2023. **62**(5): e202213927.
173. He, J., C. Dong, X. Chen, et al., Review of piezocatalysis and piezo-assisted photocatalysis in environmental engineering. *Crystals*, 2023. **13**(9): 1382.
174. Zhang, J., X. Luan, Z. Lv, et al., Electron transfer driven piezocatalytic degradation of emerging contaminants: Recent advances, modification strategies, and prospects. *J. Water Process Eng*, 2025. **75**: 108012.
175. Mahmood, P.H., O. Amiri, and S.M. Sajadi, $BaTiO_3$ nanoparticles for highly efficient piezocatalytic reduction of toxic hexavalent chromium: Synthesis, optimization, and kinetic study. *J. Hazard. Mater*, 2024. **16**: 100468.
176. Cai, Y., Y. Zhang, Z. Lv, et al., Highly efficient uranium extraction by a piezo catalytic reduction-oxidation process. *Appl. Catal. B Environ*, 2022. **310**: 121343.
177. Zhu, W., C. Wang, W. Hui, et al., Intrinsically morphological effect of perovskite $BaTiO_3$ boosting piezocatalytic uranium extraction efficiency and mechanism investigation. *J. Hazard. Mater*, 2023. **455**: 131578.
178. Yang, Y., S. Li, B. Wu, et al., Oxygen vacancy-mediated piezocatalytic-driven H_2O_2 pathways for efficient uranium extraction. *Appl. Surf. Sci*, 2026. **732**: 166539.
179. Feng, J., Y. Fu, X. Liu, et al., Significant improvement and mechanism of ultrasonic inactivation to escherichia coli with piezoelectric effect of hydrothermally synthesized t-$BaTiO_3$. *ACS Sustainable Chem.Eng*, 2018. **6**(5): 6032-6041.
180. Ghosh, S., A. Maity, and N.R. Jana, $BaTiO_3$ nanorod-conjugated silica gel for ultrasonic water purification via piezocatalytic generation of reactive oxygen species. *ACS Appl. Nano. Mater*, 2023. **6**(13): 11622-11629.
181. Singh, R., M. Ali, K. Sharma, et al., Ultrasound-activated piezocatalytic degradation of Rhodamine B, Ofloxacin, and inactivation of E. coli by $BaTiO_3$/CuO nanocomposites. *J. Envoron. Chem. Eng*, 2024. **12**(6): 114741.
182. He, D., W. Wang, N. Feng, et al., Defect-modified nano-$BaTiO_3$ as a sonosensitizer for rapid and high-efficiency sonodynamic sterilization. *ACS Appl. Mater. Int*, 2023. **15**(12): 15140-15151.
183. Liu, J., W. Qi, M. Xu, et al., Piezocatalytic techniques in environmental remediation. *Angew. Chem. Int. Ed*, 2023. **62**(5): e202213927.
184. He, T., Y. Jiang, W. Wang, et al., Piezo-photocatalytic synergistic reduction of U(VI) over CdS@$BaTiO_3$ heterostructure composites. *Nano Res*, 2026. **19**(19): 94908657.
185. Liang, Z., C.-F. Yan, S. Rtimi, et al., Piezoelectric materials for catalytic/photocatalytic removal of pollutants: Recent advances and outlook.

Just Accepted

Appl. Catal. B Environ, 2019. **241**: 256-269.
186. Yu, G., X. Xie, L. Pan, et al., Hybrid nanostructured materials for high-performance electrochemical capacitors. *Nano Energy*, 2013. **2**(2): 213-234.
187. Wang, Z., E. Tiukalova, Y. Tai, et al., Piezocatalytic ZnS:Mn^{2+} nanocrystals for enhanced organic dye degradation. *Mater. Int*, 2024. **100005**: 68.
188. Zhu, W., Y. Cao, S. Li, et al., Degradation of iohexol by Cu ion-doped Bi_2WO_6 activated peroxydisulfate under synergistic visible-light photocatalysis/piezoelectric catalysis. *Chem. Eng. J*, 2026. **528**: 172007.
189. Wang, S., Y. Li, K. Lin, et al., Enhancing the piezoelectric properties and carrier separation efficiency to improves Bi_2NdO_4Cl piezo-photocatalytic performance by Ce ion doping. *Appl. Surf. Sci*, 2025. **694**: 162841.
190. Cao, J., H. Zhou, C. Huang, et al., ZIF-8-derived Zn, N-codoped porous carbon as a high-performance piezocatalyst for organic pollutant degradation and hydrogen production. *J. Alloy. Compd*, 2023. **645**: 794-805.
191. Han, J., W. Tian, Y. Miao, et al., Flexoelectricity in hydroxyapatite for the enhanced piezocatalytic degradation of phenanthrene in soil. *Ind. Chem. Mater*, 2024. **2**(2): 300-308.
192. Wang, C., F. Chen, C. Hu, et al., Efficient piezocatalytic H_2O_2 production of atomic-level thickness $Bi_4Ti_3O_{12}$ nanosheets with surface oxygen vacancy. *Chem. Eng. J*, 2021. **431**: 133930.
193. Qiu, X., A. Hao, S. Hu, et al., Oxygen vacancy engineering of $Bi_4Ti_3O_{12}$ piezocatalyst driving in situ H_2O_2 evolution for self-cycled fenton-like degradation of pollutants. *Inorg. Chem*, 2025. **64**(12): 6172-6182.
194. Lei, R., F. Gao, J. Yuan, et al., Free layer-dependent piezoelectricity of oxygen-doped MoS_2 for the enhanced piezocatalytic hydrogen evolution from pure water. *Appl. Surf. Sci*, 2022. **576**: 151851.
195. Zhao, X., X. Lu, W.J. Chen, et al., Exceptional piezocatalytic H_2 production of nitrogen-doped TiO_2@carbon nanosheets induced by engineered piezoelectricity. *J Colloid Interf. Sci*, 2024. **659**: 11-20.
196. Guo, M., Y. Li, and S. Qiao, Bacteria-piezocatalyst for NO^{3-} reduction to NH^{4+} driven by hydraulic kinetic energy. *Water Res*, 2025. **286**: 124292.
197. Zhai, Y., J. Ye, Y. Zhang, et al., Excellent sensing platforms for identification of gaseous pollutants based on metal–organic frameworks: A review. *Chem. Eng. J*, 2024. **484**: 149286.
198. Rehman, S.U., M.H. Hassan, H.-S. Kim, et al., Designing the nano-scale architecture of the air electrode for high-performance and robust reversible solid oxide cells. *Appl. Catal. B Environ*, 2023. **333**: 122784.
199. Gao, F., Z. Wang, M. Fang, et al., Biological calcium phosphate nanorods for piezocatalytical extraction of U(VI) from water. *Nano Res*, 2023. **16**(11): 12772-12780.
200. Zhong, L., X. Guo, L. Deng, et al., Dopant-regulated piezocatalysts evoke sonopiezoelectric and enzymatic PANoptosis for synergistic cancer therapy.

Just Accepted

Adv. Sci, 2025. **12**(17): 2500406.
201. Guo, R., L. Jin, X. Zhang, et al., Bimetal doping enhanced polarization electric field in $BiFeO_3$ for piezocatalytic U(VI) reduction and hydrogen production. *Appl. Catal. B Environ*, 2025. **367**: 125113.
202. Chen, J., Y. Liu, Q. Guo, et al., Synergistic enhanced piezocatalytic properties of Nd-doped $BaTiO_3$-based nanosheets with NaCl assistance. *J. Phys. Chem. C*, 2025. **129**(129): 11655−11665.
203. Guo, R., L. Jin, X. Zhang, et al., Bimetal doping enhanced polarization electric field in $BiFeO_3$ for piezocatalytic U(VI) reduction and hydrogen production. *Appl. Catal. B Environ.*, 2025. **367**: 125113.
204. Singhal, M., A. Gaur, and S. Patel, Piezocatalytic investigation on $0.97(Na_{0.5}Bi_{0.5})TiO_3$-$0.03Ba(Ni_{0.5}Nb_{0.5})O_3$-$x$La for dye degradation from water. *Appl. Surf. Sci.*, 2025. **714**: 164498.
205. Wang, L., K. Cui, Y. Liu, et al., Dual optimization of Ca-doped $BaTiO_3$ by combined doping and annealing: mechanistic understanding and hydro-activated piezocatalytic degradation of organic pollutants. *Chem. Eng. J*, 2026. **527**: 172000.
206. Jiang, L., N. Xie, Y. Hou, et al., Enhanced piezocatalytic performance of $(Bi_{1/2}Na_{1/2})(1\text{-}x)_3$ piezoelectric material with morphotropic phase boundary for degradation of RhB. *Catal. Commun*, 2023. **181**: 106735.
207. Cheng, S., Y. Luo, J. Zhang, et al., The highly effective therapy of ovarian cancer by Bismuth-doped oxygen-deficient $BaTiO_3$ with enhanced sono-piezocatalytic effects. *Chem. Eng. J*, 2022. **442**: 136380.
208. Yu, C., Y. Dong, X. Zhu, et al., Oxygen vacancy piezoelectric nanosheets constructed by a photoetching strategy for ultrasound “unlocked” tumor synergistic therapy. *Nano Lett*, 2024. **24**(26): 8008-8016.
209. Liu, H., R. Li, B. Zhang, et al., Leveraging Mn-doping to modulate band structure and carrier dynamics in $BaTiO_3$ for efficient piezoelectric-chemodynamic cancer therapy. *Mater. Des*, 2026. **266**: 116189.
210. Zhang, P., H. Sun, W. Zhang, et al., Ultrasound-triggered Mn-$BaTiO_3$ nanoplatform for MRI-guided piezocatalytic therapy. *Adv. Mater. Technol*, 2026. **11**(8): e01331.
211. Meher, N., K. Seo, S. Wang, et al., Synthesis and preliminary biological assessment of carborane-loaded theranostic nanoparticles to target prostate-specific membrane antigen. *ACS Appl. Mater. Int*, 2021. **13**(46): 54739-54752.
212. Pang, Z., B. Ding, J. Wang, et al., Metal-ion inserted vanadium oxide nanoribbons as high-performance cathodes for aqueous zinc-ion batteries. *Chem. Eng. J*, 2022. **446**: 136861.
213. Jiang, P., C. Wang, S. Wu, et al., Interstitial nitrogen doping in barium titanate amplifies ultrasound-triggered piezocatalysis for eradicating biofilms and boosting osseointegration. *Adv. Funct. Mater*, 2026. **36**(34): e29205.
214. Wei, Y., X. Hu, and J. Shao, Daily sonic toothbrush triggered biocompatible

Just Accepted

$BaTiO_3$/chitosan multiporous coating with enhanced piezocatalysis for intraoral antibacterial activity. *Mater. Today Commun.*, 2024. **38**: 107715.
215. Wu, L., Y. Lu, L. Liu, et al., $BaTiO_3$ doping enhances ultrasound-driven piezoelectric bactericidal effects of fibrous poly(L-Lactic Acid) dressings to accelerate septic wound healing. *ACS Appl. Mater. Int*, 2024. **16**(49): 67477-67490.
216. Zhu, P., Y. Chen, and J. Shi, Piezocatalytic tumor therapy by ultrasound-triggered and $BaTiO_3$-mediated piezoelectricity. *Adv. Mater.*, 2020. **32(29)**: 2001976.
217. Hoang, Q.T., V. Ravichandran, and T.G.N. Cao, Piezoelectric Au-decorated ZnO nanorods_ ultrasound-triggered generation of ROS for piezocatalytic cancer therapy. *Chem. Eng. J.*, 2022.
218. Chen, J., Q. Tang, Y. Wang, et al., Ultrasound-Induced piezocatalysis triggered NO generation for enhanced hypoxic tumor therapy. *ACS Appl. Mater. Int*, 2023. **15**(12): 15220-15234.
219. Zhang, M., X. Song, Y. Qin, et al., Single-atom-doped piezocatalyst induces copper-free cuproptosis in tumor therapy. *Sci. Adv*, 2025. **11**(11): eadt8451
220. Jing, L., F. Zhuang, W. Feng, et al., Doping-engineered piezoelectric ultrathin nanosheets for synergistically piezo-chemocatalytic antitumor and antibacterial therapies against cutaneous melanoma. *Small*, 2024: 2401171.
221. Han, Y., H. Zhang, R. Yang, et al., Ba^{2+}-doping introduced piezoelectricity and efficient Ultrasound-Triggered bactericidal activity of brookite TiO_2 nanorods. *J Colloid Interf. Sci*, 2024. **670**: 742-750.
222. Zheng, G., Z. Tang, and F. Peng, Ultrasound-activated inorganic nanomaterials to generate ROS for antibacterial applications. *Biomater Sci.*, 2025. **13(10)**: 2628-2641.
223. Park, S., H.Y. Jeong, and S. Kim, Strategic design of emerging (K,Na)NbO_3-based perovskites for high-performance piezocatalysis and photo-piezocatalysis. *Nanoscale*, 2025. **17(6)**: 2931-2960.
224. Jiang, Y., J. Liang, F. Zhuo, et al., Unveiling Mechanically Driven Catalytic Processes: Beyond Piezocatalysis to Synergetic Effects. *ACS Nano*, 2025. **19**(19): 18037-18074.
225. Zhang, S., F. Gao, X. Qiu, et al., Research progress of piezocatalysis in energy and environment fields. *Chem. Commun*, 2026. **62**(16): 4648-4669.
226. Sankari Jeyabalan, S., O. Sudhir Ekande, B. Mainali, et al., A systematic review of recent advances in piezocatalysis – Synergetic heterojunctions for organic pollutants removal, immobilization, and scope of machine learning techniques. *Chem. Eng. J*, 2024. **498**: 155086.
227. Shi, J., P.W. Kantoff, R. Wooster, et al., Cancer nanomedicine: progress, challenges and opportunities. *Nat. Rev. Cancer*, 2017. **17**(1): 20-37.

Just Accepted